Creating a two dimensional cold mixture experiment

by

Michael Holynski

A thesis submitted to
The University of Birmingham
for the degree of
DOCTOR OF PHILOSOPHY

Midlands Ultra-cold Atom Research Centre
School of Physics and Astronomy
College of Engineering and Physical Sciences
The University of Birmingham

November 2012

Abstract

A cold atom experiment can be used to simulate analogous solid-state systems. This provides the benefit of having a high degree of control over the system parameters and allowing direct detection methods. Disordered transport is one example of where such a system has much to offer. This thesis concerns the development of a Bose-Fermi mixture experiment for study of two-dimensional optical lattice systems. To achieve single site resolution of the lattice, the experiment makes use of a double microscope set-up. One microscope provides imaging and the second is used to image a spatial light modulator onto the atomic plane. This provides an extremely versatile potential landscape for a trapped cloud.

This thesis presents an overview of the set-up of the experiment including progress towards condensation. Particular focus is given to the design and characterisation of the vacuum system and the combined double microscope and spatial light modulator system. The vacuum system design requires a narrow magneto-optical trapping chamber. A novel epoxy sealing technique has been developed, allowing construction of a chamber of just 36mm thickness whilst maintaining high optical access. To provide illumination for the spatial light modulator a technique for homogenising the output of multi-mode fibre has been developed.

CONTENTS

CHAPTER 1

INTRODUCTION

Cooling or compressing an ensemble of particles such that their de Broglie wavelength becomes larger than the inter-particle spacing causes the ensemble to undergo a statistical phase transition to a new phase, the character of which is governed by the particle's spin degree of freedom. Bosonic particles with integer spin collapse into the ground state of the system forming a Bose-Einstein condensate (BEC) while fermionic particles with half integer spin are subject to the Pauli exclusion principle meaning that a spin-polarised ensemble will instead fill the energy states of the system up to the Fermi energy, forming a degenerate Fermi gas.

Since the first experimental achievement of BEC in 1995 [1,2] the use of cold atoms has become widespread, finding applications ranging from precision measurement to simulation of physical systems from different fields. By manipulating cold atoms with optical fields it is possible to create systems analogous to solid state systems. Many features familiar from lattice physics have been successfully reproduced using optical lattice cold atom experiments, such as the band structure or the Mott insulator transition [3, 4]. However, while a solid state sample always contains impurities, an optical lattice system is intrinsically regular. A cold atom system has the benefit of not only allowing the removal of key terms in the Hamiltonian, but also selective reintroduction. An optical lattice can be modified with an unprecedented degree of control, allowing large variation in the lattice depth and the addition of impurities through optical or particulate means. Inter-particle interactions are always present in the solid state experiment, while in an optical lattice these are tuneable over a wide range, allowing study of interaction induced effects. Further to this, detection techniques in solid state lattices rely on indirect methods such as measurement of transport properties while cold atom experiments can directly monitor the distribution of atoms on the lattice.

Many important open questions in solid state physics currently reside in two dimensional systems. From

a theoretical approach, both analytical and mean field theories break down, leaving a primarily numerical, and currently often incomplete, approach. One such question is that of high temperature superconductivity, the pairing mechanism for which remains unclear since the discovery in 1986. Many of the cuprate high temperature superconductors are highly anisotropic, showing a preference for motion on CuO_2 planes.

Transport phenomena in two dimensions also present a challenge for both theory and experiment. In the case of Anderson localisation [5] dimensionality plays a decisive role in determining the sensitivity of a system to a perturbing disorder. For example, it has been shown theoretically that with increasing disorder strength a three dimensional system should show a transition from an extended, or metallic, state in which the atom wave can freely expand over the whole system to an insulating state in which the wave is isolated within a distance referred to as the localisation length. In one dimension any non-zero disorder is enough to drive the infinite system to an insulator. This has also been verified experimentally, showing that localisation takes place over a length scale similar to the mean free path in the medium. The most interesting case is that of two dimensions, where the predictions of a scaling theory [6] suggest that an infinite two dimensional sample is always an insulator for any non-vanishing disorder, but that the length scale of localisation is much larger, being instead exponentially dependent on disorder strength. This is yet to be conclusively observed using a cold atom system. The problem is experimentally challenging as in order to achieve localisation over a practical distance, the mean free path must approach the same length scale as the wavelength of the sample wave. Furthermore, wave transport experiments are typically limited by absorption masking the exponential decay.

Such situations are clear examples of where the cold atom field can add to the current understanding. By simulating a complex physical system using a simpler and highly controllable model, insight can be given into the workings of the system. For example, in the case of Anderson localisation, optical fields can be used to represent disordered media in an attempt to achieve sufficient scattering to suppress transport in two dimensions. The disorder strength can be varied trivially, allowing full study of the localisation length dependence on disorder strength. Such advantages have lead to a surge in the study of disorder physics using cold atom systems, with Anderson localisation of matter waves being observed in [7–9]. Perhaps most interestingly, the influence of how inter-particle interactions affect the Anderson problem can be studied. This has been a long standing question since the theoretical demonstration of Anderson localisation, with the current prediction being the appearance of a new phase of matter, the Bose glass [10]. After the realisation of Anderson localisation of matter waves, cold atom experiments have quickly moved on to begin exploring the interaction-disorder phase diagram [11].

The subject of this thesis is the design and construction of a new Bose-Fermi mixture experiment in an empty lab. This is intended to study two dimensional physical systems, in particular those of relevance to condensed matter physics. For study of phenomena such as Anderson localisation, a disordering potential is required along with the option of an optical lattice. Additionally, a direct measurement technique is required for a clear understanding of the evolution of the atom cloud. To achieve both goals a novel approach has been developed in which the atomic sample is placed between two high resolution microscope objectives. One of these is used to image a spatial light modulator onto the atomic plane, providing a controllable light field capable of generating a wide range of optical potentials such as lattices or random media. The second objective can then be used for detection. An example of one of the many novel uses for such a system would be to produce an optical lattice using the spatial light modulator pattern. In this case, as both the potential and detection light are resolved over approximately the same length scale it will be possible to distinguish atoms occupying individual lattice sites. This would allow resolution of single sites in the lattice, a feat achieved recently in [12, 13] through use of high resolution lenses. Although a single particle effect, there are still questions regarding how having a fermionic or bosonic ensemble will alter the Anderson picture. This will of course play an additional role when attempting study of the Bose glass phase by bringing interactions back into the system. For this reason, and to permit study of various other interesting physical systems, the experiment has also been prepared as a mixture experiment, creating cold atom samples of bosonic rubidium 87 and fermionic potassium 40. This also allows the use of one species as a disordering medium for another.

The thesis will begin with Chapter 2 providing an overview of disorder induced transport, giving some background understanding and developing formulae useful in later chapters. Chapter 3 will follow with an overview of the procedure used to prepare cold atom samples in the experiment, including an overview of the techniques used and the apparatus with which they are performed. Chapter 4 will give a more detailed discussion of the design and construction of the ultra-high vacuum system used in the experiment along with development of a specialised, highly compact sealing technique for bonding windows directly onto a metal vacuum chamber. Chapter 5 covers the design and testing of the high resolution imaging system and the spatial light modulator to be used for generating potentials. To reduce fringes on the illumination beam a novel technique has been developed which relies on averaging the output of a multi-mode fibre over short timescales. The progress of the experiment as a whole is presented in Chapter 6. The main results of the thesis are summarised in Chapter 7, and an outlook for the future progression of the experiment given.

Statement of contributions

The setting up of a new experiment requires a great deal of design and putting together of various, very different systems. Fortunately, the experiment has been the work of a small group of people through the duration on which this thesis is based, ranging from undergraduate students working on summer projects up to the principal investigator. In particular, four PhD students have worked on the project, meaning a good deal of overlap. The experiment system contains many sub-systems each having a responsible student performing the bulk of design work with significant contributions from the rest of the team. As such, it would be impossible to present a complete picture of the experiment without mentioning some of the work of others. Such instances will be highlighted here. Chapter 3 gives an overview of the key components of the experiment. The high speed computer control system used to run the experiment and dipole trapping scheme were developed by M. Baumert while the rubidium and potassium laser systems were designed by N. Meyer and put together with the assistance of M. Perea-Ortiz. The magnetic coil system was developed by N. Meyer with M. Baumert building the oil cooling system and the author putting together the IGBT system used to interface between the coils and the computer control. The linear actuator was implemented by both M. Baumert and the author, with M. Baumert developing the software to run the actuator and the triggering apparatus, while the actuator and mounting equipment was chosen and developed by the author. The work of Chapter 4 is predominantly based on the work of the author, with the exception of the design of the glass cell which was undertaken by M. Baumert. The work of Chapter 5 is again the work of the author, but contains analysis based on results taken by the M. Sci. students A. Blackmore [14] and C. Willis [15] while being supervised by the author. Finally, the work of Chapter 6 contains results arising from work undertaken together by all of the PhD students of the project. The contribution of the principal investigator, Professor K. Bongs, and the experiment lead, Dr J. Kronjaeger, can be assumed throughout.

CHAPTER 2

ANDERSON LOCALISATION

2.1 Introduction

Multiple scattering is a phenomenon present in everyday life, from the grey hue of a raincloud to the change in pitch when placing a spoon into a tea cup containing cold or boiled water. In each case the input wave is absorbed as it scatters through the medium, for a raincloud light from the sun is scattered by water droplets while in the tea cup micro-bubbles scatter high frequency sound waves resulting in a lower pitched sound. Depending on the strength of the scattering, transport through a medium can occur through several regimes. A dense collection of scatterers may give rise to a diffusive process such as Brownian motion while few scatterers allow more direct crossing of the system, for example ballistic transport. Transport processes are typically defined by the rate at which an initial distribution spreads through the system. For a wave travelling through a random medium in a classical picture, transport through the system proceeds via diffusion. This is defined as having a mean squared displacement of $\sigma^2 \approx Dt^n$ at time t, where D is the diffusion coefficient, and n determines the nature of the diffusion, with values $n > 1$ resulting in super-diffusion and values $n < 1$ giving sub-diffusion. If coherence is maintained between wavelets scattered on the potential then as the wave expands through the medium coherent contributions interfere to reduce the ability of the wave to diffuse, effectively applying a spatial decay to the diffusion constant. This is a phenomenon known as weak-localisation. If the scattering is strong enough, or the sample size large enough, the diffusion constant is reduced to zero and the wave is localised within a volume determined by the scattering strength.

One of the aims of the experiment system is to be able to explore a range of transport phenomena in particular that of Anderson localisation [5]. This makes up one phase of the superfluid-insulator phase diagram of Figure 2.1. In the weak disorder and weakly interacting regime particles in a bulk lattice will

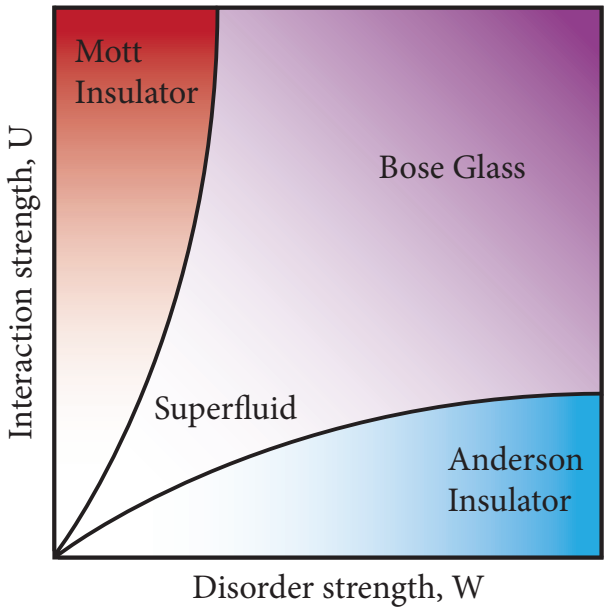

Figure 2.1: showing the speculative phase diagram of the disorder-interaction lattice system. At weak interaction energy, U, and disorder amplitude, W, the system is superfluidic and particle wave functions can extend over the whole sample. For U>>W and W≈0 the system is driven into the Mott insulator phase. For W>>U and U≈0 the system is localised by disorder and becomes an Anderson insulator. In either case particle wave functions are prevented from extending across the sample. In the intermediate case, U≈W>0, neither dominates and the system is predicted to enter the Bose glass phase.

be in the superfluid phase (or metallic in the context of solid-state physics) and a particle wave function can extend over the entire sample. Multiple wave packets across the system are then coherent. If either the disorder or interaction strength is increased sufficiently the system is driven to an insulating state and particle wave functions are localised, destroying coherence across the lattice. In the disorder case the system is Anderson localised while localisation from interactions gives rise to the Mott insulator state [16]. The least understood portion of the phase diagram is that of non-zero disorder and interaction strengths. In different regimes interaction is predicted to either suppress or aid localisation by disorder. Of particular interest is the supposed appearance of a predicted phase referred to as the Bose glass [10]. This is believed to be made up of many pockets of superfluid separated by regions in which transport is suppressed. However, the exact shape of the phase diagram is subject to considerable debate [10,17–19]. A two dimensional cold atom system would be ideal for observation of such a phase, allowing control over both interaction and disorder strength while permitting direct detection methods.

As Anderson localisation has the most stringent requirements concerning the random potential, requiring the finest modulation size or strongest effective disorder, being able to produce an Anderson localised wave packet guarantees capability of reaching other transport regimes. This chapter is therefore concerned with

providing some background understanding on the Anderson localisation problem, sufficient to calculate and interpret what parameters are required of the experiment for producing an Anderson localised sample.

2.2 Length scales and transport regimes

The localisation phenomenon is perhaps best explained as absence of wave diffusion resulting from disorder in a medium. Originally observed in a model designed to study the transport of a single spin through an array of disordered lattice sites [5], the problem has since been extended. It is now understood that localisation arises from coherent back-scattering occurring during multiple scattering of a single particle. The contribution of many back-scattering paths renormalises the diffusion constant toward zero [20]. Over long enough length scales, or for strong enough disorder, the diffusion constant is reduced to zero and no transport can occur beyond this effective boundary on the system size.

The transport of a wave through a disordered system, of length L, involves scattering of the wave with the various modulations in the potential. Two types of scattering occur during motion; first elastic scattering with the potential where the frequency of the wave is preserved but the direction of propagation is not. The characteristic length scale associated with this is the mean free path, l; the average distance between two elastic scattering events. The second is inelastic scattering where both the frequency and direction of propagation are altered. The scattering length for this, the coherence length L_ϕ, is not a property of the disorder potential but rather due to other mechanisms such as the electron-electron interaction in an electronic system or inelastic scattering of photons in an optical potential. For situations where $l \ll L_\phi$ the wave can undergo many scatterings before losing phase coherence meaning that the coherent phenomena underlying localisation can be observed.

The important length scale for interference is the wavelength, λ. A useful quantity in describing the strength of scattering in the medium for a particular wave is the number of mean free paths contained in one wavelength, i.e. the ratio $\frac{l}{\lambda}$ or rather $k \cdot l$ with $k = \frac{2\pi}{\lambda}$ the wave number [21, 22]. For large values of $k \cdot l$ the wave can travel over many wavelengths before scattering. If this is such that $l \approx L$ then the wave may scatter only a few times during crossing the system and has a negligible chance of scattering upon the same modulation twice; the wave will cross the system almost directly with a time scale linear in L. For $l \ll L$ the wave will scatter diffusively across the system and is described by the diffusion equation with diffusion constant $D = \frac{lv}{d}$ with v the average speed of the wave and d the dimensionality of the system. The wave now takes time of order $\frac{L^2}{D}$ to cross the system. For L sufficiently larger than l the probability of scattering with a single modulation twice begins to become noticeable. In either regime, $l \approx L$ or $l \ll L$, as long as $k \cdot l \gg 1$ the

wave function can be considered as propagating plane waves which are only lightly perturbed by the disorder. Naturally the next regime of interest is that where $l \ll L$ with $k \cdot l$ intermediate. Repeated scattering with a single modulation becomes important and allows the macroscopic presence of coherent phenomena which reduce the diffusion constant for the wave in the medium meaning slower transport and crossing times. For $k \cdot l \approx 1$ the wave only moves a distance of approximately the wavelength before being scattered meaning interference continues to be important during scattering, this is known as the Ioffe-Regel condition. Transport can no longer be thought of as propagation of plane waves but rather waves which are over-damped. In this situation the wave becomes strongly localised by the disorder and the diffusion constant rapidly drops to zero. The wave function develops an exponentially decaying envelope with characteristic length scale ξ, the localisation length. It should be emphasised that dimensionality plays an overwhelming role in the behaviour of localisation and as such the above description is only figurative. A discussion of the influence of dimensionality, with particular emphasis on $d = 2$, is delayed until Section 2.4. As is clear from the above discussion the mean free path is of critical importance in the study of localisation. Determination of this for useful cases is the topic of Section 2.5 with an emphasis on situations relevant to future experiment. Section 2.6 will present an overview of the experimental efforts into understanding localisation. Finally, Section 2.7 will present considerations relevant for realising two dimensional localisation in the current experiment.

2.3 Coherent back-scattering and weak localisation

Understanding the physics underlying localisation requires study of the interference between the different scattering paths available for an incident wave [20, 23]. Consider a particle travelling through a disordered medium by elastically scattering with modulations in the potential. The interference pattern for a particle incident with wave vector k scattering until being emitted with wave vector k' is given by

$$I(k,k') = \left| \sum_{r,r'} A(r,r') e^{ik\cdot\mathbf{r} - ik'\cdot\mathbf{r}'} \right|^2 = \sum_{r,r'} \sum_{b,b'} A(r,r') A^*(b,b') e^{ik\cdot\mathbf{r} - ik'\cdot\mathbf{r}'} e^{-ik\cdot\mathbf{b} + ik'\cdot\mathbf{b}'} \tag{2.1}$$

where the modulus square of the function A represents the probability of the wave scattering from point r to r'.

The useful approach is to average over the configurations of the disorder potential. During this process the length of trajectories for different paths are randomised, meaning the phase differences between pairs of paths are also randomised. This causes the majority of the interference terms to fluctuate in sign and cancel during averaging. The only terms which remain are those for pairs of paths which have trajectory lengths

that are identical to each other and thus have phase difference of zero. This can only happen when the scattering paths are identical and so for paths representing the same sequence of scatterings. Therefore the only remaining terms are complementary paths which have the same trajectories either traversed in identical sequence or in the reverse. Pairs which have identical ordering require $r = b$ and $r' = b'$ and contribute terms of the form:

$$\langle I_{incoherent} \rangle = \left\langle \sum_{r,r'} |A(r,r')|^2 \right\rangle \tag{2.2}$$

where the angled brackets represent configurationally averaging over the disorder. This is the classical component of the conductivity which one arrives at following the Drude approach which considers all paths to be phase incoherent. This is a good approximation when multiple scattering upon a given modulation is unlikely. Pairs travelling their paths in opposite direction require $r = b'$ and $r' = b$ giving contribution

$$\langle I_{coherent}(k,k') \rangle = \left\langle \sum_{r,r'} |A(r,r')|^2 \, e^{i(k+k')\cdot(r-r')} \right\rangle \tag{2.3}$$

The configurationally averaged intensity is then given by

$$\langle I_{total}(k,k') \rangle = \left\langle \sum_{r,r'} |A(r,r')|^2 \left[1 + e^{i(k+k')\cdot(r-r')} \right] \right\rangle \tag{2.4}$$

The coherent term generally averages to zero due to the fluctuating phase factor. However, for cases where the paths have opposite wave vector the wave is travelling in the opposite direction. Phase coherence then causes an extra contribution in the back-scattering direction. The phase coherence is not maintained in any other direction and so, due to constructive interference, the intensity in the backward direction is twice that of the classical value. This is the phenomenon known as coherent back-scattering. Perhaps the most direct observation of this phenomenon is that upon illuminating a disordered medium one receives a cone of increased intensity in the backward direction of the wave on top of the classical intensity. The cone originates from k values near $-k$ and has a width of order $\frac{1}{k \cdot l}$ for isotropic scattering [24]. This means that as one approaches the Ioffe-Regel criterion the cone will become broader and broader for stronger scattering.

For cases where the wave returns to its initial position, i.e. when $r = r'$, the intensity is also doubled regardless of the direction of the wave. The increased probability to remain in a closed loop reduces the probability of transmission through the disordered medium. This is the origin of weak localisation, a precursor of Anderson localisation. This and coherent back-scattering work together in reducing the diffusion constant

and therefore transport through the system.

Interestingly these coherent effects also cause the diffusion constant to no longer be an intensive quantity [25]. This is because for a larger sample size more closed loops will be present meaning a larger reduction in the diffusion constant. The consequence of this for a wave introduced to the medium is that the nature of transport will alter as it progresses through the sample. Initially it will travel as though in an unperturbed medium until it has scattered enough to enter the diffusive regime. Once diffusing, the onset of coherent effects will reduce the diffusion constant with the reduction increasing gradually as more closed loops appear. Eventually the diffusion constant will be reduced to zero and the wave is localised. It is important to note that the size of the system is determined by the presence of dephasing processes. For systems of physical size much larger than L_ϕ the effective system size reduces to L_ϕ for study of coherent effects. Therefore by altering L_ϕ one could observe the system size dependence of the back-scattering effect without the need to alter the system itself.

The assumption that the phase difference is zero for pairs of reversed paths is only correct when the system is time reversal symmetric. If this were otherwise, for example through motion of the scatterers, then the contribution in the back-scattering direction would be diminished depending on the degree to which symmetry was present. Therefore, the disordering potential is required to be static over the transport time.

2.4 The influence of dimensionality

An understanding of the behaviour of localisation in d dimensions can be obtained by following the arguments which lead to the scaling theory of localisation [26, 27]. Consider a sample, of side L, which is built up from various microscopic d dimensional cubes. In order to gain information about the wave transport properties of such a medium one could introduce an excitation within each cube and measure the response on the sample surface. If the sample size is then increased it would be expected that for an extended state the response at the surface would stay constant. For a localised state the response will decrease as the sample size increases because of the decaying envelope of the wavefunction.

This picture can be inverted so that rather than focusing on the response at the surface one instead examines the sensitivity of the interior wavefunction to changes of the boundary conditions at the surface, i.e. $\psi(\mathrm{n}+1)=\mathrm{e}^{i\chi}\psi(1)$ with a symmetric and periodic system for $\chi = 0$ to antiperiodic when $\chi = \pi$. The picture is then as follows, an extended state has a wavefunction spread across the whole sample including the boundaries meaning that it always remains sensitive to changes; for a localised state the wavefunction decays exponentially over length ξ and can only experience changes through regions of small amplitude resulting in

a drastically reduced sensitivity for samples with $L \gg \xi$.

The eigenstate of the sample is a linear combination of the eigenstates of the cubes. A single cube is perturbed by neighbouring cubes according to their overlap integral and the difference in their energy. The energy denominator is given by the average level spacing, $\delta\epsilon \approx (NL^d)^{-1}$ and the overlap can be considered as the energy change, ΔE, caused by twisting the boundary conditions through changing $\chi = 0 \to \pi$. The two quantities are the only factors contributing to the admixture, giving a ratio $\frac{\Delta E}{\delta\epsilon}$ which can be used to determine whether a state is localised. For $\frac{\Delta E}{\delta\epsilon} \gg 1$ the cube wave functions can mix and extend over the system while for $\frac{\Delta E}{\delta\epsilon} \ll 1$ each cube is isolated and wave functions are localised.

It is now useful to define the dimensionless conductance, $g = G \cdot \frac{\hbar}{e^2}$ with G the conductance and $\frac{e^2}{\hbar}$ the quantum of conductance. Thouless argued that this is directly related to the ratio $\frac{\Delta E}{\delta\epsilon}$ making it the useful parameter in deciding whether a system is localised [27, 28]. Returning to the sample of side L, if this was used to construct another cube of side $2L$ then it would be expected that $g(2L)$ should depend only upon $g(L)$, i.e.

$$g(nL) = f(g(L)) \tag{2.5}$$

or, written continuously;

$$\frac{\Delta g}{g} = \beta(g)\frac{\Delta L}{L} \tag{2.6}$$

where $\beta(g)$ is the scaling function depending only on the value of the dimensionless conductance [6, 29]. In situations where $\beta(g) < 0$ the dimensionless conductance decreases with length scale and the system is in the localised regime. The asymptotes of the scaling function can be found quite trivially. In the Ohmic regime the conductance behaves as

$$G(L) = \sigma\frac{A}{L} = \sigma L^{d-2} \tag{2.7}$$

and in this limit $\beta(g) = d - 2$. In the localised regime of small g, g must decay exponentially as the system size expands over the localisation length

$$g(L) = g_0 e^{-\frac{L}{\xi}} \to \ln g = \ln g_0 - \frac{L}{\xi} \tag{2.8}$$

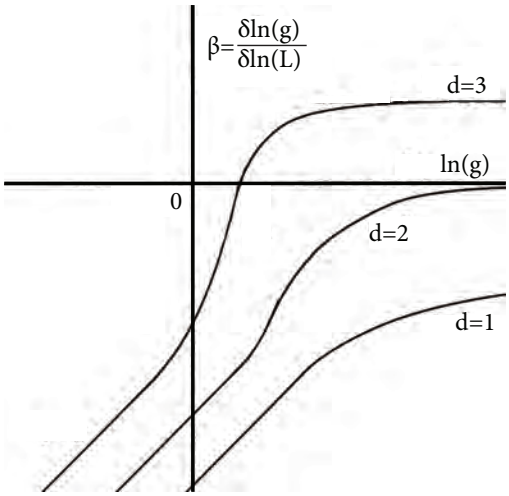

Figure 2.2: The scaling function $\beta(g)$ shows a transition from negative to positive for a critical value of g in three dimensions while in $d = 1, 2$ it is always negative and all states are localised in the infinite system [6].

giving a scaling function of the form $\beta(g) = \ln(\frac{g}{g_0})$. Figure 2.2 shows the continuous linking of these asymptotes for $d = 1, 2$ and 3. This shows a clear transition in $d = 3$ from $\beta(g) < 0 \rightarrow \beta(g) > 0$ as g is increased, and therefore the disorder strength weakened. In $d = 1$ there is clearly no transition and all states are localised. In $d = 2$ is it necessary to determine whether the scaling function is always negative. The dimensionless conductance is corrected by weak localisation even for the Ohmic regime, thus having the form $g(L) = g_0 + \delta g(L)$. Determining the sign of $\delta g(L)$ determines the sign of the scaling function at this asymptote. This can be achieved by calculating the first order correction due to weak localisation and is given in (2.11), having the form $\delta g(L) \propto -\ln(\frac{L}{l})$. The consequence is that for any non-vanishing disorder all states are predicted localised in $d \leq 2$ and in general no metal-insulator transition can occur.

2.4.1 Coherent back-scattering and dimensionality

The lack of a metal-insulator transition in one and two dimensions can be understood by considering how the probability of return behaves for a diffusive system and comparing this to the availability of closed loops for coherent back-scattering [25]. The solution to the diffusion equation for a particle diffusing away from the origin is given by

$$P(\vec{r}, t) = (4\pi Dt)^{-\frac{d}{2}} \exp\left(\frac{-r^2}{4\pi Dt}\right) \tag{2.9}$$

which describes the probability density for the particle to be at distance r at time t. Integrating (2.9) over

all times after a cut off, to allow motion away from the origin, and with $r = 0$ gives the probability to return. By allowing the upper time limit to tend to infinity the probability of the particle returning to the origin can be found:

$$\lim_{T\to\infty}\int_{t_c}^{T}\frac{dt}{(4\pi Dt)^{\frac{d}{2}}} = \begin{cases} \frac{\sqrt{T}-\sqrt{t_c}}{4\sqrt{\pi D}} & d=1 \\ \frac{1}{4\pi D}\ln\left(\frac{T}{t_c}\right) & d=2 \\ \frac{1}{16(\pi D)^{\frac{3}{2}}}\left(\frac{1}{\sqrt{t_c}}-\frac{1}{\sqrt{T}}\right) & d=3 \end{cases} \tag{2.10}$$

For one and two dimensions the integral diverges meaning the particle will return to the origin. For three dimensions the integral is dominated by the cut off time, with long cut off reducing the probability of return. Therefore after longer and longer times it becomes less likely to return to the origin. This can be understood by examination of the diffusion path for a particle in two and three dimensions, shown in Figures 2.3 and 2.4 respectively. The two dimensional random walk shows numerous returns to the vicinity of the origin while in the three dimensional case the distance increases with step number suggesting no return at infinite times. The diffusion path in two dimensions covers the majority of the area which it sits in while the extra freedom granted in three dimensions means that the same effective area swept out per unit time is spread over a much larger space, therefore giving less motion in the region of the origin on average.

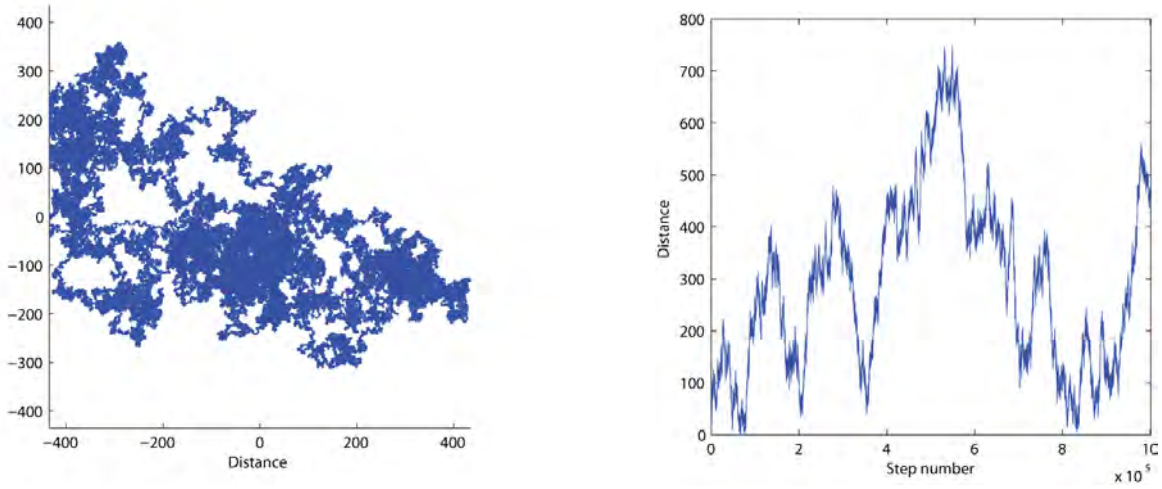

Figure 2.3: *Left:* Two dimensional random walk of one million steps. *Right:* Magnitude of distance from origin versus step number showing repeated returns to the vicinity of the origin

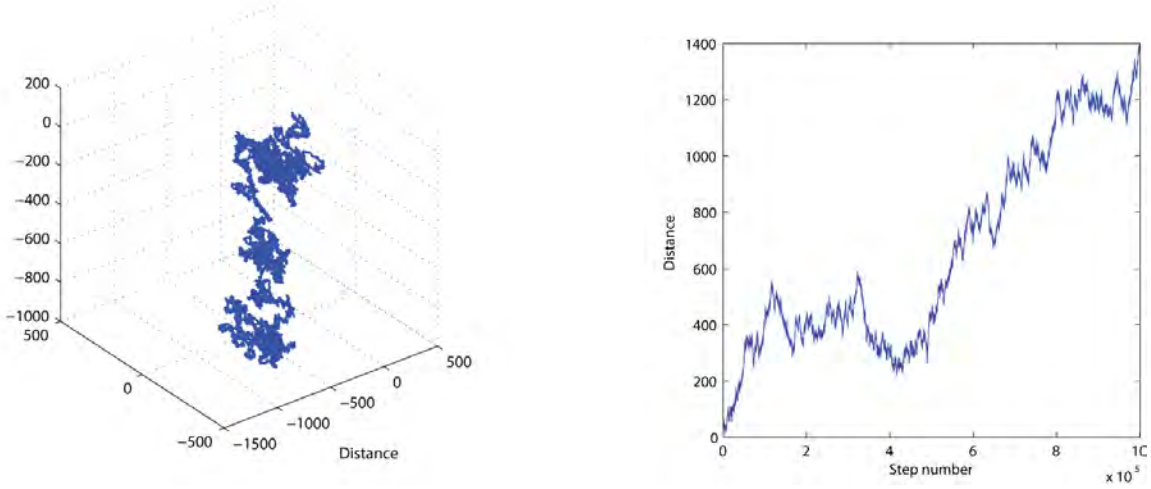

Figure 2.4: *Left:* Three dimensional random walk of one million steps. *Right:* Magnitude of distance from origin vs step number showing distance away from the origin increasing over steps.

2.4.2 Localisation length

As weak localisation occurs for closed loops the change in the diffusion constant is proportional to the probability of travelling in a closed loop during diffusion. The maximum volume in which the wave can be located is $\approx (4\pi Dt)^{\frac{d}{2}}$. For a wave travelling for time dt interference will occur in a cylindrical path of length $\frac{\hbar k}{m}dt$ and of cross-section $\approx \lambda^{d-1}$ providing a volume element $dV = \lambda^{d-1}\frac{\hbar k}{m}dt$. The probability of travelling in a loop is then given by integrating the ratio of these volumes over all relevant times. For a finite system of size L, with $L \ll L_\phi$, the integral is bounded from above by the time required for the wave to scatter diffusively across the system, $\frac{L^2}{D}$. The shortest relevant time scale is that between elastic scatterings, $\tau_e = \frac{l^2}{D}$, as otherwise non-diffusive behaviour will be involved. Thus the diffusion constant should be reduced by a factor proportional to

$$\frac{\delta D}{D} \approx -\lambda^{d-1}\frac{\hbar k}{m}\int_{\tau_e}^{\tau_\phi}\frac{dt}{(4\pi Dt)^{\frac{d}{2}}} \propto \begin{cases} -\frac{1}{l}(L-l) & d=1 \\ -\frac{1}{k\cdot l}\ln\left(\frac{L}{l}\right) & d=2 \\ -\frac{1}{k^2\cdot l}\left(\frac{1}{l}-\frac{1}{L}\right) & d=3 \end{cases} \tag{2.11}$$

Using (2.11) allows estimation of the localisation length in the weak scattering regime by setting the ratio equal to one and the system size to $L = \xi$, the localisation length. The result is that for one and two dimensions

$$\begin{aligned} \xi &\propto l & d &= 1 \\ \xi &\propto l \exp\left(\tfrac{\pi}{2} k \cdot l\right) & d &= 2 \end{aligned} \tag{2.12}$$

while for $d = 3$, ξ is infinite for weak scattering. In one dimension the wave will quickly become localised over some distance of order the mean free path, essentially meaning only a few scatterings are required to completely stop transport. In two dimensions the localisation length is exponentially large, meaning that the wave will travel diffusively within an area before being localised. In two dimensions the product of $k \cdot l$ manifests as controller of the size of area. For weak scattering the area is large and the wave will likely extend over the size of a sample; resulting in a system which appears extended. For the regime where $k \cdot l \approx 1$ the wave is localised over length scales of order the mean free path. To observe weak localisation, where the wave is localised after multiple scattering upon many modulations of the potential, one must work in a regime where $l \ll \xi < L$ giving $k \cdot l \approx 3 - 5$ depending on the system size.

2.5 The mean free path

The mean free path is the central quantity of the medium in determining the transport properties of a wave travelling through it. In nature disorder manifests itself in a variety of ways, for example impurities in a metal or random grain size in porous media. As the mean free path is a property of the medium one may expect it to have a varying form between systems and models. Some initial universal understanding can be obtained by examining the transition rate, $\frac{1}{\tau}$, between two states, given by the second golden rule [30]

$$\frac{1}{\tau} = \frac{v}{l} = \frac{2\pi}{\hbar} \left|\langle f| V |i\rangle\right|^2 \delta(E_f - E_i) \tag{2.13}$$

For a time-independent random potential one can set $V(\mathbf{r}) = W\nu(\mathbf{r})$ with W a constant specifying the disorder amplitude. In the Born approximation the matrix element simplifies to the Fourier transform of the scattering potential. For scattering into a continuum of states the delta function can be replaced with the density of final states, which for a two dimensional system is constant in energy and has the form $g = \frac{m}{2\pi\hbar^2}$. Making the appropriate substitutions and rearranging for l gives

$$\frac{1}{l} = \frac{m^2}{\hbar^4} \cdot \frac{W^2}{k} \left|\tilde{\nu}(\kappa - \kappa')\right|^2 \tag{2.14}$$

showing that for any potential which can be written as above, a $l \propto W^{-2}$ dependence can be expected for a given value of k. The k dependence varies through $\nu(\mathbf{r})$ and the Fourier transform $\tilde{\nu}(\kappa - \kappa')$.

The above discussion is altered by correlations in the potential, as seen in recent cold atom experiments using speckle potentials [7]. Atoms having a momentum larger than a cut off value were observed as being unaffected by the potential, inducing an effective mobility edge above which atoms behave as though in a extended or superfluid state. In the Born approximation one can consider an atom scattering from the spatial frequency in the disorder pattern that corresponds to its momentum. For a white noise potential one then has a spectrum which scatters all components equally. For a correlated potential the disorder has a finite spectrum and one can expect a cut off in the k components scattered by the disorder.

Correlations in the potential have the effect of altering the k dependence of the mean free path [31, 32]. For correlations over scale r_c the relevant quantity is kr_c. For $kr_c \ll 1$ the wave will experience an effectively uncorrelated potential while for $kr_c \gg 1$ the potential is correlated over several wavelengths and the wave experiences a smooth disorder potential. Consider a Gaussian random potential with correlation function

$$\langle V(\mathbf{r})V(\mathbf{r}')\rangle = W^2 \exp\left(-\frac{|\mathbf{r}-\mathbf{r}'|^2}{r_c^2}\right) \tag{2.15}$$

In the limit $r_c \to 0$ this reverts to a white noise potential giving l the k dependence of (2.14). Taking $kr_c \gg 1$ shows a $l \propto k^4$ dependence for a smooth potential, familiar from Rayleigh scattering. For a potential correlated as in (2.15), an analytical form for the mean free path can be found [32]:

$$\frac{1}{l} = \frac{\pi m^2}{\hbar^4} \cdot \frac{W^2 r_c^2}{k} G\left(\frac{k^2 r_c^2}{2}\right) \tag{2.16}$$

with $G(x) = \exp(-x)\left[I_0(x) - I_1(x)\right]$ in terms of the modified Bessel functions.

2.6 Experimental progress in the field

Early experiments of electron transport through solid-state disordered media typically relied on indirect measurements such as the electrical conductance of a sample. As discussed, in such experiments the interplay between interaction and disorder is not separable, making a clear study of disordered transport difficult. For reviews of such experiments see [33, 34].

Through the realisation that localisation arises as a wave transport phenomenon, more recent experimental studies have taken place across a variety of disciplines. For example localisation has been observed with microwaves [35] and light scattering, in which weak localisation [24, 36, 37] and, by increasing the scattering rate, Anderson localisation of light travelling through a bulk sample [38] have both been directly observed. The latter was achieved using a high refractive index powder as the scattering medium, reaching kl values of

approximately 1.5 [38]. More recently two dimensional Anderson localisation of light has been achieved [39]. Localisation effects have also been observed in ultra-sonic wave transport [40, 41]. This frequency range allows a variety of scattering media, including air bubbles moving through water (but appearing static over experiment timescales) and scattering by aluminium beads. The input from multiple disciplines is summarised in the conference proceedings of [42].

Although observation of localisation has been achieved, a thorough understanding of how interaction effects alter the system has not yet been produced. This has led to an influx of cold atom experiments aiming to produce Anderson localised samples of cold atoms within disorderd optical potentials. Although early experiments toward this goal observed diffusion and classical trapping [43, 44], in 2008 two breakthrough papers were released, both reporting Anderson localisation of a matter wave in one dimension [7, 8]. In [7] this was achieved using the optical potential arising from a speckle pattern to form the scattering medium. By measuring the fluorescence of the atom cloud when irradiated with probe light a direct measurement of the localisation envelope was achieved. Using this it was determined that atoms having above a cut-off momentum were not being localised by the disorder. As described in Section 2.5, this is due to a cut-off in the spatial frequency spectrum of the disordering speckle pattern and the atom cloud possessing a broad momentum distribution. To create the disordering medium in [8] two optical standing waves of incommensurate period were superimposed, creating a bi-chromatic lattice potential similar to a quasi-crystal. This gives a disorder potential which appears random over experiment length scales, but is in fact not truly random. The system has a spatial frequency very different from something resembling white noise. Rather than being directly analogous to Anderson localisation, the results from this paper are described by the Aubry-André model [45]. This predicts that with varying disorder strength the sample will undergo a transition from extended to a localised state despite the system being one dimensional. This was observed experimentally by dropping the atoms from the lattice and imaging the falling cloud. If released when in an extended, superfluid, state the resulting image is an interference pattern arising due to the phase coherence between the atomic wavefunctions on different lattice sites. When localised, coherence is lost and the resulting image is an incoherent superposition of the contribution from each site. By measuring the visibility of the interference pattern it is then possible to determine whether the state prior to dropping was extended or localised.

Progress has continued within the field, with further work focusing on higher dimensions [9, 46] and introducing interactions [11]. This has lead to matter wave Anderson localisation being realised in a three dimensional system by use of both the transverse and longitudinal correlations in a speckle pattern to form the disorder [9]. Using the bichromatic lattice technique of [8] in the presence of inter-particle interactions

has allowed [11] to begin exploring the phase diagram introduced in Figure 2.1. Between the two extremes of localised and extended a region of intermediate visibility is observed, corresponding to the appearance of locally coherent fragments.

2.7 Reaching localisation in two dimensions

As discussed in Section 2.4, two dimensional systems are of particular interest. The challenge of observing Anderson localisation in two dimensions arises from ensuring sufficiently strong scattering upon the disorder to localise the wave within the system size. As the localisation length scales exponentially with the product $k \cdot l$, this requires small enough k-vectors and a disorder potential capable of providing small enough mean free path.

The approach taken by [46] is to use a speckle pattern as the disordering potential. A transverse speckle grain size of $\sigma_y 0.8\mu$m is achieved. However, the beam is brought in at an angle, resulting in an asymmetric grain size, with the longer direction being determined by both the transverse and longitudinal correlation lengths. This gives a speckle pattern with an aspect ratio of $\sigma_x \approx 2\sigma_y$. This is used to measure asymmetric diffusion but would require smaller kl values to allow observation of localisation. This is certainly possible through either reduction of the atom cloud temperature or the speckle grain size. For example, the grain size used to achieve one dimensional localisation in [7] is $\sigma = 0.26\mu$m. The use of a speckle pattern as a disorder pattern is treated theoretically in [47, 48] and for the particular case of two dimensions in [49].

To provide transport through the system, speckle disorder experiments begin by confining the atoms in a tight trap to create a high inter-particle interaction energy [7, 46]. The trap is released the cloud allowed to expand over the disorder potential, converting the interaction energy to kinetic energy. The scattering length is chosen such that after expansion interactions are negligable. This creates an expanding cloud containing a broad spectrum of k values. Atoms having a larger k value have larger $k \cdot l$ and move more freely through the potential. Atoms with sufficiently low $k \cdot l$ are quickly localised by the potential. A useful cut-off value for this is $k_0^2 = \frac{2m\mu}{\hbar^2}$, with μ being the chemical potential in the trap prior to release [31]. In fact there is predicted to be no true cut off in two dimensions but having a low value of $k \cdot l$ allows achieving practical localisation lengths. As such, achieving a sufficiently small localisation length for k_0 is a good indicator as this means a large portion of the distribution will be localised within the system size.

The intended approach for producing two dimensional disorder in this experiment is to use a high resolution microscope objective to image a spatial light modulator pattern onto the atomic plane. This has the benefit of being an entirely reproducible and highly controllable potential. It is also easily adapted to study

different disorder potentials such as those required for producing Lévy flights. However, the grain size of the potential is limited by the resolution of the imaging system. This has a numerical aperture of 0.5, meaning a resolution of 532nm for 532nm light. Section 5.8 will use measured correlation lengths to assess the viability of using this system, with the expansion technique above, for achieving localisation.

CHAPTER 3

EXPERIMENTAL OUTLINE

3.1 Overview

Creating a cold atom experiment requires both decreasing the temperature and increasing the density of a hot vapour by many orders of magnitude. The goal is to increase the phase space density, the product of the density of the gas and its deBroglie wavelength, from of order 10^{-18} to 2.612, the critical value for achieving condensation in three dimensions. Many stages of sample preparation are required before the cloud enters the quantum regime. This chapter will discuss the techniques used in preparing the atomic sample for experiment, along with the apparatus used to perform each step. These are common between experiments requiring a condensate, although some have more or circumvent some steps, for example it is possible to achieve condensation by evaporating only in optical traps. For a mixture experiment each step must be repeated for each species. The experiment cycle for reaching condensation is shown in Figure 3.1.

First a magneto-optical trap (MOT) is loaded from the hot vapour gas, providing the initial cooling and increasing the density significantly. The experiment makes use of a 2D-3D MOT scheme in which atoms are first cooled in two dimensions to provide a beam of atoms. This is then used to load a second trap in which cooling takes place in all three spatial dimensions. Using a MOT temperatures can typically be reduced to of order 200μK, at atom densities of order $10^{10} - 10^{12}\text{cm}^{-3}$. At this point polarisation gradient cooling is applied using the MOT beams, lowering the temperature of the cloud to of order 50μK [50, 51]. The cloud is then cool enough to load efficiently into a magnetic trap.

As the experiment requires a separate chamber for magneto-optical trapping and use of the high resolution imaging scheme, primarily due to optical access, a magnetic transport scheme has been implemented. Atoms are loaded from the MOT into a magnetic trap provided by coils mounted onto a linear actuator. The coils

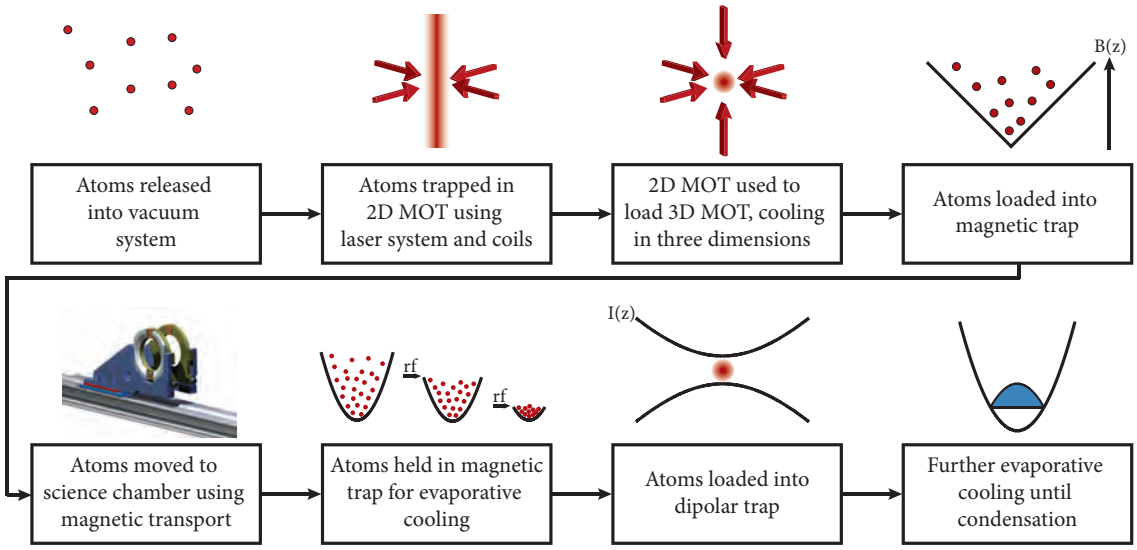

Figure 3.1: showing the experiment cycle for reaching condensation. Atoms are first loaded into a 2D magneto-optical trap. This is used to load a 3D magneto-optical trap, reaching temperatures of order 10μK. The cloud is then loaded into a magnetic trap. The coils forming the trapping field are moved through space using a linear actuator, transporting the atom cloud to the science chamber. Evaporative cooling is then performed until the cloud reaches sufficient temperatures for trapping in an optical dipole trap. In the dipole trap further evaporation is performed until condensation.

are then moved to the science cell with the atoms being carried in the magnetic trap. When using potassium and rubidium, potassium atom numbers are reduced by performing the cooling and trapping stages while in a background of rubidium [52, 53]. Although this is not a strong effect, being roughly a factor of 2-3 reduction, which is unimportant if using sympathetic cooling [54], it may be beneficial to have separate MOT chambers for each species. For initial construction the system was built using just one chamber for both species, with each being sequentially loaded into the science chamber. The system is designed to allow addition of a second cooling and trapping section for a new species or potassium.

With the atom cloud in the science chamber, evaporative cooling will be used to reduce the sample temperature to below the recoil limit. This is achieved through continuously removing the high energy tail of the Maxwell-Boltzmann distribution while allowing the cloud to rethermalise. Once the cloud has reached a sufficiently low temperature it can be loaded into a dipolar optical trap. Here further evaporation can take place until the quantum regime is entered. A general review of the field containing many of the experimental techniques can be found in [55].

In this experiment, the dipole trap will also serve the purpose of confining the cloud to a two dimensional plane. This will coincide with the focal plane of two high resolution microscope objectives. One of these will be used to image a spatial light modulator onto the atomic plane, allowing generation of exceptionally con-

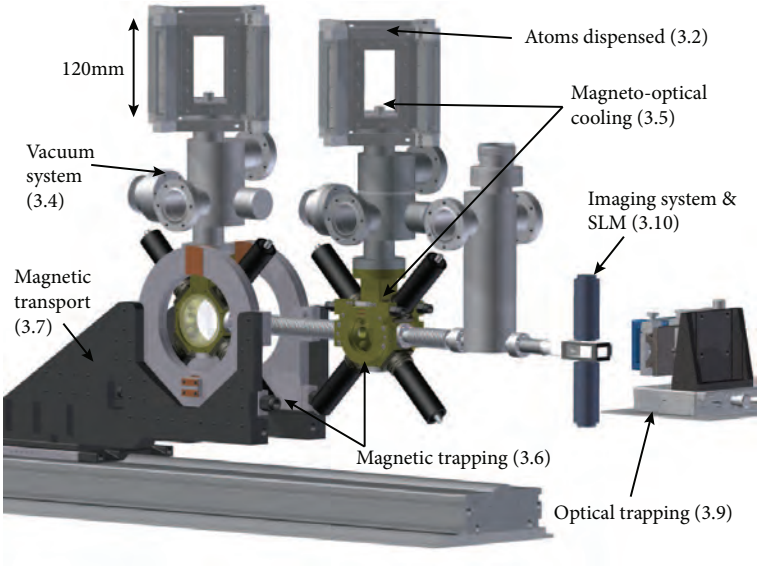

Figure 3.2: showing the layout of the experiment system annotated with Section numbers. Components of the vacuum system have been removed for clarity. Not shown in the diagram are the experiment control system (Section 3.3) and evaporative cooling (Section 3.8). The scale of the picture is indicated using the 2D MOT chamber which has a height of 120mm. Further points of reference are the separation between the transport coils (95mm) and the distance between the centre 3D MOT chamber and the science cell along the travel direction (approximately 350mm).

trollable patterns with high resolution, such as optical lattices or disorder potentials. The second microscope will permit high resolution imaging of the atoms held in the potential. As both the potential and imaging are produced with similar resolution, this scheme is intended to obtain resolution of single sites in an optical lattice, a feat achieved in [12, 13]. An overview of the experiment system and the chapter are given in Figure 3.2.

3.2 Atomic species

The atomic species used in the experiment are ^{87}Rb and ^{40}K, allowing production of cold clouds of bosons, fermions and mixtures. Evaporative cooling relies on a high rate of elastic collisions between atoms in order for them to quickly rethermalise. For a spin polarised fermionic cloud this is heavily suppressed due to Pauli-blocking of s-wave collisions at low temperatures. It is possible to cool fermionic species to sufficient temperatures by using a bosonic cloud as a thermal reservoir. Collisions between the two gases then cause rethermalisation during evaporation. For the specific case of ^{40}K and ^{87}Rb, the interspecies rethermalisation properties are excellent [56], making them a very appropriate pairing for a Bose-Fermi mixture experiment.

Another benefit of this pairing is the similar wavelength of their cooling transition, with ^{87}Rb having

a transition at 780nm and ^{40}K at 767nm [57, 58]. This allows for the two cooling laser systems to rely on similar techniques and technologies and also allows use of the same equipment in the laboratory. In particular, diode lasers are readily available in this wavelength range. The atoms are introduced to the system using commercial hot vapour dispensers containing alloys of rubidium or potassium.

3.3 Experiment control

During an experiment cycle there are many stages which require synchronised control of several entities at once and over small time scales. A simple example would be loading a magnetic trap from a MOT, which requires removal of all light and increasing of current supplied to magnetic coils. This includes synchronised switching of several shutters and electrical switching. A fast timing requirement could be, for example, pulsing detection light for absorption imaging. To provide this an experimental control system was developed [59]. The experiment control system makes use of a commercially available Field Programmable Gate Array (FPGA) system. The system controls 192 digital outputs and 16 analogue outputs, allowing management of the entire experiment system. The high-speed permitted by the FPGA system permits timing resolution of up to 25ns for digital and 1μs for analogue channels.

The control code was programmed using the visual programming language LabVIEW, although the FPGAs themselves do not use this language. It is comprised of three layers. The highest layer is the front end which allows a user to build a sequence of commands into time slots which activate sequentially. The main control software takes the control sequences from the front end software and uses them to allocate time slots which are transferred to the FPGAs. These then assign the output values of each digital and analogue channel accordingly.

The front end software has been developed to be extremely flexible. This was achieved by providing users with the ability to program their own experiment cycle in a flowing block diagram format. This is built up from a series of time slots during which the value of every digital channel is set on or off while analogue channels are either set to jump or ramp to a value over the time slot duration. This allows the user simple control over all of the available parameters of the experiment from a single user interface, allowing methodical optimisation of variables such as laser powers, detunings or MOT loading times. Control cycles can be saved and reproduced later, which is particularly useful when debugging a problem located in the experiment. For example, a control cycle with short MOT loading times can be run for optimisation of the 3D MOT loading rate. Once a set of time slots has been optimised to perform a particular goal, such as to perform detection imaging, they can be bunched into a single module which can be used in multiple control cycles.

3.4 Vacuum system

The vacuum system forms a central part of the experiment, around which the rest of the apparatus is built. The design and construction of this will be covered in detail in Chapter 4 and only the key points are introduced here, in particular those relevant to other aspects of the system.

The main role of the vacuum system is to provide a low pressure environment to allow long confinement times, through reducing losses caused by the background gas colliding with cooled atoms. Target pressures for regions needing long lifetimes are of order $10^{-10} - 10^{-11}$mbar.

The vacuum system has a modular design, with each atomic species being cooled and trapped in separate 3D MOT chambers before being moved through magnetic transport to a separate science chamber which has excellent optical access for further cooling and experiment. However, the system has initially been built with only a single trapping section providing sources for both ^{87}Rb and ^{40}K. This was to save on the time required for setting up multiple optical systems and allow initial testing of whether separate chambers are required.

The system has several key features to aid other aspects of the experiment. The system has separate chambers for trapping each species, in order to allow trapping of high atom numbers. The science chamber, a glass cell, is made to the required specifications of the microscope objectives. It also permits large optical access and has optical isolation between each face to prevent excess light bouncing in an effort to improve the contrast of the optical system. This is particularly important for fluorescence detection. To aid magnetic transport, the whole system has been kept unprecedentedly thin along the transport path. This has been achieved through the development of a specialised technique for bonding viewports to a titanium chamber using epoxy. The system also has flexible links between each modular section to allow careful alignment of the system. This is both to prevent issues caused during magnetic transport and to allow good alignment between centres of the 3D MOT and dipole trapping scheme such that the transport trap can coincide with both.

3.5 Magneto-optical trapping

The first stage of the experiment is loading a background vapour into a magneto-optical trap (MOT) [60]. This consists of paired counter-propagating laser beams impinging on the atom cloud while it is located in an inhomogeneous magnetic field. The effect can be understood by considering an atom placed in the path of a counter-propagating beam pair. At rest, the atom would absorb photons equally from each beam and

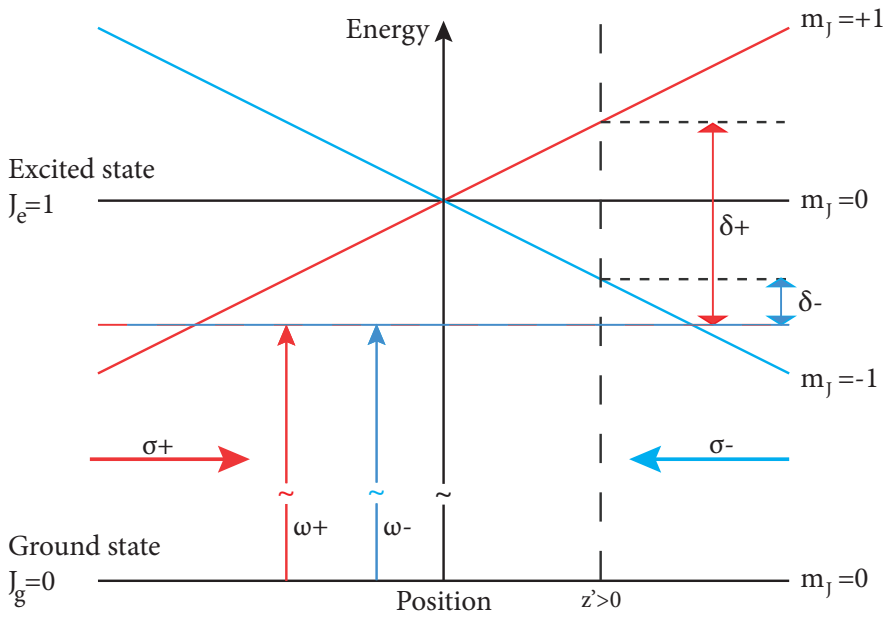

Figure 3.3: showing the cooling in a magneto-optical trap using the schematic level diagram of $J_g = 0$ and $J_e = 1$. Two circularly polarised counter-propagating beams are incident on the atom cloud which is placed in a linear gradient magnetic field. For values of $z > 0$ the $m = -1$ state is shifted toward resonance, increasing the number of photons scattered by the left travelling σ^- beam. For $z < 0$ the opposite is true.

have a momentum limited by that of the last photon to hit it. However, if the atom were moving toward one beam the laser frequency observed by the atom would be Doppler shifted. By choosing the laser frequency such that it is detuned below the atomic resonance the atom can be made to preferentially absorb from the beam that it is travelling towards, causing it to on average lose momentum.

In a MOT the preferential absorption is additionally made spatially dependent using a linear gradient magnetic field, $B(z) = Az$, to apply a Zeeman shift to the magnetic sub-states of the excited state. This is most simply demonstrated by considering transitions between a ground state with angular momentum quantum number $J_g = 0$ and an excited state with $J_e = 1$, as shown in Figure 3.3.

To address each of the $m = \pm 1$ states individually, two counter-propagating beams, each detuned below resonance with detuning δ and with circular polarisation of opposite sense, are set incident to the cloud. With the senses correct with respect to the field, for $z > 0$ the magnetic field then shifts the energy of the $m = 1$ sub-state upward and away from resonance while the $m = -1$ transition is shifted downward, closer to resonance. This reduces the rate at which photons are absorbed from the σ^+ beam, while increasing the absorption rate for photons in the σ^- beam, causing a larger net absorption of photons travelling towards the origin where both transitions have the same frequency. The opposite is true for the $z < 0$ side of the trap

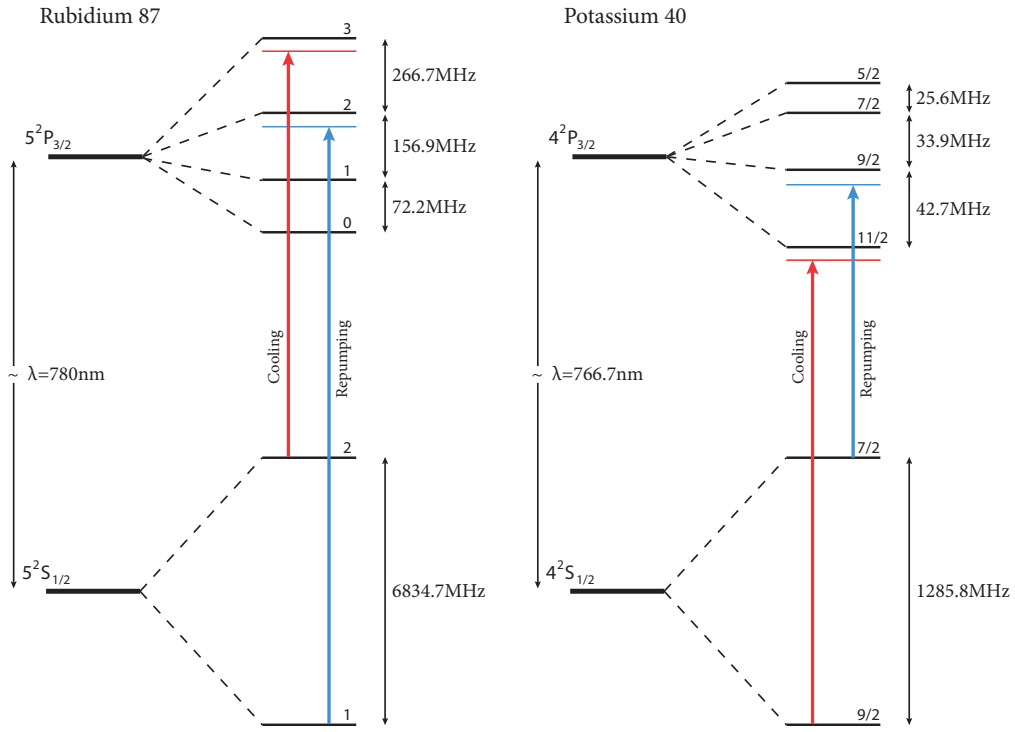

Figure 3.4: showing the hyperfine structure of the D_2 lines for ^{87}Rb and ^{40}K [57,58]. The cooling beams are used to reduce the momentum of atoms while the repumping light prevents atoms building up in dark states and being lost to the cooling cycle. For ^{87}Rb the cooling transition used is between $F = 2$ and $F' = 3$ with the repumping transition being between $F = 1$ and $F' = 2$. For ^{40}K the cooling transition is $F = 9/2$ to $F' = 11/2$ and repumping takes place between $F = 7/2$ and $F' = 9/2$

and by adding further beams the atom cloud can be cooled and compressed in all three spatial dimensions.

Laser systems

The laser system used to provide cooling light for magneto-optical trapping must allow use of a range of beams with laser frequencies suited to different tasks. First the cooling light must be detuned to the optimal point below resonance such that a large amount of atoms can be captured. The level scheme of an atom is not as simple as the $J_g = 0$ to $J_e = 1$ model, in reality involving multiple levels as shown for ^{87}Rb and ^{40}K in Figure 3.4, and includes dark states in which atoms build up. These atoms need to be pumped back into the useful states in order for cooling to continue, requiring a repumping beam. Aside from cooling, the laser system is also critical to several other stages. To improve the capture efficiency when loading the atom cloud into a magnetic trap it is necessary to pump ^{87}Rb atoms into the $|F = 2, m_F = 2\rangle$ state so more remain trapped by the field. For imaging of the MOT, it is necessary to tune the laser frequency to resonance to provide either a strong fluorescence signal or strong absorption image. Finally, due to the use of a 2D-3D MOT set-up, a pushing beam is required to increase the loading rate into the 3D MOT.

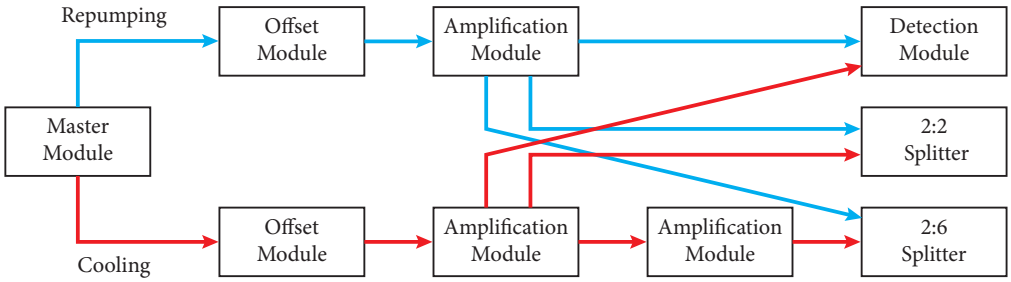

Figure 3.5: showing the work flow of the laser system used for cooling ^{87}Rb and ^{40}K.

To achieve these goals two laser systems were set-up, one to provide frequencies for ^{87}Rb and the other for ^{40}K. For a detailed discussion of the laser systems see [61]. The systems were built into modules, with each important part being contained in a separate aluminium enclosure. The laser light is transferred between modules and to the experiment using optical fibres. Building the system into modules allows stacking of the modules into a drawer unit, reducing the amount of optical table space required for the system. The modularity of the system not only allows for a compact laser system, but also makes it highly portable when compared to other systems, in principle relying only on recoupling of fibres once the system has been moved. To allow miniaturisation of the system, a custom range of optical mounts was used [61,62] with a much lower size footprint. The mounts are also highly stable, allowing infrequent realigning.

The workflow of the laser systems is shown in Figure 3.5, with both systems being identical in function. The master module provides a reference frequency to which the two offset modules can be locked. The reference frequency is obtained by locking an ECDL to a Doppler free spectroscopy cell. The offset modules then use an offset lock to set the appropriate frequency of two laser diodes, one for cooling and one for repumping light. Each beam is directed through an amplification module containing a tapered amplifier (TA) to increase the power of the beams from 5-10mW to of order 1W, with part of the cooling light being passed through another amplification module due to having higher power requirements. The light is then distributed between three paths. First, one output of the cooling light and one of the repumping light are passed into the 2:2 splitter module which takes the two beams, overlaps them and then gives out two beams containing cooling and repumping light used to produce a 2D MOT. Another output of cooling and repumping light is given to the detection module, which has outputs to provide the pushing beam, optical pumping for magnetic trapping and light used for imaging. Finally, some of the cooling light is passed through a second amplification module before being passed to the 2:6 splitter module where it is overlapped with repumping light and used for generating 3D MOTs. Each of the 2:2, 2:6 and detection modules have an acousto-optical modulator to provide fast control over switching and amplitude modulation, as well as the frequency of

output light. This also allows different detunings between, for example, the pushing beam and the 2D and 3D MOT beams. However, beams from the same module have the same detuning meaning that, for example, the pushing beam and imaging beams are always set to the same detuning.

To facilitate the production of MOTs for both species in the same chamber of the vacuum system, 50:50 fibre splitters were used to overlap the light of the rubidium and potassium laser systems. These consist of four inputs, the cooling and repumping light for each species, and two outputs each providing one counter-propagating beam pair for the 3D MOT or both retro-reflected beams for the 2D MOT. This approach allows the same lens tubes and same 2D MOT optical system to be used for each species. The splitters have a measured output of 50:50 for the rubidium light but are less evenly divided for the potassium light, with variations on the order a few per cent. The output light power of the system is 8mW (19.6mm diameter at 13.5%) for each 3D MOT beam or 40mW (over 5cm by 2cm) for each 2D MOT beam.

3.6 Magnetic trapping

The atoms are subjected to magnetic fields during the majority of steps during both sample preparation and experiment. As mentioned in the previous section, an inhomogeneous magnetic field is required for producing a 3D MOT. However, purely magnetic traps are also used in the experiment, providing the ability to transport the atoms from one section of the vacuum system to another and allowing evaporative cooling. A neutral atom can be trapped using the interaction between a magnetic field and its magnetic moment, $\vec{\mu}$, with a field $\vec{B}(\vec{r})$ providing a trapping potential [60]

$$V(\vec{r}) = -\vec{\mu} \cdot \vec{B}(\vec{r}) = g_F m_F \mu_B |\vec{B}| \tag{3.1}$$

with g_F the Landé g-factor and μ_B the Bohr magneton. The signs of g_F and m_F then give rise to two types of field sensitive state; high-field seekers and low-field seekers which move to regions of either high or low field respectively. Low field seekers can be held in a field minimum while high field seekers are lost as no field maximum can exist in free space.

The magnetic trap used for transport and evaporation, and also the 3D MOT field, is a quadrupole field formed by two identical coils carrying currents of opposite sense. This has a single zero located at the origin and a field profile near the origin given to first order by [63]

$$B = B' \sqrt{x^2 + y^2 + 4z^2} \tag{3.2}$$

with B' being the gradient in the weak direction. A gradient of approximately $2B' = 10-20$G/cm is required for producing a MOT for rubidium or potassium or of order $2B' = 140-180$G/cm for magnetic trapping. A wire loop of radius R, having N turns and carrying current I, has a field profile along the z-axis of:

$$B_{x,y=0}(z) = \frac{\mu}{4\pi}\frac{2\pi R^2 NI}{(z^2+R^2)^{\frac{3}{2}}} \tag{3.3}$$

By placing two such wire loops concentrically with a separation of d one can construct a coil apparatus capable of either creating strong linear gradients or highly homogeneous fields simply by reversing the current in one of the loops. For two coils carrying current in the same sense the odd terms of the Taylor expansion of (3.3) are all zero by symmetry. The largest contribution to the field then comes from the from the first term in the expansion, having the form $B_0 \propto \frac{NI}{R}$, providing a field constant in z up to $\mathcal{O}(z^2)$. This contribution can be removed by setting $d = R$, the Helmholtz condition, creating a field homogeneous up to $\mathcal{O}(z^4)$. Such a field is used in experiment to provide a field suitable for tuning the atomic scattering length, controlling the interaction strength between atoms. This relies on use of a Feshbach resonance, typically requiring homogeneous fields of order 1100G for some ^{87}Rb and ^{40}K resonances. As the scattering length is very sensitive to the magnetic field when near a Feshbach resonance, a highly homogeneous field is required to provide near constant interaction strength across a cloud. Another use for such a field is the cancelling of stray fields around the experiment. This is vital when making use of Feshbach resonances to provide a homogeneous environment, but also for molasses cooling. The presence of a stray field would otherwise cause atoms to be lost on being irradiated by the molasses beams.

Another important field profile is a gradient field, used to provide a spatial detuning dependence during magneto-optical cooling or a trapping field for magnetic trapping. This can be achieved by having two coils carrying current in the opposite sense. In this case the even terms of the Taylor expansion of (3.3) are removed by symmetry. The first order contribution then has the form $B' \propto \frac{NI}{R^2}$. It is worth noting that the linearity of the field can be improved by choosing $d = \sqrt{3}R$, removing the third term and giving a linear field up to $\mathcal{O}(z^5)$. However, for magnetic trapping it is typically preferable to optimise to have a steeper gradient, rather than more linear, to achieve tighter trapping. For a given separation this is typically achieved for a coil having a radius equal to approximately half the separation [64].

One caveat of using a quadrupole field for trapping is the presence of a zero field point at the centre. Around this point the orientation of the atom magnetic moment cannot follow the field adiabatically leading to transitions between magnetic sub-states, potentially causing an atom in a low field seeking state to undergo transitions to an un-trapped state and to be lost from the trap [65]. Such transitions only occur when an

atom travels near to the centre, and only cause a relevant loss rate for atom clouds with temperatures of order 40μK [66, 67]. Several experimental efforts have been undertaken to prevent such losses. One example is to use an optical beam to prevent atoms from travelling near the zero point [2]. By use of a far detuned beam heating is somewhat avoided. However, implementation of such a technique would be problematic in the experiment system due to the need for magnetic transport. Another technique is to produce a time-orbiting potential trap (commonly known as a TOP trap) [1, 67, 68]. This is achieved by applying an oscillating bias field on top of the quadrupole trap using a pair of Helmholtz coils. The result is that the minimum field point moves around the trap, causing the low field seeking atoms to follow it. If the bias field is rotated faster than the magnetic trap frequency (but still slower than the Larmor frequency to ensure adiabaticity) the atoms the atoms are held in the centre of the trap. Another approach is to magnetically shift the trap such that the minimum corresponds to a non-zero field. This can be achieved using a Ioffe-Pritchard trap (IP) [69, 70] formed from a Helmholtz coil pair and four wires directed along the symmetry axis of the coil pair. The wires are spaced equally, with adjacent wires carrying opposite current. The wires then form a two dimensional quadrupole field. Another similar scheme is the use of a quadrupole Ioffe-Pritchard configuration (QUIC) [71]. This uses an anti-Helmholtz coil pair with a third coil. The third coil has its axial direction perpendicular to the anti-Helmholtz pair and is used convert the trap to a configuration with a similar profile to that of a Ioffe trap. Although this trap is exceptionally simple to create for a static trap, the added complication of the third coil prohibits simple implementation into the experiment. These techniques have the advantage of allowing cooling to lower temperatures in the magnetic trap without incurring excessive losses. However, to prevent added complications in the magnetic transport design of the experiment, a pure quadrupole trap is currently used. To prevent high losses only initial evaporative cooling will be performed in the magnetic trap. Once sufficiently cooled the atoms will be loaded into a dipolar trap where further evaporation can take place.

Magnetic field generation

The magnetic trap used for transport is loaded from the 3D MOT. To allow efficient transfer of atoms from the MOT to a magnetic trap the centre of the two fields must be well aligned. This presents two options, either using the same coils for magnetic transport and the MOT, or having two separate coils. The latter option is preferable as it allows loading of a MOT for another species while the transport coils are in motion. This means that during the loading stage, the two coil pairs must be concentric with one placed in between the other. As the Feshbach coils will be located close to the vacuum system, the MOT coils were designed to fit between the transport coils. This is also convenient as the transport coils require various appendages,

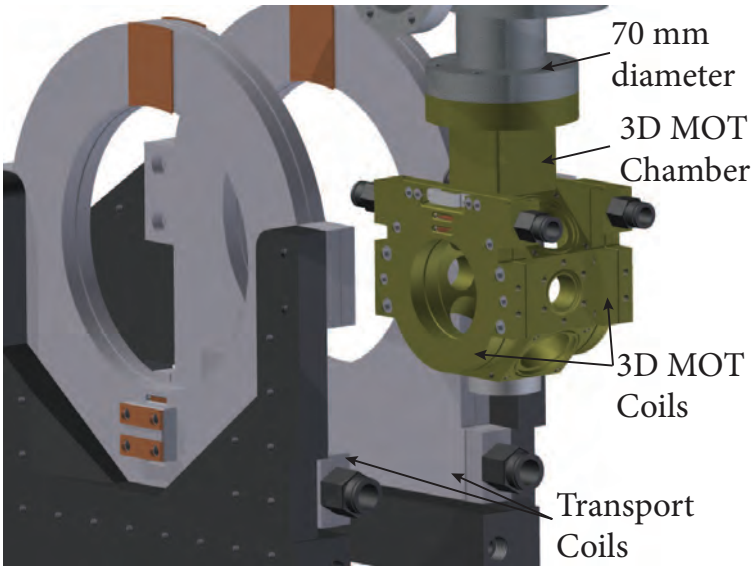

Figure 3.6: showing the positioning of the magnetic coils for producing 3D MOTs and magnetic transport. The scale of the drawing is given by the 70mm diameter of the CF35 vacuum flange. Further points of reference are the separation of the transport coils (95mm) and their central radius (83.7mm).

such as current cables and cooling oil piping, which move with them during motion. Figure 3.6 shows the positioning of the coils.

As can be seen from the form of B', increasing the separation of the two coils causes a rapid increase in the current required to reach a given gradient, which in turn leads to excessive heat generation. This problem is exacerbated somewhat by the microscope objectives used for high resolution imaging. As can be seen in (3.2), a quadrupole field has both a strong gradient (in the $z-$direction) and a weak gradient (in the $x-y$ direction). Gravity skews a magnetic trap, reducing the trap depth in that direction. Due to this, experiments usually mount their coils such that their strong gradient is against gravity. However, the confining 2D lattice or experiment plane must be aligned such that it is at the same height with respect to gravity, to prevent a skewing of the lattice. The objectives must then be mounted parallel to gravity, and would then cause an obstruction for the transport coils when they move to the science cell. This could not be avoided without using excessively large coils, meaning a factor of two increase in the required weak gradient.

A narrow spacing between the coils was used to avoid requiring excessive cooling of the transport coils. The main occupiers of space between the coils are the 3D MOT coils and the 3D MOT chamber itself. The chamber was kept exceptionally narrow, having a profile of 36mm compared to of order 100-150mm for a standard chamber, by constructing the chamber using the epoxy bonding technique as mentioned in Section 4.3.2. The coils themselves were kept compact through use of two key design features which were applied to

both the 3D MOT coils and the transport coils. The construction of the coil and cooling body is shown in Figure 3.7L.

Firstly, to reduce the required cooling per coil, the copper density of each coil was maximised. Rather than using standard wire, or hollow wire, a flat copper ribbon was used for the coil windings, with each winding being separated by a thin layer of kapton. The downside to this is that cooling can only be provided at either edge of the ribbon, meaning a smaller cross-section for the cooling system to work on. The coil was wound with many stacked windings, but with a depth of only one winding, to reduce the thickness of the coil. Each coil was wound by hand turning a lathe to wind the copper ribbon onto an aluminium former with epoxy being applied between the turns. The epoxy was cured by passing a current through the coil to induce Joule heating. The aluminium former was then machined away on each side in turn, also removing a small portion of the coil to produce well defined edges. The coil surface was then finely polished and etched to prevent connections between turns.

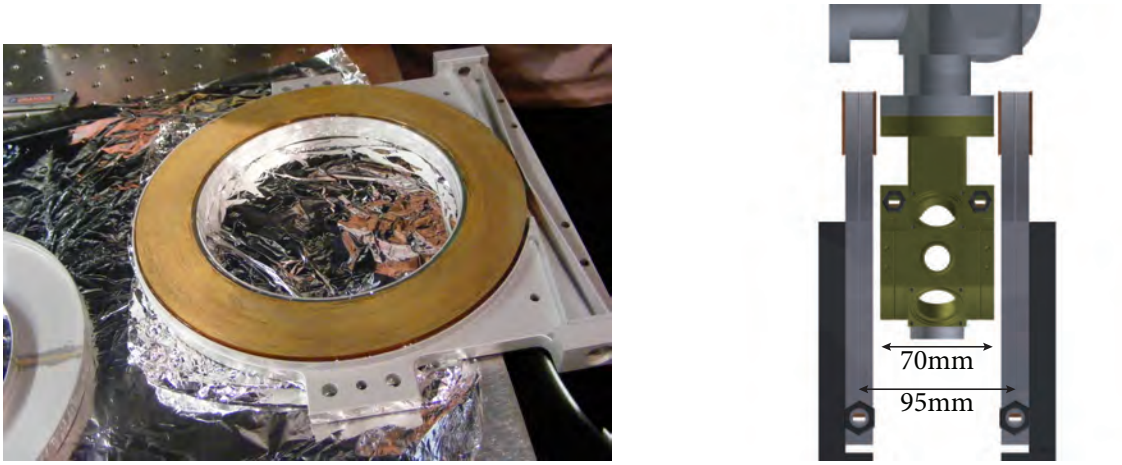

Figure 3.7: *Left:* showing the cooling body of the transport coils. The transport coil is first wound and prepared and then placed onto spacers. The coil is then fixed into one half of the cooling body using an adhesive which also seals the cooling channel. Once this has cured the exposed faces of the cooling body half are painted with more adhesive and the second half is lowered onto the coil. This is fixed in placed with bolts and cured. *Right:* showing the spacing of the transport coils using this coil body design. The 3D MOT chamber has a width of 36mm while the 3D MOT coil cooling bodies have widths of 17mm.

The second feature was use of a compact cooling body that allowed flow on either side simultaneously through a narrow channel. Cooling on just one side would result in a large thermal gradient over the copper ribbon, causing an increase in the resistance of the ribbon toward the hotter side. This would cause more current to flow on the cooled side of the coil, resulting in a time varying centre in the current distribution, and therefore effective separation of the coils. This was of particular concern for the Feshbach coils due to

the narrow width of some resonances. Cooling on both sides allows even cooling of the coil and reduces the temperature differential across the ribbon. Each body was constructed of two parts, with the coil being fixed to one half first, while held in place by water soluble spacers. Adhesive was then applied to the cooling body and the second half lowered over the coil. Once the epoxy was cured the spacers were then removed by flooding the cooling body with water. The 3D MOT coil cooling bodies were constructed from titanium while the transport coils used slotted aluminium.

The MOT coil cooling bodies have a profile of just 17 mm, meaning a total separation of 53mm between the coil centres. These were made with a coil of radius 32.2mm and 20 turns. For producing a 3D MOT the coils run at around 10A providing a gradient of around 16G/cm. The 3D MOT coils mount directly onto the vacuum system to save space, using nylon bolts and having a layer of kapton sheet between surfaces for isolation, giving a total profile of 70mm when mounted on the 3D MOT chamber. The transport coil body is slightly thicker at 21mm. Having 2mm of free space on either side then gives a separation of 95mm between the coil centres. They have a radius of 83.7mm with 90 turns providing, a gradient of 1.4G/cm per Amp of current as measured with a Hall probe. The coils are clearly not designed to optimise their gradient, but instead use a larger radius due to restrictions on optical access caused by the dipole trapping scheme. Roughly a factor of two larger gradient could be reached using coils having radius ≈47mm. Figure 3.7R shows the placement of the coils relative to the vacuum system. The Feshbach coils (currently in construction) were designed to have close to a Helmholtz configuration, having separation $\approx 0.99R$. A radius of 56.7mm and 70 turns then provides a homogeneous field of 11.8G per Amp or a field gradient of 2.5G/cm per Amp if in a gradient configuration. The radius is kept small to allow close proximity to the vacuum system, reducing the current required for high fields and to allow access for the transport coils.

Stray magnetic fields are cancelled through use of three Helmholtz coil pairs with orthogonal axes. The current flowing through each pair can then be adjusted to provide an isolated region at the centre with uniform background field. This is achieved in practice by loading a MOT and removing the trapping field. Each coil pair can then be adjusted such that the expansion of the atoms is uniform, rather than flowing through a preferred or distorted path. The compensation coils are also located between the transport coils. These are fixed to two Perspex sheets to add stability and prevent them moving into the path of the transport coils. The Perspex sheets can be fixed to the clamp used to align the 3D MOT using two countersunk screws or onto the outside of the 3D MOT coils.

The transport and MOT coils are powered using Delta Electronics power supplies giving up to 100A, 60V and 100A, 30V respectively. The coils are switched at high speeds by using an IGBT circuit rather than

the power supplies directly to control their output state (although current magnitude is still altered through addressing the power supplies). This operates by cutting the connection to the power supply and instead allowing current in the coil circuit to decay through a varistor. To provide cooling Paratherm CR58 cooling oil is pumped through the cooling bodies at a flow rate of up to 10l/min.

Due to the resistance of the transport coils they are in practice limited to a maximum current of approximately 90A when pulsed, dropping to 80A when used continuously due to increased resistance through heating. This allowed a strong direction gradient of $2B' = 112 \pm 5\%$G/cm when used continuously, as measured using a Hall probe. This is lower than many other experiments, which typically rely on strong gradients of order 140-180G/cm. This is particularly important when recalling that it is the weak direction defining the trap depth in the direction of gravity, meaning a further factor of two lower gradient than stated. As discussed later in Chapter 6, this did not provide a sufficiently tight trap to prevent atoms hitting the chamber walls during magnetic transport. Additionally, the rethermalisation time during evaporative cooling was too slow for effective evaporation. For this reason the transport coils have been redesigned to optimise the gradient at a specified separation, with the coil inner radius now being 44mm. As the coil radius has been decreased by roughly a factor of two, a corresponding factor of increase in gradient can be expected. To increase the gradient further the coils have been designed to allow higher currents and, through changes to the cooling body, to have a smaller separation. For more specific details on the construction of the coils, calculations of field geometries and simulations towards magnetic trapping see [61].

3.7 Actuation for magnetic transport

Magnetic transport can be achieved either using multiple static coils with time varying currents [72], moving a magnetic field minimum in space, or by moving a pair of coils which produce a static field [54, 73]. The moving coil option was chosen due to its relative simplicity, meaning the transport coils required mounting onto a linear actuator. For a complete system this would have several stops, beginning at the 3D MOT of one species, moving the atom cloud to the science cell, then repeating the process for another species.

The actuator needs to have a high repeatability to prevent the stopping points varying from cycle to cycle. This is important as the centre of the transport coils must be routinely brought back to the 3D MOT centre for efficient loading, but more critically, so that the centre can repeatedly coincide with the position of the dipole trap, which has a beam waist of 10μm. The actuator must also be fast enough that losses during travel are not relevant, and experiment cycle times can be kept low. Due to the short distances between stops acceleration is more relevant than absolute velocity. It also requires a travel distance sufficient to cover

all the stops needed for multiple species.

The actuator chosen was a ball-screw linear actuator manufactured by Parker, 406XR-1200. This was used over a linear motor, which generally have higher specifications, to minimise magnetic field gradients along the transport length. The actuator has a repeatability of $\pm 5\mu$m and, through use of an encoder which measures the rotation of the motor, a position measurement accurate to 2.15μm. The maximum speed with the chosen motor is 0.875ms^{-1} with a maximum acceleration 20ms^{-2}. In practice neither of these values are reached over the current travel distance, 350mm, between the MOT and science chamber. The maximum acceleration reached 6ms^{-2} is limited by motor torque and vibrations in the load. This allows the transport coils to move between the 3D MOT chamber and the science cell in 0.7s. The total actuator travel length is 1200mm, allowing for the future inclusion of three species in the system without changing the actuator. For characterisation and programming of the actuator system see [59].

When using an actuator the specifications of accuracy, repeatability and lifetime, are best met when the load is bourne centrally on the moving platform. However, the under-side of the science cell must be free for access for one of the microscope objectives and to allow fixing the cell position relative to the optical table. Thus the coils are be mounted such that they are displaced forward from the moving platform, allowing them to protrude past the end of the linear actuator when they are positioned at the science cell. The actuator is mounted so that it rests upon a flat surface along the whole travel length. Rather than mounting directly onto the optical table, a 15mm intermediate base plate was used. This allows the option of replacing the base plate with vibrational damping, should it be necessary at a later stage.

The transport coils are mounted at a centre height of 265mm above the optical table surface, so as to coincide with the centre height of the vacuum system. To hold them at this height an aluminium chassis was constructed, see Figure 3.8. This was in turn mounted on to an aluminium plate which connected directly to the moving platform of the actuator. The connection to the aluminium plate uses brass sliding blocks, allowing the separation of the transport coils to be adjusted over 30mm.

The aluminium chassis was designed to rigidly hold the transport coils without impacting on the optical access they allow, or increasing their profile along the transport direction. Due to the cooling body of the coils being designed such that the cooling oil travels into and out of the body along the travel line of the experiment, the oil needed to be brought back in the opposite direction. This was achieved using a simple aluminium u-bend and having the cooling oil pass through a long bore in the aluminium chassis itself. The chassis also allows for mounting the housing used to attach the flexible chain which guides the hoses and cabling used to supply the coils. See Figure 3.9 for the assembled transport system.

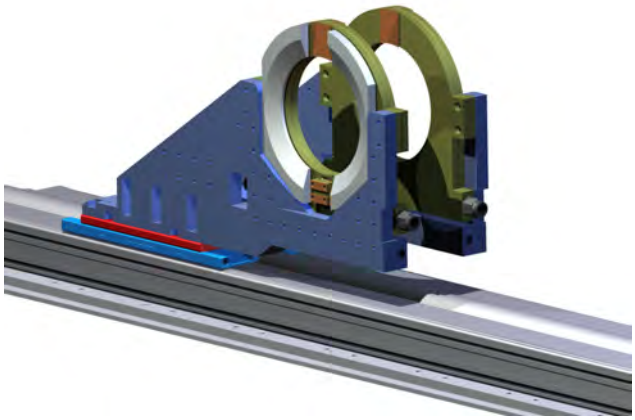

Figure 3.8: showing the transport coil system mounted to provide a centre height of 265mm to coincide with the trap centre of the 3D MOT coils. The transport coils are mounted onto two rigid anodised aluminium bodies, shown in blue, which also provide mounting points for electrical connections and for the flexible chain used to guide piping and cables during motion. The transport coil mounts are mounted onto a base plate, shown in red, which allows alteration of the coil separation using sliding blocks. This fixes directly onto the carriage of the linear actuator, shown in bright blue. The linear actuator is mounted onto a 1.2m long, 15mm thick aluminium base plate. For scale, the separation of the coils is 95mm and their radius is 83.7mm.

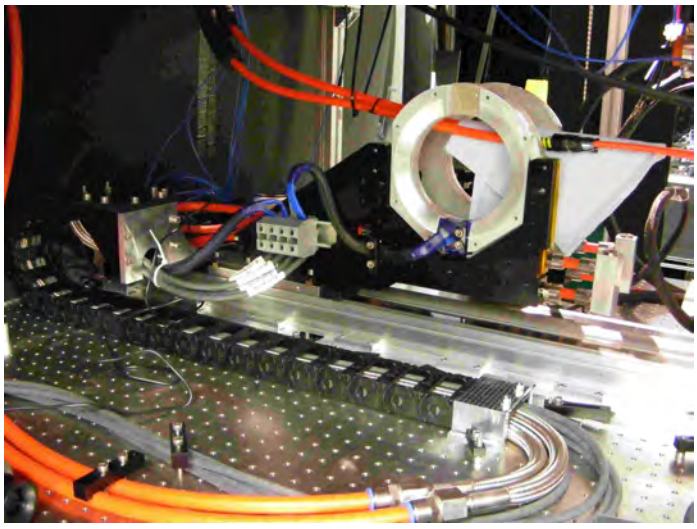

Figure 3.9: showing the assembled magnetic transport system. Due to the inline oil flow design of the transport coils the aluminium mounts also serve as the backflow line for cooling oil. To allow this, two simple U-bends are mounted in front of the transport coils. The flexible chain is used to guide two corrugated steel hoses and four power cables during motion

3.8 Evaporative cooling

Laser cooling allows reaching of temperatures of order μK with low atom losses. The lowest temperature achievable is given by the energy from absorbing a single photon, which is then emitted in a random direction through spontaneous emission. This leaves a residual momentum of order $\hbar k$ on the atom. Further to this, as the sample cools and occupies a smaller region of the trap, the density increases. If compressed to the point where light scattered by an atom is reabsorbed by another an effective repulsion appears between the atoms. The increased density of the cloud also increases the rate of collisions between the atoms. The collision rate between a ground state atom and one in the excited state is much faster at lower temperatures than the rate for two ground state atoms. The ground-excited state collision is typically inelastic, meaning that using near resonant light increases the loss rate of atoms from the trap.

To circumvent these issues evaporative cooling is employed [67, 74, 75]. This technique relies on selectively removing the hottest atoms from the trap, such that the average temperature drops. The distribution of energies in a classical gas is given by the Maxwell-Boltzmann function. This has a long tail which describes a small number of atoms having a very high energy. By removing these atoms and then allowing the cloud to rethermalise the distribution is then reproduced with a lower average value. The important timescales are the rethermalisation time of the cloud, which is determined by the elastic scattering rate and the trap depth ramping time. If the trap depth is reduced faster than the rethermalisation time the high energy tail of the Maxwell-Boltzmann profile is not reproduced and more atoms are removed from the trap than necessary. If the trap depth is lowered slower than the cloud can rethermalise then inelastic collisions lead to loss of atoms again making the process inefficient. As the temperature lowers the density increases, achieving both goals toward reaching a high phase space density simultaneously.

For successful evaporation the rate of elastic collisions must be approximately 150-200 times faster than that of inelastic collisions [75]. Inelastic collisions are caused by many processes, for example collisions with the background gas of the vacuum system or three-body recombination. For a given density the rate of these is constant at low temperatures. The elastic collision rate depends on the relative velocity between particles, therefore reducing with temperature. This results in the ratio of elastic to inelastic collisions decreasing with temperature.

Experimental procedure

To perform evaporative cooling the trap depth must be lowered in a controllable fashion. For evaporative cooling in a magnetic trap this is achieved through forced evaporative cooling, in which an RF antenna is

used to induce transitions between trapped and untrapped magnetic sublevels. This provides a much more controlled approach compared to reducing the current in the coil as only the trap depth is altered, rather than the gradient of the trap. The highest energy atoms can occupy regions of the trap where the field is stronger, meaning a larger Zeeman shift. By ramping the antenna from a high to low frequency, only the higher energy atoms undergo transitions to untrapped states with which the RF field is made resonant. The antenna used for this is a simple loop of wire mounted onto a heat sink to provide cooling for a load resistor. The signal is generated by a direct digital synthesiser signal which is passed through an RF amplifier. In the dipole trap, evaporation can be achieved through reduction of the laser power directly.

3.9 Optical trapping

Atoms which have been sufficiently cooled can also be trapped through the electric dipole interaction with non-resonant light. This provides traps generally much weaker than magnetic traps, with a typical trap depth being of order mK. When laser light is shone onto an atom the electric field, **E**, induces an atomic dipole moment, **d**, which oscillates at the laser frequency, ω, having an amplitude [76]:

$$d = \alpha E \tag{3.4}$$

where α is the atomic polarisability. The interaction potential of the induced dipole moment arising from the interaction between the atom and laser, of intensity $I(\mathbf{r})$, is then given by:

$$V_{a-l}(\mathbf{r}) = -\frac{1}{2}\left\langle \mathbf{dE}(\mathbf{r},t)\right\rangle = -\frac{1}{2\epsilon_0 c}\Re\left(\alpha\right) I\left(\mathbf{r}\right) \tag{3.5}$$

Another important quantity for an optical trap is the rate at which photons from the trapping beams scatter with an atom in the cloud. This provides the lifetime for atoms held in the dipole trap. This is calculated through the amount of power absorbed by the cloud:

$$\Gamma_{sc}\left(r\right) = \frac{P_{abs}}{\hbar\omega} = \frac{1}{\hbar\omega}\left\langle \dot{\mathbf{d}}\mathbf{E}(\mathbf{r},t)\right\rangle = \frac{1}{\hbar\epsilon_0 c}\Im\left(\alpha\right) I\left(\mathbf{r}\right) \tag{3.6}$$

Through calculation of the atomic polarisability and use of the rotating wave approximation, the potential and scattering rate simplify to [76]

$$V_{a-l}(\mathbf{r}) = \frac{3\pi c^2}{2\omega_0^3}\left(\frac{\Gamma}{\delta}\right) I(\mathbf{r}) \tag{3.7}$$

and

$$\Gamma_{sr}(\mathbf{r}) = \frac{3\pi c^2}{2\hbar\omega_0^3}\left(\frac{\Gamma}{\delta}\right)^2 I(\mathbf{r}) \tag{3.8}$$

where δ is the detuning of the laser frequency from resonance and Γ is the spontaneous scattering rate which is dependent on the atomic species, for ^{87}Rb $\Gamma = 2\pi \cdot 6.06$MHz [57]. The appearance of the detuning shows that atoms would prefer to sit in bright areas for a red detuned beam and the inverse when blue detuned. The potential depth created by a laser beam is directly proportional to the beam intensity meaning a condensate would experience an optical potential dependent on the spatial distribution of the beam. This is of critical importance not only for the production of optical lattices, but also for the production of the majority of disorder potentials through choice of a random distribution for $I(\mathbf{r})$.

Optical trapping scheme

Optical trapping is used to confine the atom cloud to a 2D plane. To provide a 2D light sheet a beam is created with an astigmatic focus. This is produced by using a 200mm focal length aspheric lens to focus down a collimated beam of waist 12.3mm, and thus a region of high intensity. A low power cylindrical lens of focal length 5150mm is then placed into the beam to provide a weak astigmatism. The result is two foci separated in space, one in the vertical plane at a distance of 192mm from the aspheric lens and another in the horizontal direction after 200mm. The horizontal focus can then be used as a 2D potential. This approach is simpler than the more commonly used crossed beam trap as it only requires aligning one beam to the centre of the transport trap. For characterisation of the optical trapping beam and optical system see [59].

Optical lattice scheme

With the cloud confined to two dimensions, the high resolution imaging system and spatial light modulator introduced in the following section can be used. The spatial light modulator is used to provide versatility in the choice of potentials, for example lattices of differing geometries. The final step in the trapping scheme is then to image the spatial light modulator onto the two dimensional cloud and choose the potential relevant for the experiment. To allow imaging of single sites in a lattice a minimum length scale of 780nm must be used for the potential as that is the resolution limit for fluorescent light.

Dipole trapping laser system

The laser system providing light for the dipole trap uses three fibre amplifiers to boost the power of a 1550nm diode laser seed. The seed, which can operate between 1 and 15mW when used with the amplifiers, is split into three components which are each passed through an AOM to allow frequency shifts between the three

beams. Each component beam is passed through a fibre amplifier, boosting the light power up to a maximum of 10W per beam. To allow high speed switching, the output of the fibre amplifier is passed through a high power AOM before being coupled into an optical fibre connected to the optical system for producing the dipole trap.

3.10 High resolution imaging system and spatial light modulator

Two of the major features of this experiment are the dual microscope set-up, designed to achieve resolution of single sites of the optical lattice, and the use of a spatial light modulator (SLM) for manipulating atoms . These will be discussed in Chapter 5 and are only introduced here for completeness.

The main component of the imaging system is a pair of commercially available 50x microscope objectives with long working distance and corrected for use through glass of thickness 3.5mm. These two features allow them to be used externally to the vacuum system. They have a numerical aperture of 0.5, allowing resolution of 532nm for 532nm light.

By positioning one objective above the 2D experiment plane and the other below, high resolution can be achieved for both imaging and manipulating atoms. This grants the option of imaging the demagnified SLM distribution directly onto the atom cloud, creating a highly controllable potential landscape. This creates the possibility of studying dynamics in the vast majority of conceivable two dimensional potentials. For example, the SLM could be used to create highly complex lattices, or lattices of varying spacing without any need to realignment of the optical system. It could of course also be used to produce random potentials of various types for studying disordered transport.

CHAPTER 4

VACUUM SYSTEM

4.1 Introduction

The cooling of gas clouds to temperatures below the mK level requires that they are isolated from thermal atoms at atmospheric temperature and pressure. This is achieved through use of an ultra-high vacuum (UHV) system, an enclosed volume in which the pressure can be fourteen orders of magnitude lower than the surrounding laboratory. The UHV system is a central part of the experiment system, not only acting as an atom source and allowing high trapping times but also being the keystone around which the rest of the experiment is constructed.

The chapter will continue with an overview of the system in Section 4.2. Section 4.3 will follow with the design of the key chambers of the system, the 2D and 3D MOT chambers and the science chamber. Section 4.4 covers the development and assessment of the epoxy sealing technique for bonding viewports directly onto metal chambers. The design for the layout of the system, alongside calculation and design of the pumping system is then given in Section 4.5. The mounting and alignment of the system are described in Section 4.6. Section 4.7 will discuss the performance history of the system, including discussion of the effectiveness of the system. Finally, the outlook will be presented in Section 4.8, alongside the current status of the system.

4.2 Overview of the vacuum system

Figure 4.1 shows an overview of the UHV system and Figure 4.2 shows a photograph of the system before baking. Having separate chambers for magneto-optical trapping of each species is preferable due to the impact of interactions between rubidium and potassium, which reduce the achievable trapped atom number

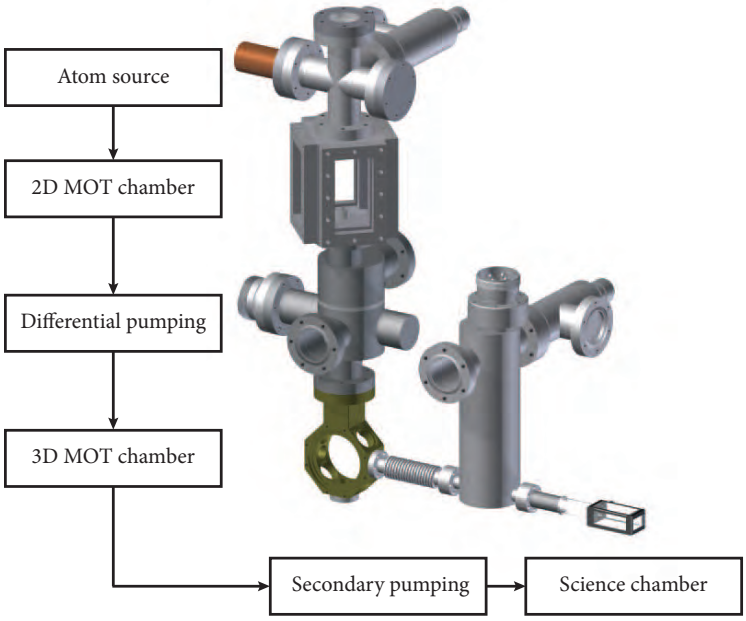

Figure 4.1: showing an overview of the vacuum system. Atoms are first trapped in the 2D MOT chamber, with pressures expected to be of order 10^{-8}mbar. The atoms are pushed into the 3D MOT chamber using a detuned laser beam. The pressure required in this chamber is much lower, of order $10^{-10} - 10^{-11}$mbar. To limit background gas flow between the two chambers a differential pumping stage is used. Atom clouds from the 3D MOT are moved through an additional pumping stage and into the science chamber using magnetic transport. Additional species will be added by including an extra 2D-3D MOT set up. For scale, the distance between the 3D MOT chamber and the glass cell centres is approximately 350mm.

for both species [52]. Rather than using the 3D MOT chamber for the final stages of the experiment, a separate glass cell is used. This is to allow the specific glass thickness and working distance required by the microscope objectives of the high resolution imaging scheme. Optical access is also greatly improved for the dipole trapping scheme. As such, the system has a modular design with separate sections for trapping each atomic species and another for the final experiment stages.

The most obvious constraint on the system is permitting long enough lifetimes by reaching a low enough pressure. The e^{-1} lifetime of a sample of atoms decaying only due to collisions with a background gas of pressure P is of the order $\left(10^{-9}\text{s/P[mbar]}\right)$ [60]. The longest time scale stages of the experiment are loading of the 3D MOT and evaporation, each taking of order 20-30s and thus requiring pressures of order $10^{-10} - 10^{-11}$mbar in the relevant chambers and along the magnetic transport path.

Achieving a high atom loading rate typically requires a high background pressure of atoms. To avoid this limiting experiment lifetimes the system is designed to first trap atoms from a high background gas

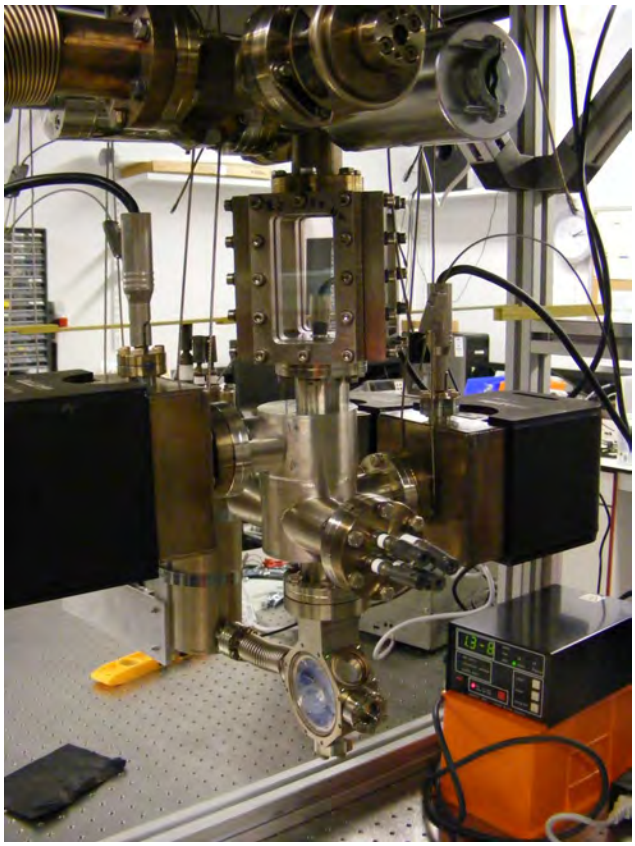

Figure 4.2: showing the UHV system prior to baking. The science chamber is obscured by a shield.

and then transfer them to a region of low background pressure before trapping and cooling them further. This is accomplished through use of a 2D-3D MOT setup where a large amount of atoms are first cooled in two dimensions in a 2D MOT. These atoms are then transported to the 3D MOT chamber by pushing them with a detuned laser beam. The 3D MOT is loaded using the resulting high atom flux beam, while having a lifetime orders of magnitude longer than what would achievable in the 2D MOT chamber. To limit transmission of background gas between the two regions of the system they are linked only by a differentially pumped stage.

The UHV system accommodates the requirement of the magnetic transport system to have a narrow spacing between the trapping coils. Specifically, the system has an exceptionally narrow profile along the transport direction, with the 3D MOT chamber having a thickness of just 36mm. This was achieved through development of an epoxy sealing technique in which windows are bonded directly onto a metal chamber. In order that the coils can be placed in close proximity to the vacuum system, a novel mounting technique has been used. The 2D-3D and science section are separated by a flexible UHV bellow and the system is hung

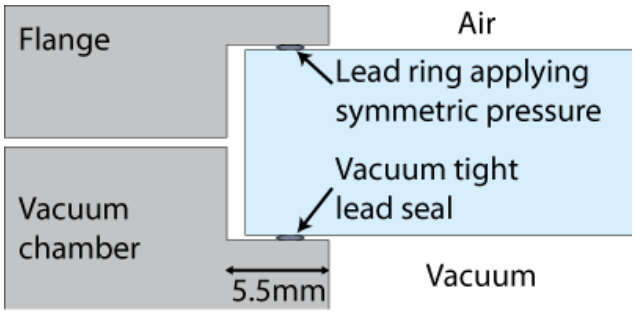

Figure 4.3: showing the sealing geometry when using the lead sealing technique of [77]. The image is to scale with the 2D MOT design except the lead which is exaggerated for emphasis. The window is placed onto a loop of lead pre-flattened to 0.2mm thickness. Another such loop is placed between the window and a tightening flange. The flange is then tightened against the chamber body, applying pressure onto the window and lead seal through the upper lead loop. The result is a vacuum tight seal between the window and chamber, formed by the lower lead loop.

on wire ropes. The alignment is then fixed using clamps to define the horizontal position. This allows good alignment between the separate sections. Finally, to reduce the presence of stray fields along the transport direction the system has been constructed of low magnetic materials, primarily stainless steel 316L and 316LN, and uses only A4 bolts.

4.3 Key chambers of the vacuum system

The UHV system is comprised of three main chambers, each of which grant external optical access to the atoms. The first is the 2D MOT chamber, which acts as a source for the atoms, having atom dispensers and optical access for creating a 2D MOT. The 3D MOT chamber allows access for beams which capture the atom flux from the 2D MOT and provide cooling in all three dimensions. The final chamber is the science chamber, consisting of a non-standard glass cell in which the final stages of the experiment are performed. The first two of these chambers were produced in house, with the glass cell being purchased from an external company, Japan Cell.

4.3.1 Lead sealed 2D MOT chamber

The 2D MOT chamber mounts directly onto the top of the differential pumping stage of Section 4.5.4. The chamber has a CF35 flange connection with just a narrow clear bore, through which the low conductance tube enters. A 2D MOT requires access for four beams. Typically large beams are preferable in order to provide a larger capture volume. To allow good optical access without having an excessively large chamber

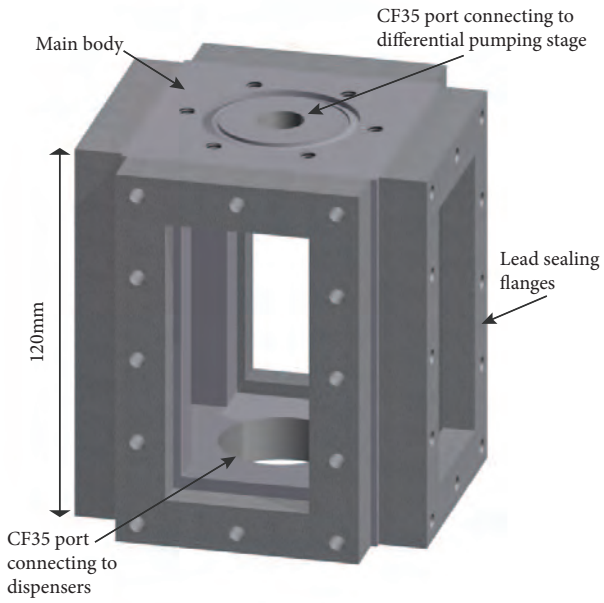

Figure 4.4: showing a CAD drawing of the 2D MOT chamber, the overall height is 120mm.

a specialised sealing technique was employed, in which rectangular windows are mounted directly to the chamber by pressing them against a lead gasket which forms the vacuum seal [77]. A cross-section of the geometry used is shown in Figure 4.3. The lead ring is prepared by dry welding, using a clean soldering iron, lead wire onto itself to form a continuous loop. The window is first placed onto the lead ring, preflattened to approximately 0.2mm thickness. Another ring is placed on top of the window and then onto this is placed a flange. The bolts are then tightened using 0.2Nm steps in an alternating criss-cross pattern up to 1.8Nm, allowing the pressure to remain even during the tightening process. Belleville washers are used to ensure pressure is maintained and to reduce pressure variation during baking. The chamber was designed to accommodate elliptical beams of dimensions up to approximately 80mm by 20mm, using windows 100mm by 55mm. A CAD design of the chamber is shown in 4.4, with the chamber and flanges being constructed from stainless steel 320.

The 2D MOT chamber has an atom source and access for a pushing beam to transfer atoms from the 2D to 3D trap. This was achieved by having a CF35 flange on the opposite end to the differential pumping stage. This is connected to a standard vacuum cross, with a valve for pumping down, viewport for the pushing beam and electrical feedthrough for the atom dispensers. Three dispensers are mounted as shown in Figure 4.5. When inserted into the system they were directed such that atoms are dispensed into the 2D MOT chamber. The dispensers used are two containing alloys of rubidium and one of potassium.

Figure 4.5: showing the mounting of three dispensers onto an electrical feedthrough using vacuum compatible barrel connectors. Connection to the common ground is made through a copper sheet which also holds the dispensers in a well-defined direction. The mounted dispensers are one of potassium mounted centrally and two of rubidium at either side. The feedthrough is mounted into a CF35 flange having diameter 70mm.

4.3.2 Epoxy sealed 3D MOT chamber

The 3D MOT chamber is connected to and pumped through the lower flange of the differential pumping stage. Optical access is required for three orthogonal beam pairs, detection such as absorption imaging or fluorescence measurement and an exit port for the pushing beam. A passage through which atoms can be moved to the science chamber is also required. The natural approach is to use an extruded octagonal chamber. Five radial windows allow access for two beam pairs and an exit port for the pushing beam, while two large windows in the axial direction give excellent optical access for the final beam pair and any imaging beams. This leaves three empty faces, two of which are used to allow passage of atoms to the science chamber and the other, opposite the pushing beam exit port, to connect to the differential pumping stage.

As discussed in Section 3.6, the magnetic transport system required the use of a thin vacuum chamber to allow more compact transport and 3D MOT coils, so as to provide larger gradients for smaller currents. Commercially available chambers which grant the necessary optical access are too large to meet this requirement. These are limited by the thickness of the ConFlat flanges used to mount viewports and peripherals. Thus, to produce a narrower chamber a custom sealing technique is required, the development of which is

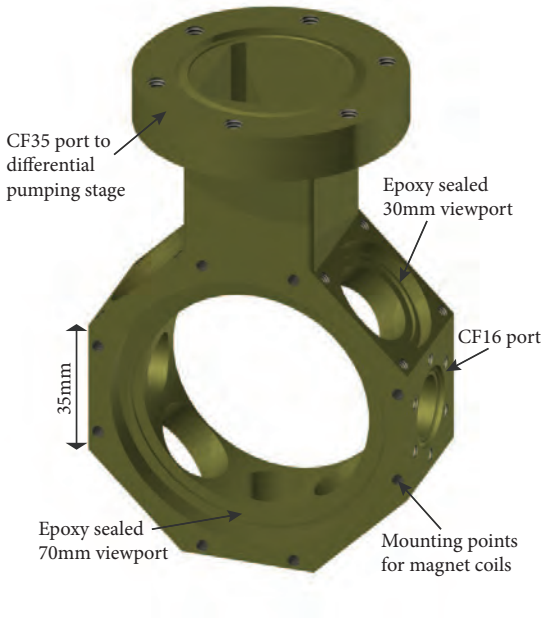

Figure 4.6: showing the CAD drawing of the 3D MOT chamber. The thickness of the chamber below the flange is 36mm, with an overall height of 129mm.

given in Section 4.4. Using this technique a chamber was prepared having a design as shown in Figure 4.6. The axial thickness of the chamber is just 36mm.

4.3.3 Science Cell

The science chamber houses the final stages of the experiment. The chamber is designed to account for the required glass thickness and working distance of the microscope objectives, 3.5mm and 13.89mm respectively. Good optical access is also required for the optical dipole trapping scheme. To achieve this a custom vacuum cell was developed around use of a glass cell. A typical problem with glass cells is that, due to the high temperatures involved in manufacture, the window surfaces can only be anti-reflection coated after production, leaving the internal faces uncoated. Typically, as the bonds between surfaces are also glass, a large amount of light is scattered around the cell within the glass. Both of these issues would reduce the achievable contrast using the imaging scheme. To overcome these problems a glass cell, shown in Figure 4.7, was purchased from an external company, Japan Cell, which uses epoxy to form the window bonds of cells. This technique does not require high temperatures, allowing coatings to be placed on the window faces before construction. By surrounding each window with a black quartz frame light is prevented from bouncing between the windows. The cell is linked to a CF16 flange using a glass-to-metal transition, resulting in a long and narrow connec-

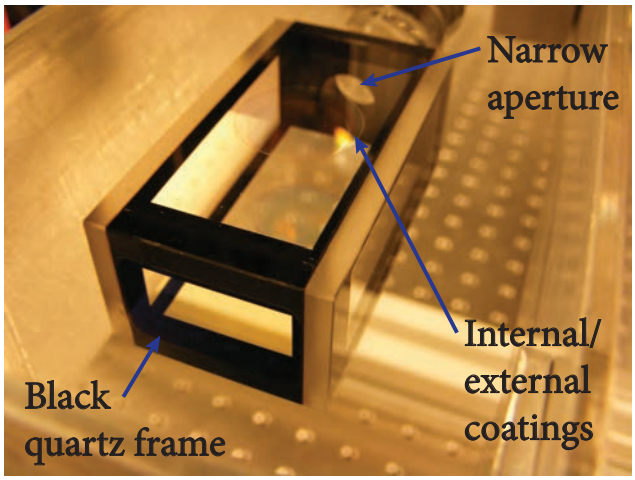

Figure 4.7: showing a photograph of the glass cell as mounted on the UHV system. The outer dimensions of the cell are 33x23x60mm.

tion, 90mm by 16mm diameter and with a narrower aperture of 5mm by 8mm diameter, to the rest of the vacuum system. This limits the effectiveness of any vacuum pump attached to it.

4.4 Epoxy sealing of viewports

Standard UHV viewports are generally constructed by brazing the optical element onto a thin metal sleeve of, for example, Kovar which is then brazed onto a CF flange. The result is far larger, in both radius and thickness, than the optical element itself. This configuration also results in a large amount of stress on the viewport element.

Several techniques have been developed to improve upon the size of standard viewports. These involve taking a window and sealing it directly against the chamber. One technique is to place an indium ring between a window and the chamber, then to use this as a soft gasket. For example see [78] in which the indium is used to seal against a copper gasket rather than using a knife edge. Unlike the similar lead sealing approach of the 2D MOT, the clamp used to squash the window onto the indium can be removed afterwards with the seal remaining leak tight, therefore having a much smaller final profile. The resulting bond can be leak tight to acceptable UHV levels while also remaining small. However, due to the low melting point of indium, 156°C, an indium sealed chamber can only be baked to around 120°C, which is a low baking temperature. Another approach would be to use a helicoflex gasket, a body containing a helical spring, to form the seal. These can be used between two flat surfaces and, with appropriate choice of materials, can be baked to over 250°C. However, unlike indium seals, the clamps providing the sealing pressure must remain

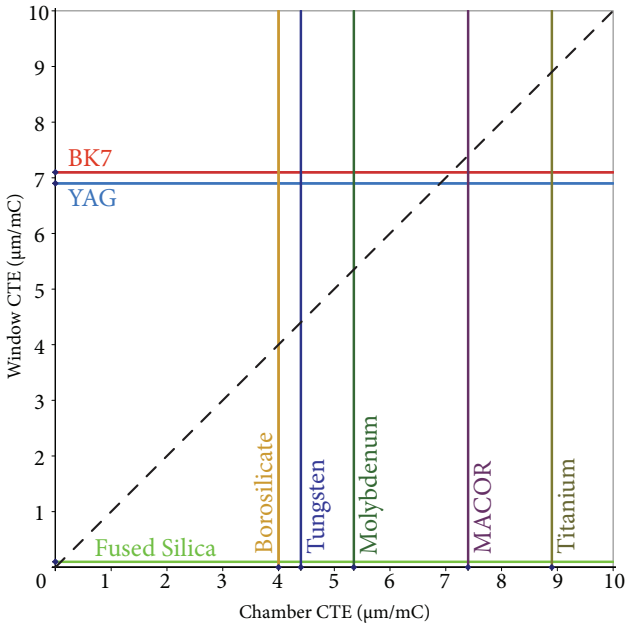

Figure 4.8: showing coefficient of thermal expansion of various window vs frame materials [79, 80].

in place. This would make the chamber considerably thicker than with indium seals.

The challenge is to provide a seal which does not need continuous external pressure and also can be baked to high temperatures. An ideal candidate is to use an adhesive to bond the window surface to the chamber directly. However, bonding two surfaces of different coefficients of thermal expansion (CTE) can put large stress onto the bond even over small changes in temperature, giving the potential of breaking or forming micro-leaks in the bond during baking. To reduce the thermal stress during baking, appropriate materials can be chosen which have similar CTEs. Another issue is the choice of an appropriate adhesive. The most important criteria set on the adhesive are the outgassing rate of the glue, and a degradation temperature high enough to permit good baking temperatures.

4.4.1 Material choices

The first step in producing an effective design is the correct choice of window and frame materials. By choosing two materials with similar CTE the amount of thermally induced stress can be reduced. The CTE for various practical materials are compared in Figure 4.8. Some materials can be ruled out based on their CTE alone. For example, the CTE of fused silica is far below that of the suggested frame materials ruling this out as a window material. This leaves the choice of BK7 or YAG for the windows and based on the CTE of these possible frame materials are molybdenum, titanium and MACOR. However, both molybdenum

and MACOR are unsuitable for use as a CF flange due to the pressure exerted onto the knife edge when pushed into the copper gasket. As the piece should be usable with standard UHV fittings titanium is the most practical choice.

As critical is the choice of adhesive which should be vacuum compatible and have a suitable operating temperature. The adhesive chosen was a two component epoxy, Epo-Tek 353ND, which is recommended by NASA as having a low outgassing rate [81] and has a specified continuous operating temperature of up to 250°C. This epoxy has also been used in several recent UHV applications, for example, in the lead sealing technique of [82] it is used as a back-up sealant and in [83] it is used to bond an atom chip to a glass cell and provide a UHV seal. It also has a low viscosity which allows for production of very continuous, uniform bonds. The epoxy has a CTE $54 \cdot 10^{-6}\mathrm{K}^{-1}$ rising to $206 \cdot 10^{-6}\mathrm{K}^{-1}$ above the glass transition at 120°C. Despite the epoxy being rated as having a low outgassing rate, it will exceed that of the frame material and as such, it is necessary to minimise the amount of epoxy exposed to the vacuum. Voids in the glue must be avoided as these would lead to weakly connected pockets of gas at higher pressure, resulting in virtual leaks.

A range of different curing schedules are available to the epoxy, for example 80°C for 30 minutes or 150°C for 1 minute. The curing temperature has influence over two key parameters, the zero stress temperature, which is where the epoxy cures and the bond activates, and the glass transition temperature, T_g, of the epoxy [84]. When heated to temperatures above T_g the CTE of the epoxy is much larger, and increases rapidly with further heating. More importantly, above T_g the strength of both the epoxy and its adherence to a surface is reduced considerably, decreasing further with temperature. Using a higher temperature cure, and curing for longer increases T_g, allowing a larger temperature range over which both the bond and the epoxy remain strong [84]. For this reason the epoxy is cured at 150°C for an hour, and then allowed to cool to room temperature slowly over several hours. This sets the zero stress temperature at close to 150°C, in practice the epoxy may cure before it can heat to this temperature, and T_g to as high as possible which for 353ND is in the range 125°C to 130°C. This places the seal under the greatest stress at room temperature, and upon heating the stress is reduced. When heated and in the region of T_g the stress approaches the zero stress point. In this way, the thermal stress is lower as the bond strength decreases.

4.4.2 Test system

In order to test the viability of the sealing technique a test UHV system was constructed, as shown in Figure 4.9. This consisted of three sub-systems isolated by all metal valves, each containing a titanium sublimation pump (TSP), 3-filament cartridge from GammaVacuum, an ion getter pump (IGP), 20l/s TiTan differential

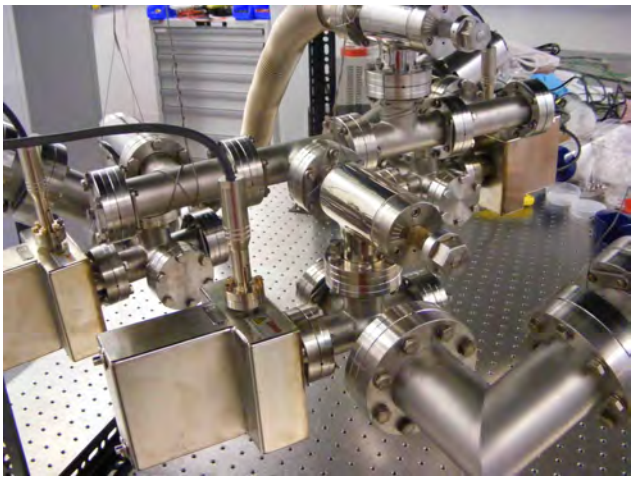

Figure 4.9: showing the UHV system used to test the viability of the epoxy sealing technique. The system comprises three test chambers separated by valves. Each chamber contains an ion getter pump, a titanium sublimation pump, access for a test piece and a blind flange which can be replaced with a gauge for closer testing. The main body of the system contains a cold cathode gauge specified to measure pressure down to $5 \cdot 10^{-11}$mbar.

diode from GammaVacuum, and space for including a test piece on a CF35 flange. The main body of the system contains a cold cathode gauge, IKR270 from Pfeiffer, specified to measure pressure down to $5 \cdot 10^{-11}$mbar. However, this was more weakly connected to the individual test pieces and placed in a region having weaker pumping. The system was pre-baked to 350°C for one week with blind flanges taking the place of test pieces. Sub-system pressures were measured using the IGP, which is only indicative of the true pressure. In particular, later testing on a different system has shown IGP pressures to be up to a factor of 40 different from that measured with atom clouds. The test sub-systems reached a pressure of $5.1 \cdot 10^{-12}$mbar after prebaking, well below the accuracy limit of the IGP.

4.4.3 Tests using a wide bond

Testing of the epoxy seal is necessary due to both the undefined strength of the adhesive and the lack of quantitative outgassing data. Initial tests were carried out using a geometry which minimised the amount of epoxy exposed to the vacuum in order to reduce outgassing and film production. To achieve this a test frame was manufactured for use with a 25.4mm diameter by 3mm thick BK7 test window. The geometry of the epoxy bond is shown in Figure 4.10. The frame consisted of a tube with outer diameter 27.4mm and central bore of 23.4mm. The window was then placed into a 2mm deep pocket, diameter 25.6mm such that it was surrounded by a 1mm thick wall. The other end of the tube was connected to a CF35 flange, with the frame and flange being constructed from one piece of titanium.

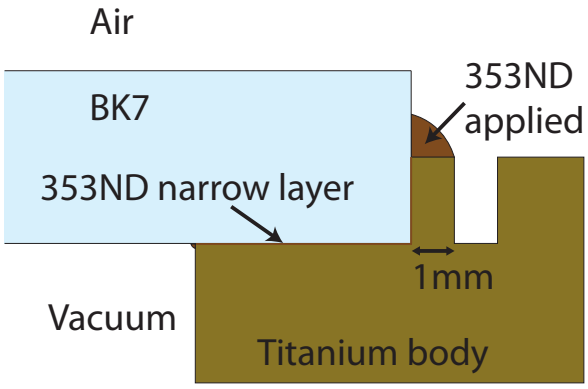

Figure 4.10: showing the initial geometry for epoxy bonding BK7 windows onto a titanium chamber. The window is first placed into a pocket on the frame. Epoxy is then placed onto the top of the pocket, against the window edge. The epoxy is pulled by capillary action through the narrow 0.1mm gap between the window circumference and titanium frame, leaving a thin bond layer with very little exposure to the UHV system.

To ensure a strong bond it is necessary that the bonding surfaces are exceptionally clean before gluing. Of particular importance is removal of water on the surface of the bond. After removing bulk greases, the titanium bodies of the test pieces were processed according to the cleaning cycle:

1. Ultra-sonic bath of Acetone for fifteen minutes
2. Ultra-sonic bath of Liquinox, diluted 1:40 with distilled water, for fifteen minutes
3. Ultra-sonic bath of Propanol for fifteen minutes

Directly before gluing each window the bonding surfaces were again cleaned with high grade propanol to remove built up surface water.

The epoxy is prepared by mixing the two components to the correct ratio and then thoroughly degassing the mixture to reduce the presence of air bubbles. This is achieved by placing the epoxy under vacuum and allowing gas to escape. This was aided by putting the epoxy onto a platform heated to approximately 70°C while under vacuum, both speeding the degassing process and allowing the removal of all visible bubbles. Without any heating many bubbles persist indefinitely.

To seal the window onto the frame, the window is placed into the pocket and epoxy applied to the top of the titanium pocket and side of the window. This allows the epoxy to be pulled by capillary action through the small gap between the titanium and window and underneath forming a narrow layer. While heating up to curing temperature, the viscosity of the epoxy lowers, allowing it to flow more easily under the window and over the whole rim resulting in a continuous and thin seal between the window and the titanium it rests on. The epoxy thickness in this region was measured as 10-20μm using a micrometre.

Figure 4.11: *Left:* showing one of the large windows after curing, the thin epoxy bond layer can be seen as a brown ring. *Right:* showing the appearance of fringes after attaching the assembled chamber to the test UHV system and performing two heating cycles to a baking temperature of 200°C. Further heating cycles lead to more widespread fringes.

Three test pieces were produced using this design and attached to the test vacuum system. After attaching the test pieces, the sub-system pressure reached $6.7 \cdot 10^{-11}$mbar before baking and $9 \cdot 10^{-12}$mbar, as measured on the IGP, after a three day bake at 200°C. The pressure of the system main body was $1 \cdot 10^{-10}$mbar as measured on the gauge with the valves open. As these results were promising, further testing was performed using an assembled 3D MOT chamber consisting of six windows of two sizes, 30mm diameter for the smaller side windows and 70mm diameter for the larger face windows. The glue bond of the final large window directly after cooling down from curing temperature is shown in Figure 4.11L. Connecting the chamber to the system revealed that after multiple heating cycles the thin layer of epoxy started to lose bonding to either the window or titanium surfaces. This could be seen by interference fringes, as one might observe on thin films, appearing in patches over the bonding area as shown in Figure 4.11R. These moved under gentle pressure applied to the region by hand, and became more widespread with further temperature cycling. This suggested that simply matching thermal expansion coefficients is not enough to produce a seal which is repeatedly bake-able.

4.4.4 Revised techniques

In order to improve upon the previous design the shear stress, induced by thermal stress, placed on the epoxy had to be minimised and the bond strength increased. The shear stress on the epoxy can be compensated for by increasing the thickness of epoxy, allowing the bulk epoxy to deform rather than the bond [85]. The

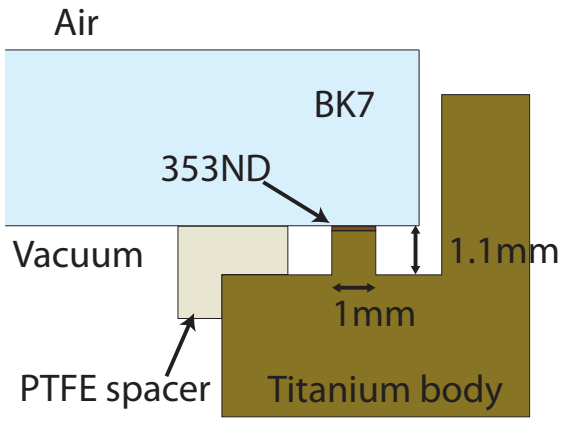

Figure 4.12: showing the revised bonding geometry. The epoxy is now held in an aspect ratio of 1:10, height:width. This allows the epoxy to better cope with the shear stress caused by thermal stress. The width of the epoxy is fixed by the width of the titanium extrusion onto which the glue is applied. The height is fixed to 0.1mm using the PTFE spacer, which has a thickness of 1.1mm in the region between the chamber and the window. The surfaces to which the epoxy bonds are sand blasted to provide a rough and easy to wet surface. Good wetting is one of the key factors in gaining a strong bond.

most effective ways to increase bond strength with adhesives is to roughen the surface to which the bond adheres [86]. An effective approach which does not result in contamination of the surface is to sand blast the bonding regions of both the window and titanium frame. A caveat to this is that sandblasting does not result in as uniform a surface over larger scales as machining or window polishing making the sandblasted surface useless for setting any defined distance. Additionally, the sandblasting process exposes the windows to machining greases present in the sand blasting beam line. The windows were sand blasted on one optical face such that the outer 2mm of their radius was roughened. The remaining inner 13mm radius was protected using a mask to prevent exposure to both sand and greases. After sand blasting, the windows were subjected to the cleaning cycle of Section 4.4.3.

To maintain a reproducible application technique the frame geometry was changed to that presented in Figure 4.12. Now epoxy is to be placed onto a protruding rim of thickness and height 1mm. Epoxy is applied using a needle tip onto the top of the rim only. The epoxy is then spread carefully until it is roughly the correct height and reasonably evenly distributed. To prevent epoxy falling down the internal side of the rim, it is forced over the external side at several points, giving it a preferred flow to the non-vacuum side of the bond. The window is then lowered onto a set of spacers, shown in Figure 4.13L, which rest on the flat portion of frame toward the inside. These hold the window 0.1mm above the protruding rim, setting the epoxy height with excess epoxy bulging onto the rim and window. As the spacers rest on unroughened surfaces of both the

Figure 4.13: *Left:* showing the spacers used in the gluing process. The internal spacers rest on the radius of the clear bore of the window. These set the height of the epoxy layer by having a well-defined thickness and serving as the resting point for the window during curing. The spacers are put into place after the epoxy has been applied and removed after curing. They are constructed from PTFE to prevent epoxy from bonding to them should they come into contact with it through undesirable flow. *Right:* the centring tool has three arms which fit between the window and the titanium chamber to centre the window. The window is held in the centring tool and lowered onto the internal spacers, to ensure that the window is never off centre, avoiding epoxy adhering to unnecessary surfaces. This is constructed of nylon to provide some elastic strength for holding the window in the tool. The centring tool remains in place until after curing.

frame and window, the window is fixed in a well-defined position with regard to the frame. The window is centred using spacers between the external diameter and the frame as shown in Figure 4.13R. Before curing the window is gently turned back and forth while the epoxy region is visually inspected for voids. Voids can generally be removed by carefully varying the turning speed to spread the epoxy.

A prototype was produced using this design, with a 70mm diameter, 5mm thick window and an inner radius of 66mm for the epoxy. This was baked three times at increasing temperature, 150°C, 175°C and 200°C each time spending one day at temperature. The system was allowed to cool to and remain at room temperature overnight between baking cycles. After the 150°C bake the measured pressures was $3{\cdot}10^{-11}$mbar, while after the 200°C bake the pressure had dropped to $3 \cdot 10^{-12}$mbar showing that this sealing technique could now be used for repeated bakes. Another identical prototype was prepared in order to test repeatability of producing the seal. This and the original prototype were both attached to separate arms of the UHV test system and baked to 200°C for five days at temperature. The system pressure in the region of the original prototype reached $1 \cdot 10^{-11}$mbar while the new piece reached $1 \cdot 10^{-10}$mbar with the latter dropping to $8 \cdot 10^{-12}$mbar after firing of the TSP. The gauge displayed a pressure of $9 \cdot 10^{-11}$mbar with valves open. The pressure stayed at these values for one week, whereupon the pieces were removed from the system and subjected to a further eight temperature cycles to 200°C. Upon visual inspection no difference was noticed

to the bonding surfaces or epoxy aside from the expected darkening due to further curing.

Due to the promising results of these tests a 3D MOT chamber was constructed using the revised bonding geometry. This required gluing four 30mm diameter and two 70mm diameter windows onto the titanium frame as shown previously in Figure 4.6. Due to the geometry of the part, each window was glued and cured individually meaning that the first window glued was cycled to temperature five times during the curing of the remaining windows. The small windows were glued first to allow optimal access for removing the internal spacers. When gluing the final large window, the internal spacers had to be removed using a long dentist pick to reach through the CF16 flanges.

However, despite promising results in testing, once the constructed chamber was placed on the UHV system and baked it was later found to cause a long time scale rise in pressure, as is discussed later in Section 4.7. The magnitude of this was masked by pressure measurement using the IGPs being highly non-linear and inaccurate, as determined by atom cloud measurements. The results of this section should therefore be taken with some scepticism, although the IGP measurements are supported to some degree by the gauge and the lack of a rise in pressure.

4.5 Design of the vacuum system

This section will cover the design of the pumping system and differential pumping stages used to limit gas flow around the system. This will first involve developing formulae for calculating pressure and gas loads. These are then applied to provide a suitable predicted pressure.

4.5.1 Pressure calculation

To calculate achievable pressures in a vacuum system one must understand both how pressure relates to gas load and how gas moves around the system. The pressure, P, achievable in a chamber of the vacuum system is given by the ratio of gas load, Q, to pumping speed, S [87]:

$$P = \frac{Q}{S} \tag{4.1}$$

In a UHV system, unavoidable relevant gas loads are outgassing from internal surfaces of the system, diffusion through the system walls and experiment processes. To achieve low pressures all of these sources should be minimised as far as possible. In the experiment there is an unavoidable large process load due to the atom dispensers. The first region of the experiment with long time scales, thus requiring low pressures, is the 3D

MOT chamber. Therefore a particular aim in the design of the UHV system is to reduce this process load in the region of the 3D MOT such that it is on a similar scale, or lower, when compared with the outgassing and diffusion contributions to the gas load. Once at this level, a pumping system sufficient to reach acceptable pressures will be implemented. In this section the relevant formulae and understanding will be developed.

Outgassing can be managed by using materials with sufficiently small rates and ensuring good working practices to avoid contamination. Outgassing can be improved dramatically by baking; heating the vacuum system to increase the rate of desorption from the internal surfaces and the wall interiors. On cooling, the out-gassing rate of most materials is reduced by orders of magnitude. The magnitude of the reduction depends on baking temperature and duration, which is typically at least 150-250°C for several days to a couple of weeks. Diffusion through the system walls is generally small compared to out-gassing rates, but can become relevant for hydrogen through stainless steel or helium through glass windows.

The first step in design of the system is therefore to minimise the impact of process load on the pressure in the 3D MOT chamber. The throughput, Q, resulting from a pressure difference, $\Delta P = P_{high} - P_{low}$ is given by:

$$Q = c\Delta P \tag{4.2}$$

where c is the conductance between the two pressure regions. As is clear from (4.2) reducing the conductance results in a smaller throughput of gas between the two chambers. For a tube of length L and radius R, c is given by [88, 89]

$$c = \left[1 + \frac{3L}{8R}\right]^{-1} \cdot \frac{\pi}{4} v R^2 \tag{4.3}$$

with v the average speed of gas inside the system; this has the effect of reducing the conductance for heavier molecules, the average value for air is $v = 464\text{ms}^{-1}$. The narrower the tube between the two chambers the higher the achievable pressure difference. For multiple non-trivial connections in series the effective conductance is given by

$$\frac{1}{c_{total}} = \frac{1}{c_1} + \frac{1}{c_2} + \frac{1}{c_3} + ... \tag{4.4}$$

or for just two connections

$$c_{total} = \frac{c_1 c_2}{c_1 + c_2} \tag{4.5}$$

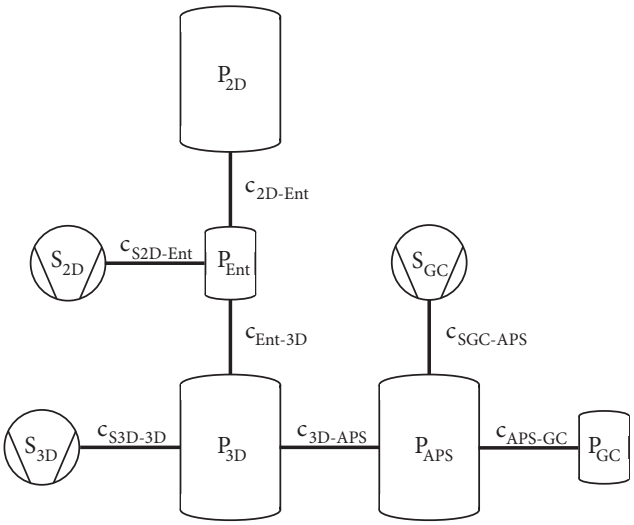

Figure 4.14: showing the layout of the system as a series of pumps and volumes interlinked by conductances. The pressure in volume A is represented by P_A, while c_{A-B} denotes the conductance between volumes A and B. S_A represents an ion getter pump which has effective pumping speed $S^*_{A,B}$ at volume B. The system also contains two titanium sublimation pumps, one placed with S_{3D} and the other placed directly inside the APS volume.

showing that the total conductance is limited by the smallest conductance, typically caused by the smallest aperture.

As the conductance controls flow around the system it also limits the effectiveness of a pump at removing particles from a connected region. A pump connected to a chamber through a region of high conductance is more effective as the pump experiences more molecules per unit time from the chamber. The conductance results in an effective pumping speed, S^*, according to

$$S^* = \frac{S \cdot c}{S + c} \tag{4.6}$$

For clarity, the notation used will be of the form $S^*_{A,B}$ with B denoting the point at which the effective speed of pump S_A is measured.

To provide a framework of equations describing the system it is useful to divide it up schematically, into components as shown in Figure 4.14. The key components of the system are the 2D and 3D MOT chambers, the science chamber, the pumps and the connecting tubing. As illustrated in Figure 4.14, the 2D and 3D MOT chambers are separated by a conductance then a pump followed by another conductance. This is to achieve differential pumping between the two chambers, further lowering the throughput between them.

To calculate the magnitude of the gas load between the 2D and 3D MOT chambers it is first necessary

to find the gas load between the 2D MOT and the differential pumping centre. Taking the pressure in the 2D MOT chamber, P_{2D}, as a constant, and assuming that the gas load from the 2D MOT is the dominant load, the pressure at point P_{Ent} is given by:

$$P_{Ent} = \frac{Q_{2D-Ent}}{S^*_{2D,Ent}} = \frac{c_{2D-Ent} P_{2D}}{c_{2D-Ent} + S^*_{2D,Ent}} \tag{4.7}$$

The gas load between the 2D and 3D MOT chambers is then given by

$$Q_{2D-3D} = c_{Ent-3D} \left(P_{Ent} - P_{3D} \right) \tag{4.8}$$

and from (4.1) the pressure in the 3D MOT chamber, P_{3D}, is given by

$$P_{3D} = \frac{Q_{2D-3D} + Q_{outgas} + Q_{leaks}}{S^*_{3D,3D}} \tag{4.9}$$

4.5.2 Calculation of differential pumping parameters

As described in the preceding section, the purpose of the differential pumping stage (DPS) is to reduce the gas load Q_{2D-3D} such that it is negligible compared to outgassing. From (4.8) it can be seen that this is possible through reduction of c_{Ent-3D} and P_{Ent}, which is in turn reducible through c_{2D-Ent} and $S^*_{2D,Ent}$.

The pump S_{2D} in Figure 4.14 is an IGP with nominal pumping speed $S_{2D} = 20$l/s, providing pumping for the 2D MOT. Larger sizes are impractical due to the need of the system to stay compact. As the system must remain compact, the largest flange size practical for the DPS is CF35, meaning tubing of diameter 38.1mm. Using the shortest practical link for the tube having conductance $c_{S2D-Ent}$ then gives a conductance of 23.8l/s. This gives an effective pumping speed at the entrance of $S^*_{2D,Ent} = 10.9$l/s. As the DPS should be kept short in length, the most substantial reduction in the conductance of c_{2D-Ent} is achieved through use of a small radius. However, too small a radius would infringe upon transferring atoms from the 2D to the 3D MOT. The pushing beam has a beam diameter of 3mm. Using a tube with a diameter of twice this allows for significant alteration of the pushing beam alignment without vignetting. The longest practical length is achieved through allowing the tube to penetrate into the 2D MOT chamber, allowing a tube length of 86mm. This results in a conductance of $c_{2D-Ent} = 0.28$l/s. Using (4.7) and assuming a 2D MOT pressure of $P_{2D} = 10^{-8}$mbar then gives a pressure at the middle point of the DPS of $P_{Ent} = 2.5 \cdot 10^{-10}$mbar.

All that remains is to choose appropriate dimensions for the lower conductance tube c_{Ent-3D}. For ease of manufacture, allowing the tube to be constructed from one piece, the radius is kept the same. A length

of 69mm allows the tube to pass near to the entrance of the 3D MOT chamber. This gives a conductance of $c_{Ent-3D} = 0.34$l/s for the lower tube. Using (4.8) and assuming $P_{Ent} >> P_{3D}$, which is identical to calculating the maximum particle flow due to gas flow from the DPS, the gas load from the 2D to the 3D MOT is then $Q_{2D-3D} = 8.75 \cdot 10^{-11}$mbar·l/s. This is near negligible when compared to the outgassing rates presented in the following section.

4.5.3 Calculation of expected pressure in the 3D MOT chamber

The 3D MOT will primarily be pumped by another IGP, $S_{3D} = 20$l/s, and a TSP which will not be considered for initial estimates. The 3D MOT is linked to S_{3D} in a similar fashion as S_{2D} to the 2D chamber but with a longer tube, giving a conductance of $c_{S3D-3D} = 17.5$l/s and effective pumping speed $S^*_{3D,3D} = 9.3\text{l/s} \approx 0.47 S_{3D}$.

All that remains is to estimate the remaining source terms Q_{outgas} and Q_{leaks}. Leaks will always be present at some level, but through careful construction they will be dominated by the gas load due to outgassing of surfaces. Q_{outgas} can be estimated by taking approximate values of the surface areas for the different components of the 3D chamber. Using the CAD design of Figure 4.6 gives approximate areas of 48.9cm^2 of titanium, 95.8cm^2 of BK7 and 402cm^2 for stainless steel 316LN. Typical post-baking outgassing rates for these are $7 \cdot 10^{-12}$mbar·l/s cm^{-2}, $5 \cdot 10^{-12}$mbar·l/s cm^{-2} and $2.86 \cdot 10^{-13}$mbar·l/s cm^{-2} respectively [87, 90]. The resulting pressure in the 3D chamber is then

$$P_{3D} \approx \frac{\overbrace{8.75 \cdot 10^{-11}}^{Q_{2D-3D}} + \overbrace{9.8 \cdot 10^{-11}}^{O_{outgas-Ti}} + \overbrace{6.4 \cdot 10^{-10}}^{O_{outgas-BK7}} + \overbrace{1.1 \cdot 10^{-10}}^{O_{outgas-316LN}}}{\underbrace{9.3}_{S^*_{3D,3D}}} \approx 1 \cdot 10^{-10}\text{mbar} \tag{4.10}$$

This reveals that the pressure in the 3D chamber can be expected to be limited by outgassing from the BK7 windows of the chamber. However, the dominant gas loads from this source in this pressure regime are water and water constituents [88], all of which are very effectively pumped by a TSP. Achievable pumping speeds for H_2, and H_2O are 3l/s·cm^{-2} [91, 92]. The chamber housing the TSP, as described in Section 4.5.4, has a surface area 322cm^2 with line of sight to the TSP filaments. For half of this surface a nominal pumping speed of 485l/s would be possible for H_2 and H_2O with the titanium surface in the unsaturated state.

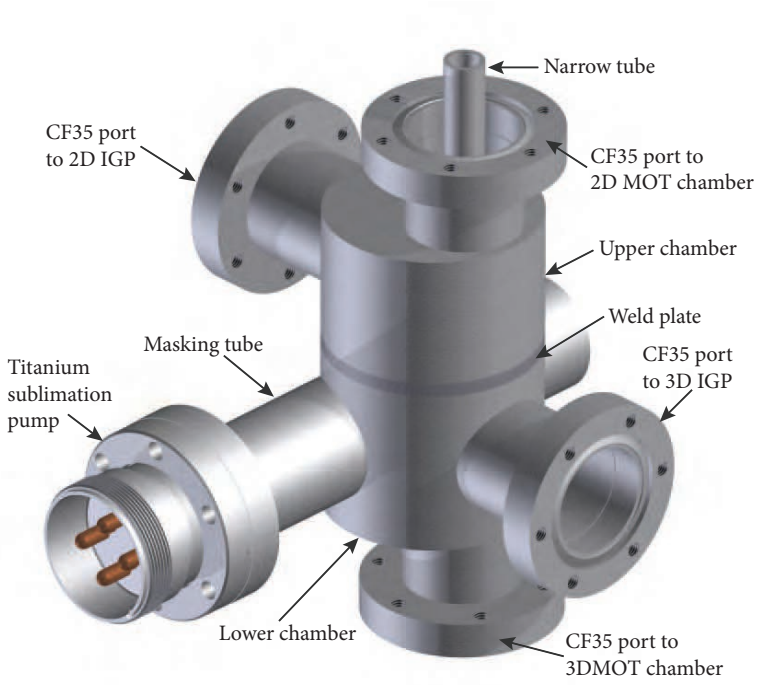

Figure 4.15: showing the design of the differential pumping stage separating the 2D and 3D MOT chambers. Overall height 188mm.

4.5.4 Design of the differential pumping stage

A custom manifold was designed to achieve the differential pumping scheme of Section 4.5.2 and provide the appropriate ports for the chambers and pumps. It was necessary to ensure that the manifold had a small footprint. If too large vertically the separation between the 2D MOT and 3D MOT chambers would become excessive, potentially leading to spreading of the beam of atoms being pushed from the 2D MOT. Along the magnetic transport direction of the experiment the manifold was kept narrow to allow close proximity between separate 3D MOT chambers, both to save on travel time during transport and prevent the need for an excessively long linear actuator.

The manifold, shown in Figure 4.15, is constructed of two stainless steel 316LN chambers separated by a plate through which a narrow tube passes. The narrow tube serves as both of the small conductance tubes, c_{2D-Ent} and c_{Ent-3D}. It is constructed from one continuous tube with a sculpted opening which coincides with the pump port of the upper chamber to form the differential pumping entrance. It has an inner diameter of 10.9mm to allow insertion of a graphite rod, inner diameter 6mm, through the internal bore. This is added to avoid rubidium or potassium entering the IGPs. The rod is held in place by inserting 1.5mm stainless steel wire through grooves in the narrow tube, as shown in Figure 4.16. The only conductance between the

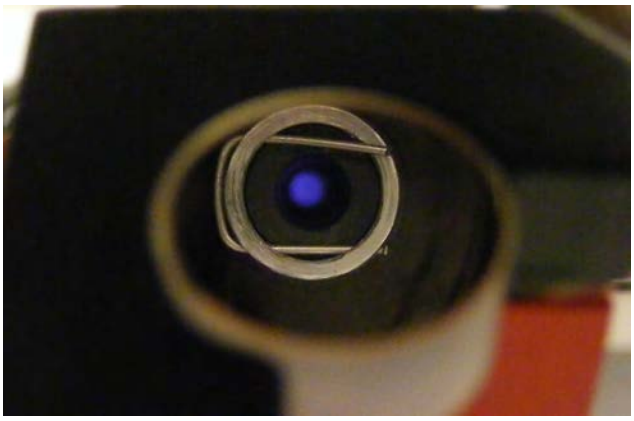

Figure 4.16: showing the fixing of the graphite rod in the narrow tube of the differential pumping stage.

two chambers is through the graphite rod.

The upper and lower chambers are both constructed from a 76.2mm outer diameter tube onto which standard 38.1mm inner diameter ports are welded. The upper chamber has two ports, the first connecting directly to the bottom of the 2D MOT chamber, with the 2D MOT chamber designed such that the narrow tube is inserted into a tight fitting hole, effectively reducing the conductance between the two chambers to that of the narrow tube. The second port, the radial flange, is used to connect the IGP labelled S_{2D}. The lower chamber has three ports, the first concentric with the top port of the upper chamber providing the connection to the 3D MOT chamber. The lower chamber IGP is located on the radial port opposite to that of the pump for the top chamber. The top and lower most ports, through which the narrow tube passes, are off centre with respect to the main body. The offsetting moves the narrow tube off-centre, allowing a TSP to penetrate through the lower chamber on the final port. This takes advantage of the large surface area inside the lower chamber, allowing a coating area of 322cm^2 whilst keeping the conductance between the TSP and the 3D MOT chamber high, both acting to drastically increase the effective pumping speed of the TSP. To prevent the TSP depositing onto unwanted surfaces, such as the interior of the IGP or the 3D MOT windows, it is inserted into a tube which penetrates through the lower chamber. This has a sculpted mask which protects the relevant solid angles. The use of rotatable flanges over the outer diameter of the large tube allows bolt access without requiring excessive space, saving extra centimetres. Using this design the total separation between the 2D and 3D MOT chamber flanges is 187.7mm.

Due to a manufacturing error the manifold arrived with the TSP tube bowed out from where it is welded onto the main body of the part. This required in house modifying of a TSP in order to allow insertion into the bent tube.

4.5.5 Additional pumping stage for the science chamber

To achieve the lowest possible pressure in the science chamber, an additional pumping stage has been implemented between this and the 3D MOT chamber, as shown in Figure 4.14. By having a narrow link between the two chambers this will act as another differential pumping stage and reduce the influence of any unknown gas loads in the 3D MOT chamber, for example outgassing from the epoxy sealant. The link is made using a CF16 bellow, $c_{3D-APS} = 3.7$l/s, for alignment purposes discussed in Section 4.6. This links onto a CF16 port of the additional pumping stage. This consists of a main body formed from a 63mm inner diameter tube, with four further ports. The first, directly opposite the CF16 bellow port, provides a CF16 port for the science chamber. Three CF35 ports are used to connect a valve, an IGP and a TSP. As with the TSP pumping the 3D MOT, the TSP has access to a large coating surface, 433cm^2, and is placed inside a tube which obscures line of sight between the TSP and the IGP. The IGP has excellent conductance, $c_{SGC-APS} = 73$l/s, to the main body, meaning an effective pumping speed of $S^*_{GC,APS} = 15.4$l/s while the TSP directly coats the interior surfaces. Neglecting any load from the 3D chamber, and using the previous outgassing rate for 316LN stainless steel gives a load of $1.2 \cdot 10^{-10}$mbar$\cdot$ l/s resulting in a pressure of $P_{APS} = 7.8 \cdot 10^{-12}$mbar without use of the TSP. However, the two entrance apertures of the science cell, 8mm radius and 90mm length followed by 5mm radius and 8mm length, create a small conductance to the science chamber of $c_{APS-GC} = 2.5$l/s. This has the consequence of limiting the effective pumping in the science chamber. Unfortunately, there is no freedom over this aperture due to the technology used in making the glass cell.

4.6 Mounting and alignment

The mounting of the system must ensure that there is optimal line of sight along the travel direction of the transport coils as well as that the coils can pass by unobstructed. Ideally the centres of the 3D MOT chamber and science cell will be at the same height such that the centre of the transport trap will coincide with both. With a single rigid chamber this would require ensuring a good alignment during building the vacuum system. On baking a chamber, flanged joints relax and stresses redistribute causing slight bends in the system. This would cause misalignment of components, meaning a reduced line of sight and introduction of an offset between the centre of the 3D MOT chamber and the science cell.

By separating the mounting of the two sections such that they can be aligned with respect to each other this problem is removed. This is achieved by separating them with a flexible link, introduced through use of a CF16 UHV bellows connecting directly to the 3D MOT chamber and the additional pumping stage of the

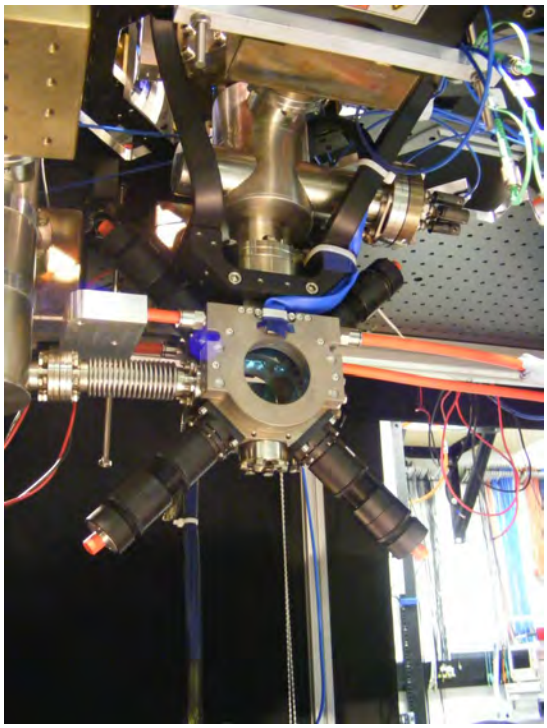

Figure 4.17: showing the aluminium clamp used to fix the 2D-3D MOT scheme in the plane. The clamp is constructed of two parts fixed together around the neck of the 3D MOT chamber using two M6 bolts. The clamp is fixed to the breadboard used for mounting the 2D MOT optics by legs fixed to the clamp in each corner. These slot into height adjustable clamps mounted onto the breadboard.

science cell.

The difficulty in mounting is then reduced to finding an appropriate way of holding the individual sections in a rigid and well-defined manner. To allow good alignment of the system it is desirable to fix each section in place as close to the most alignment critical part as possible, that is the 3D MOT chamber and glass cell. The 3D MOT chamber must be held rigidly with respect to the transport coil trap centre. This is complicated by the transport coils which, due to the system being mounted with the 2D-3D section vertical (a consequence of the microscope objectives forcing this coil orientation), have to pass under the whole experiment, making access to the optical table difficult. As can be seen in Figure 3.7R, due to the large radius of the transport coils it is difficult to fix the chamber to the optical table without using a long connection. The only obvious support points, the IGPs on either side, are undesirable due to the many connections between them and the 3D MOT chamber. This lead to the approach of supporting the weight of the system from above, by allowing it to hang freely on stainless steel wire ropes. The chamber is constrained in the plane using a clamp which does not have to bear the load of the whole system, allowing it to be much less substantial in size while retaining rigidity.

An aluminium frame was constructed around the system, extending from the table surface to above the system. As well as supporting the vacuum system this also supports an optical breadboard mounted around the system. This is to provide mounting for the 2D MOT optical system. Wire rope assemblies were attached the top of this frame and connected to each IGP, the IGPs themselves being a significant portion of the weight, and the four way cross mounted above the 2D MOT chamber. Each rope arm contains a spring to allow a tolerance in the load and a turnbuckle to allow adjustment of the tension in the rope, allowing alignment of the height of the system. To fix the system horizontally the clamp is fixed below the CF35 flange of the 3D MOT chamber, as shown in Figure 4.17. This is constructed of two pieces, held onto the chamber by pressure exerted using two M6 bolts. The clamp extends to each side of the flange and upward, without increasing the profile of the chamber with respect to the transport coils. On top of each corner are two fixing points for an arm which is slotted into an anchoring point. This is clamped onto the underside of the optical breadboard, in turn supported by the aluminium frame. When assembled the clamping system allows the chamber to be horizontally translated and then clamped in place. The height adjustment on the arm anchors not only allows for slight deviations from design parameters but also gives the possibility of additional height adjustment of the chamber. Using this set up the system was positioned such that the 3D MOT centre was at a height of 265±0.1mm, measured using a Vernier height gauge.

As with the 2D-3D MOT scheme, the science scheme is held using stainless steel rope assemblies to control height and a clamp to fix position in the plane. Ropes are fixed to the flange of the IGP and the valve at the top of the pumping stage. To create a balanced load, a counterbalancing weight was clamped around the valve with the two having weight equal to an IGP. This allowed for much easier control over tension in the ropes, and prevented drastic tipping or motion of the system when tension was released.

The cell is fixed in the plane by a clamp which closes directly onto the CF16 flange of the science cell using a V shaped clamp, as shown in Figure 4.18. This is to have the fixing point as close to the alignment critical part as possible without putting stress onto the glass metal transition of the cell. The clamp is attached to a one inch stainless steel bar, which in is inserted into a pocketed 2.5 inch brass bar, allowing a height adjustment to match the chamber height. This can then be clamped rigidly onto the optical table surface, fixing the cell in place. This clamp, intended as an initial design, only permits control over the yaw of the cell. As the wire ropes can be used to control the glass cell roll, only the pitch is unaccounted for.

To ensure good clear view along the transport path, to prevent atoms colliding with system walls, and to match the centre heights of the two chambers a laser was shone along the transport path. This was aligned to travel parallel to the surface of the optical table using a Vernier height gauge. The glass cell was then

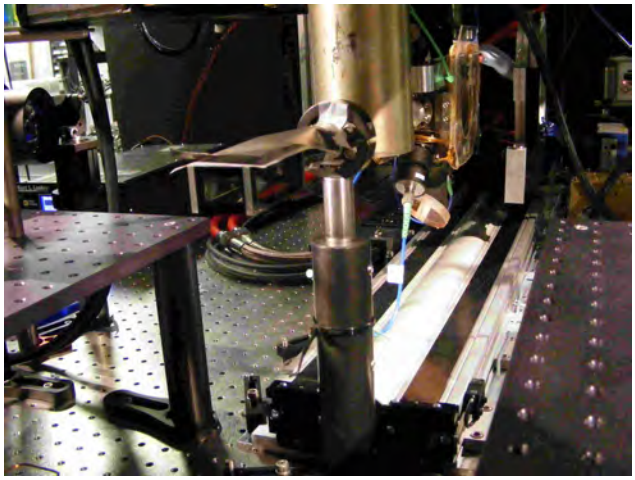

Figure 4.18: showing the clamp used to fix the science cell in the plane of the optical table. The brass clamp fixes around the CF16 flange of the science cell using two M4 bolts to close a V clamp. This is fixed to a one inch non-magnetic stainless steel bar using two inline M4 bolts to prevent rotation. The bar slots into a pocketed 2.5 inch base constructed of brass, allowing height adjustable fixing.

adjusted in height before being clamped such that the beam passing through the system was circular of the same size as the smallest aperture of the glass cell and the back reflection from the glass cell surface was in line with the incoming beam. Due to the glass cell clamp allowing no control over the pitch, the glass cell is tilted by 1°.

4.7 Performance analysis

The all-metal components were prebaked, then the more sensitive components connected and the system baked with a 150°C limit to reduce thermal stress on the epoxy bond. After baking the system showed pressures of order $5 \cdot 10^{-12}$mbar as measured with the IGPs shown in Figure 4.14. This is below their accuracy range. This was followed by a slow increase in pressure on the 3D pump, rising to of order 10^{-10}mbar. Pressures measured on the 2D and GC pumps remained below the 10^{-11}mbar level. After finding no perceptible leaks through helium leak testing the system was baked again to the same temperature. The rise was reproduced and is shown in Figure 4.19. The 3D pressure could then be maintained at the 10^{-10}mbar level by weekly firing of the TSP, with the 2D and GC pressures remaining of order 10^{-11}mbar or below. Pressures of this order would provide lifetimes of order 10s in the 3D MOT chamber and have been used for MOTs in other BEC experiments. As the pressure was somewhat lower in the glass cell, allowing expected lifetimes of order 100s, this was deemed reasonable until the pressure could be determined accurately using atom clouds. As the vacuum system was ahead of other aspects of the experiment it was necessary to wait until all the

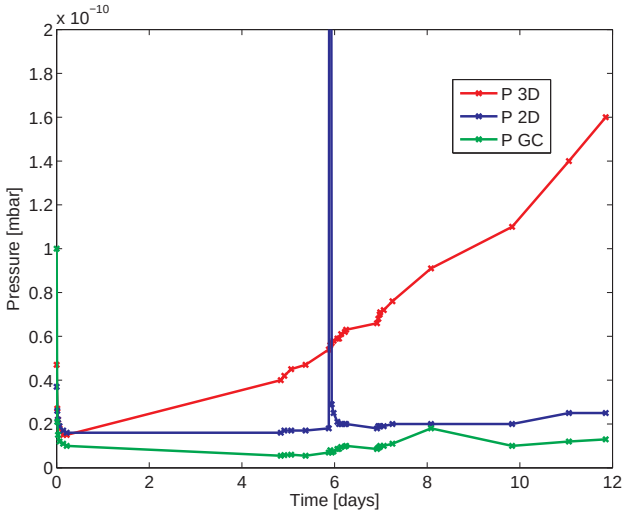

Figure 4.19: showing the rising pressure over twelve days directly following baking as measured on the system IGPs. The spike in 2D pressure is due to use of a dispenser.

required apparatus was prepared. These measurements revealed the pressure to be at best a factor of 4 higher than measured. For a more thorough discussion of the experiment UHV system performance see Appendix A.1.

4.7.1 Measurement of system pressure using atom clouds

Once the experiment was routinely producing magnetic traps it was possible to use trapped atoms to measure pressure in the system. This comprises two measurement techniques. The first is loading a MOT and measuring the rise and decay times when removing loading. The time at which the MOT reaches a steady state is determined by the balance of the loading and loss rates, with the loss rates being determined by light assisted collisions and background gas collisions. The second, more direct technique is to load a magnetic trap and measure the e^{-1} decay time or lifetime using absorption imaging, see Appendix B.2. This is limited by scattering with near resonant light and again the background gas. However, through careful shuttering and concealment of the laser system, the lifetime can be dominated exclusively by the background gas pressure. To investigate the rising pressure further, measurements were taken at the lower measured pressure, after firing of the TSP, and at higher measured pressures, after allowing a considerable rise induced by turning off the IGPs.

Typical MOT loading curves are shown in Figure 4.20, recorded by measuring the fluorescence of the MOT on a photodiode. Figure 4.20L shows the loading and out-loading at a pressure of $2.4 \cdot 10^{-10}$mbar in the 3D chamber, showing time constants of 2.93s and 3.28s respectively. Figure 4.20R shows the loading

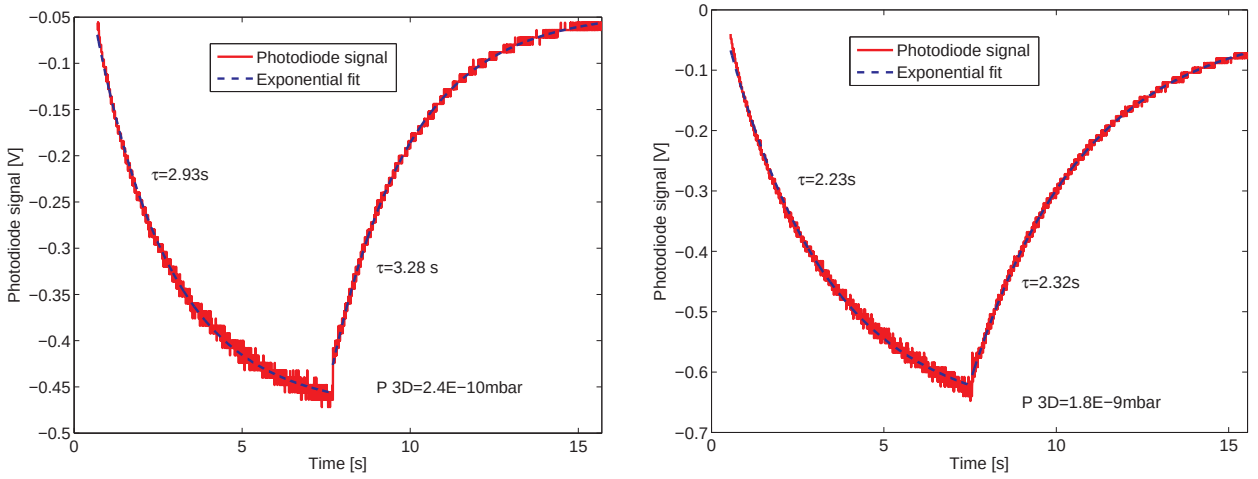

Figure 4.20: *Left:* showing the MOT loading and out loading curves at a measured pressure of $2.4 \cdot 10^{-10}$mbar. The time constants suggest a much larger loss rate than background collisions at the measured pressure. *Right:* showing the same measurements at $1.8 \cdot 10^{-9}$mbar. The change in time constant is roughly a factor of 7 less than would be expected from such a pressure change.

and out-loading at a pressure of $1.8 \cdot 10^{-9}$mbar in the 3D chamber, achieved by allowing the pressure to rise with pumps switched off, with time constants of 2.3s and 2.32s respectively. As the laser power settings were unaltered between the two measurements the difference in time constants is due to the variation in pressure. However, the reduction in time constant is at most a factor of 1.4 which is far less than the factor of 10 that would be expected from increasing the pressure by an order of magnitude.

To measure the lifetime in magnetic traps clouds were produced and then held for increasing times before taking an absorption image. The resulting image is then integrated, giving a number directly proportional to the number of atoms in the trap. Figure 4.21 compares the magnetic trap lifetimes of clouds held in the 3D MOT and science chambers at two different pressures. Each data point is an average of ten images. Increasing the pressure has a clear impact on the lifetime in both chambers. However, in the 3D MOT chamber a factor of five increase in the recorded pressure only reduces the lifetime by a factor of 1.7. As discussed in Section 4.2, assuming the lifetime to be limited solely by background collisions these measurements give a pressure of $5.7 \cdot 10^{-10}$mbar rising to $9.7 \cdot 10^{-10}$mbar. This is a factor of 3 different from the IGP reading in the lower pressure case and a factor of 1 in the high pressure case. This and the different factor between the change in lifetime and pressure suggest non-linearity in the pressure measurement of the 3D IGP. The IGP having a lower pressure reading than measured with the atoms is caused by the finite conductance between the two measurement points. However, this can not account for the non-linearity.

In the science chamber increasing the recorded pressure by a factor of 2.7 (while having a factor of 4

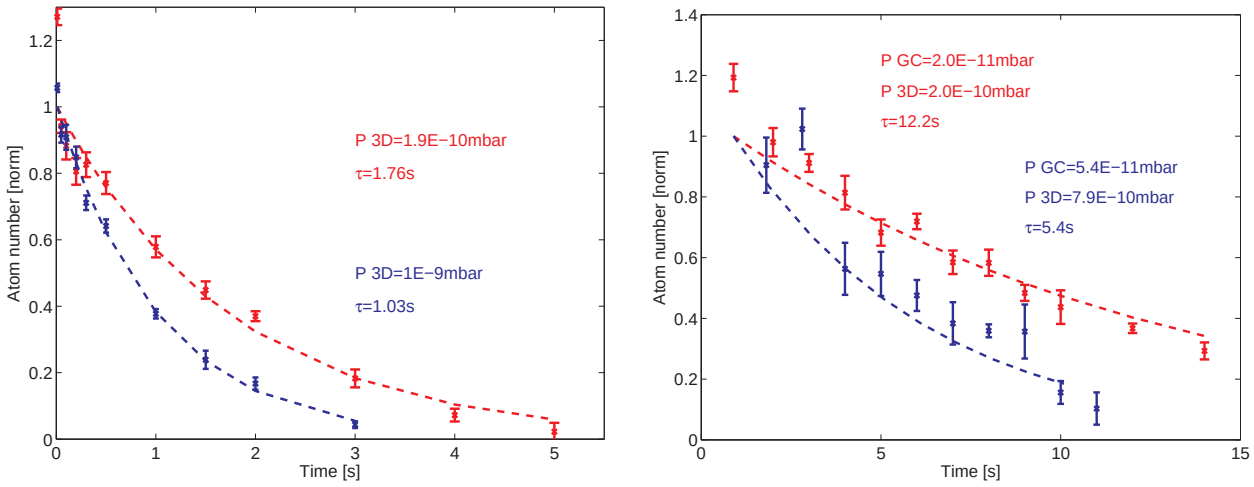

Figure 4.21: *Left:* showing magnetic trap lifetimes measured in the 3D MOT chamber measured using absorption imaging. A factor of five change in measured pressure only produces a factor of 1.7 change in lifetime. The lifetimes suggest background pressures a factor of 3 higher than measured in the low pressure case and a factor of 1 in the high pressure case. *Right:* showing magnetic trap lifetimes measured in the science chamber. Here the pressure change causes a similar scale change in lifetime. The lifetimes suggest measured pressures are off by 4.1 in the low pressure case and 3.5 in the high pressure case.

higher measured pressure in the 3D chamber) gives a factor of 2.3 reduction in lifetime. Again assuming background collisions are the limiting factor, these lifetimes correspond to a pressure of $8.2 \cdot 10^{-11}$mbar, 4.1 times higher than measured, rising to $1.9 \cdot 10^{-10}$mbar, 3.5 times higher than measured.

4.7.2 Further testing of the epoxy bonding technique

During extensive helium leak testing the only portion of the system displaying any response was the epoxy sealed 3D MOT chamber. To evaluate the likelihood that this was causing the slow rise in pressure, another identical 3D MOT chamber was constructed using the same process and design as Section 4.4. This was then attached to a small UHV system comprised of an IGP, a cold cathode pressure gauge and a valve separating these from a turbo-molecular pump and mass spectrometer. For details regarding the calibration of the mass spectrometer for helium see Appendix A.2 The system was baked at 150°C for one week. After cooling and the rest of the system being verified leak tight, an air tight bag was placed around the epoxy seal chamber. The trace is shown in Figure 4.22L, with an initial slope of $5.9 \cdot 10^{-8}$mbar/h and a rise time to 98% of 0.86 hours. To compare this with literature it is necessary to define the permeation constant, K:

$$\frac{dQ}{dt} = K \cdot \Delta P \frac{A}{d} \tag{4.11}$$

with $\frac{dQ}{dt}$ being the permeation rate, ΔP being the internal-external partial pressure difference, $A = 7.5 \cdot 10^{-5}\text{m}^2$ being the area of the bond (bond height $1 \cdot 10^{-4}$m and six windows, four with 27mm bond diameter and two with 66mm) and $d = 10^{-3}$m being the bond thickness. Calculation of the permeation constant gives $K = 2 \cdot 10^{-13}\text{m}^2/(\text{Pa s})$. This is much larger than the literature value of $0.7 \cdot 10^{-17}\text{m}^2/(\text{Pa s})$ [93]. The calibration of the mass spectrometer is unlikely to be inaccurate by more than a factor of ten in this pressure range. Instead, the discrepancy could in part be caused by curing at a higher temperature and for a longer duration, 150°C for two weeks compared to 80°Cfor 30 minutes. A more likely conjecture is that helium is travelling through the bond via a process faster than permeation. However, as under normal atmospheric conditions the helium partial pressure in air is a factor of $1 \cdot 10^5$ lower than under the above test conditions it is unlikely to be the cause of the high pressure in the system. Due to the linear dependence of (4.11), and other leak rates, an equilibrium partial pressure of $3.7 \cdot 10^{-}13$mbar can be expected. To support these findings the same measurements were taken with one of the original 70mm diameter single window test pieces with the trace being shown in Figure 4.22R. In this case, with $\frac{dQ}{dt} = 9.8 \cdot 10^{-9}$mbar/h, $A = 2 \cdot 10^{-5}\text{m}^2$ and the same bond thickness, the resulting permeation constant is $1.3 \cdot 10^{-13}\text{m}^2/(\text{Pa s})$.

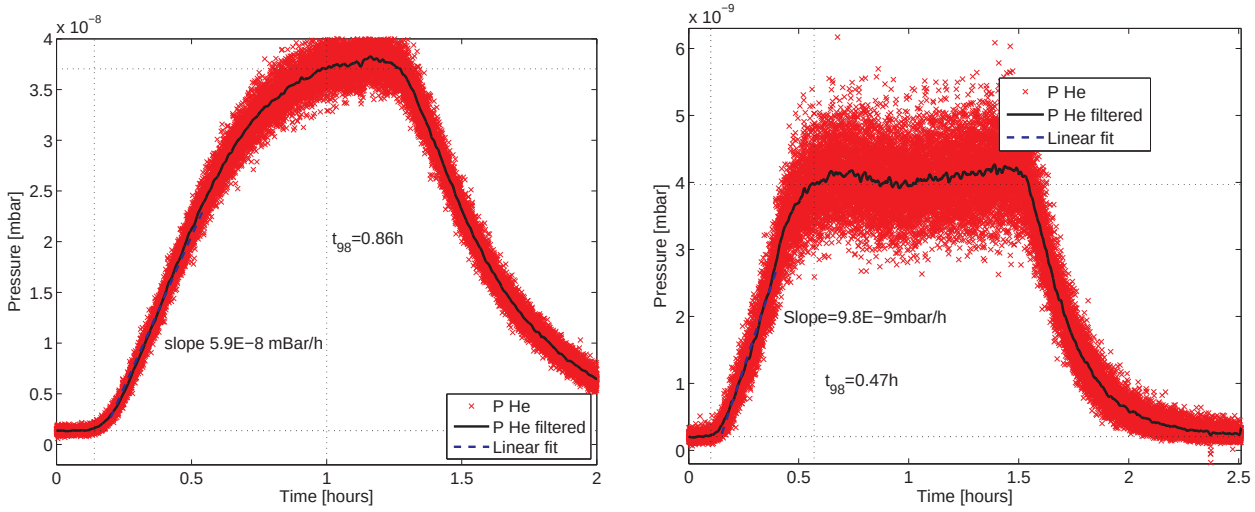

Figure 4.22: *Left;* showing the mass spectrometer helium trace resulting from helium bagging the assembled chamber replica. *Right:* showing the mass spectrometer helium trace resulting from helium bagging a 70mm viewport test piece.

To more closely examine the pressure rise, the replica test chamber was attached to a replica of the 2D-3D portion of the experiment system, only missing the 2D MOT chamber. To provide a more accurate measurement, a cold cathode gauge was placed in close proximity, conductance $\approx$ 70l/s to the chamber port, to the test chamber. The test system was first pre-baked to 350°C, reaching a pressure in the low

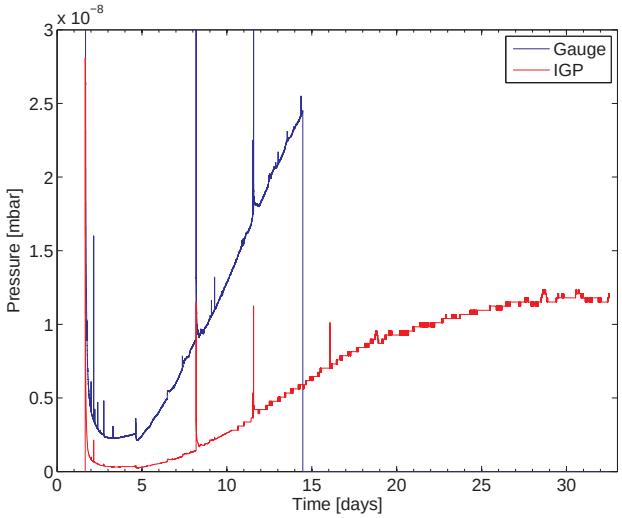

Figure 4.23: showing the rise in pressure, as measured on a cold cathode gauge and IGP, after baking the test chamber to 200°CÀt the highest gauge pressure the difference in measured pressure is a factor of five. The pressure rise takes of order a month to stabilise.

10^{-11}mbar. The chamber was then attached and the system baked at 200°C. Figure 4.23 shows the rise in pressure following bake-out. This shows a clear disparity between the gauge and IGP, with the gauge rising with approximately five times the gradient of the IGP. The time scale for the system to reach an equilibrium pressure of $1.2 \cdot 10^{-8}$mbar, as recorded by the IGP, is of order a month showing the slow dynamics of the system. It is interesting to note that the IGP pressure on the test system corresponds roughly with the pressure of the experiment system obtained through atom cloud measurements. This perhaps indicates some fault or contamination has occured on the experiment system.

The system pressure was then allowed to rise without pumping while being recorded with the cold cathode gauge, as shown in Figure 4.24L. This shows a rise of $\frac{dQ}{dt} = 4.8 \cdot 10^{-10}$mbar/h. Figure 4.24R shows a section of the trace in which the test piece was again placed in a helium atmosphere, resulting in a similar slope to that of Figure 4.22L.

The mass spectrum of the system was always dominated by water constituents, suggesting that this made up at least some component of the influx. To test whether water was passing through the bond, the chamber was wrapped in a sealed bag containing silica gel. This acts as a desiccant, reducing the humidity in the vicinity of the epoxy by approximately a factor of 3 over a time period of order minutes. Figure 4.25 shows the pressure as measured by the gauge and IGP, before the silica was placed in the bag, after, and after removal. The pressure initially rises for five days. Upon placing the silica in the bag, the slope reduces over four days until the pressure starts to decrease. When the silica is removed from the bag the pressure

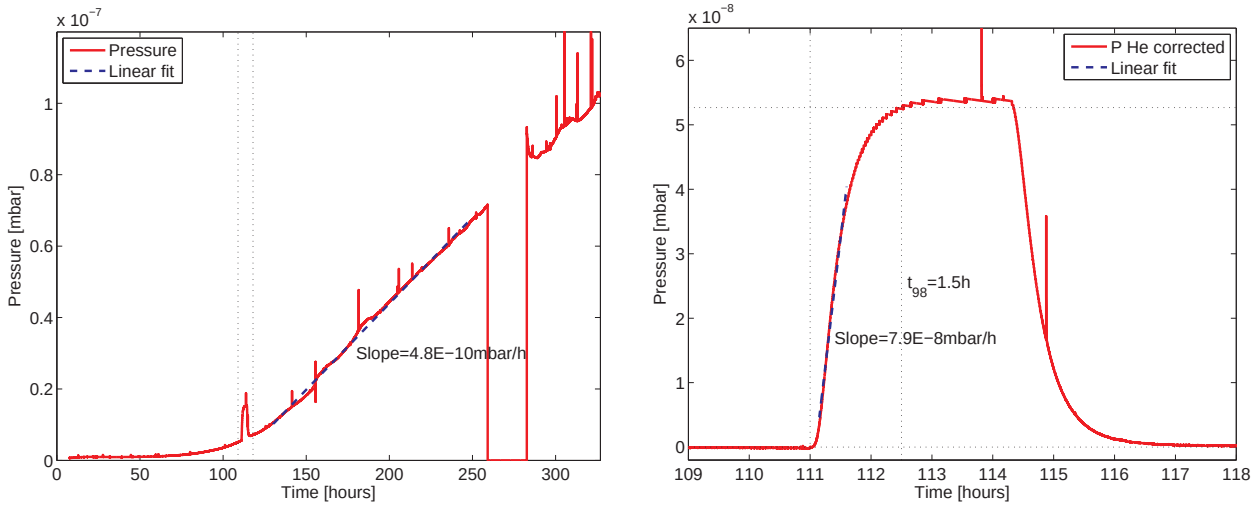

Figure 4.24: *Left:* showing the no pumping rise curve of the test system with assembled chamber replica as test piece, as recorded on a cold cathode gauge. Between 111 and 115 hours a helium bag was placed over the chamber. *Right:* showing the helium corrected partial pressure between 111-115 hours obtained by removing the slope of the left hand figure.

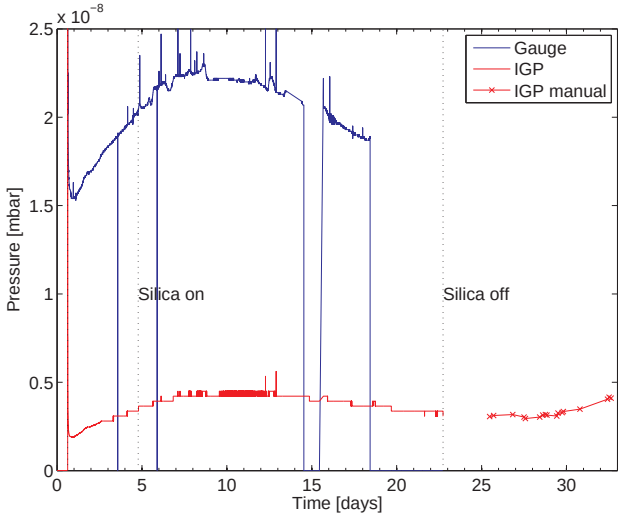

Figure 4.25: showing the effect of surrounding the replica chamber test piece with an environment of factor 3 lower humidity, formed using a silica gel desiccant. Upon addition of the silica the gradient decreases until the pressure starts to drop. Manual measurements from the IGP suggest that on removal of the silica the pressure begins to rise again on a similar time scale.

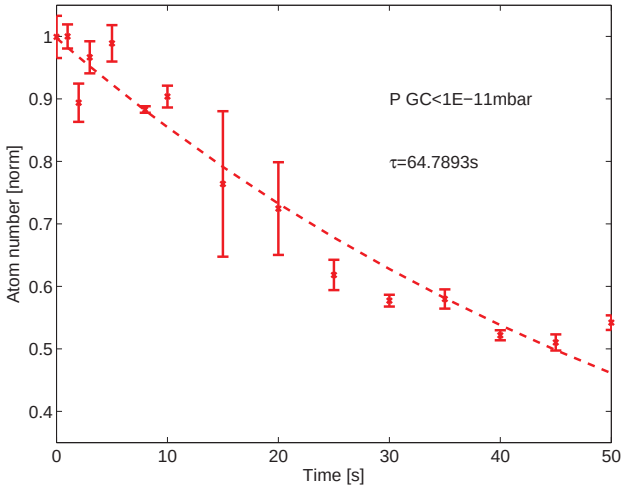

Figure 4.26: showing the magnetic trap lifetime measured (via absorption imaging) in the glass cell after replacing the epoxy bond with indium sealing. The lifetime of 64s is suitable for both loading and evaportion stages.

again begins to rise after a similar interval. This gives a strong suggestion that water is largely contributing to the rising pressure. As the diffusion rate of water through epoxy is generally low, the water is rather being absorbed by the epoxy due to a high solubility. This would explain the long timescales involved in the pressure rise of Figure 4.23, requiring several days for water to build up in the epoxy. Revisiting Figure 4.24L and calculating the permeation constant for a typical concentration of water vapour in air, 2%, gives $K = 8.8 \cdot 10^{-14}\mathrm{m}^2/(\mathrm{Pa\ s})$.

4.7.3 Resolving the rising pressure

With the rising pressure being proven to be caused by the epoxy bond it was necessary to further improve the technique. This work is on-going, and takes the form of placing a water proof buffer around the epoxy bond. This is currently being tested using a Viton buffer. However, due to the long time scales (several months) involved in testing, an alternative solution has been used for the experiment system at least until the epoxy technique is rectified. This is simply to use the existing chamber design and replace the bonding epoxy with indium as in [78]. However, for simplicity, the smaller viewports have been replaced with commercial products. This has no impact on the thickness or overall design of the chamber but does require the use of divergent beams for magneto-optical trapping. Another drawback is the limited baking temperature of 120°C. However, the modified system has been baked and is now displaying pressures below $1 \cdot 10^{-11}$mbar. Atom cloud measurements have been performed, finding lifetimes of order 60-70s in both the 3D and GC chambers. Figure 4.26 shows the lifetime in the glass cell after exchanging the 3D MOT chamber. This is

entirely suitable for both loading and evaporative cooling stages and should not cause any obstacle towards reaching condensation.

4.8 Summary & Outlook

The UHV system has been designed with a modular set up, providing separate sections for preparing each species and a final chamber in which the later stages of the experiment are performed. Each species can then be prepared using a 2D-3D MOT set up to permit high atom numbers with long confinement times. The system has initially been set up with one 2D-3D MOT set up for both potassium and rubidium. The 2D and 3D MOT chambers are separated by a differential pumping stage which restricts the gas flow between them. The second differential pumping stage, allowing a lower pressure in the glass cell as compared to the 3D MOT, has been proven effective, with atom cloud lifetime measurements showing an order of magnitude lower pressure in the glass cell.

The system required a narrow profile along the magnetic transport direction. This was achieved through use of an epoxy sealing technique, allowing a 3D MOT chamber size of just 36mm whilst retaining good optical access. Using initial test pieces, measured pressures of below $1 \cdot 10^{-11}$mbar were reached. However, after construction of the UHV system a slow rising pressure was observed in the 3D MOT chamber. This reached a measured pressure of $1 \cdot 10^{-10}$mbar when firing a TSP once a week. Using atom cloud measurements this pressure was shown to be a factor of 3 higher than displayed. Similar measurements in the glass cell showed a system pressure a factor of 4 higher than measured. This discrepancy is due to the finite conductance between the two measurement points. The lifetime provided in the glass cell was of order 12s, too short for an optimised evaporative cooling scheme.

The cause of the rise is water permeation through the epoxy bond with a permeation constant of $K = 8.8 \cdot 10^{-14}\mathrm{m}^2/(\mathrm{Pa\ s})$. After baking, the epoxy bond is depleted of water and gradually refills over approximately a month. Measurement of the permeation constant for helium gave a value larger than literature, suggesting that the transport through the bond could be taking place through a faster process. In an attempt to alleviate this problem, testing of a buffer seal to prevent water from accessing the bond will be performed.

Due to the long time scales involved in testing such a buffer, a new chamber of near identical design was constructed for the experiment. The sealing point is simply replaced with an indium seal [78]. The modified system has been baked and is now displaying pressures below $1 \cdot 10^{-11}$mbar. Atom cloud measurements have been performed, finding lifetimes of order 60s in both the 3D and GC chambers. This is entirely suitable for both loading and evaporative cooling stages.

CHAPTER 5

SPATIAL LIGHT MODULATION & DETECTION AT HIGH RESOLUTION

5.1 Introduction

The purpose of this chapter is the design and characterisation of the optical system used for high resolution imaging and imprinting a spatial light modulator (SLM) pattern onto the atomic plane. Obtaining information on the length scale of an optical lattice requires an imaging system with a resolution of order the lattice spacing. The spacing, a, produced in a standing wave optical lattice is given by $\frac{\lambda}{2}$ for retro-reflected beams having wavelength λ. For a two dimensional lattice the spacing can be increased by instead using two crossed beams to give a spacing governed by $\lambda = 2a \sin \frac{\theta}{2}$ with θ the angle between the beams. The spacing of the proposed lattice configuration, 1μm, has been chosen to allow a resolution achievable using commercially available microscope objectives. The use of such is ideal, as they are designed to focus onto a planar sample much like that provided by a two dimensional lattice.

The use of a microscope objective also gives the possibility of demagnifying optical fields and imaging them directly onto the trapped 2D cloud. This is ideally suited for implementing a spatial light modulator (SLM), a device which imprints a pixelated pattern onto a light beam. This will allow production of a highly controllable potential landscape for the atom cloud. By placing a microscope on either side of the 2D space, sandwiching them around the atoms, it will be possible to achieve high resolution imaging and have the ability to control the potential on a similar length scale. This grants a range of interesting applications. For example, the SLM could be used to generate lattice potentials with control over the spacing while the imaging objective would allow resolution of single sites in the lattice. The SLM is also intended to provide a disordering potential with imaging then being possible over distances of approximately the disorder grain size. The SLM

could also be used to remove the harmonic envelope imprinted onto an optical lattice by the Gaussian profile of the lattice beams, allowing more accurate reproduction of condensed matter systems. Having a potential which is controllable at will, without the need for any careful realignment of opto-mechanics, obviously adds a valuable tool to a cold atom experiment. The use of the microscope objectives is further motivated by the recent successful achievement of single site resolution in [12] and [13]. The latter also possesses a novel method for the addressing of single sites in the lattice [94]. This makes use of a highly focused off-resonant beam to selectively remove atoms. However, this technique does not allow the production of fine scale patterns as would be possible using an SLM.

Early work focusing on manipulation of particles using an SLM focused on creation of optical tweezers for colloidal physics experiments [95], for example [96] in which a phase modulated nematic crystal SLM is used to control the position of 1μm diameter silica spheres in a suspended in water. Having such precise control over an array of cold atoms is obviously highly desirable. Work towards this goal began with loading arrays of optical dipole traps from a magneto-optical trap [97]. Using a nematic crystal SLM having a pixel pitch of 40μm allowed realisation of up to five individually addressable micro-traps spaced as close together as 4μm. Furthermore, using control over the two-body loss rate (through tuning of the MOT density) it was possible to ensure only one atom was trapped per trap, having implications towards creation of quantum bits. Manipulation of a condensate was later demonstrated in [98], where the diffraction pattern from a phase modulating ferroelectric liquid crystal SLM is used to split a condensate into up to three pieces. These could be moved in the plane perpendicular to illumination beam. The application of an SLM onto a condensate has since allowed production of various novel potentials including controllable power law traps [99], ring traps [100, 101] including broken ring traps and rings which allow storing of atoms in dark spots [102] and to create and observe dark solitons and soliton collisions in a condensate [103]. These experiments predominantly make use of phase modulating spatial light modulators. However, in a recent paper [104] an amplitude modulating digital micro-mirror SLM has been used in an attempt to remove optical disorder, such as interference fringes due to dust, when observing a Mott insulating system. In [105] an amplitude modulation SLM has been used to confine cold (but still thermal) atoms in two dimensions, including confinement of two atoms within a trapping volume of 1.5μm. This and the high power threshold of micro-mirror devices suggest that it should be possible to realise an optical lattice capable of entering the Mott insulator regime using only a SLM.

Imaging an SLM directly onto the condensate will introduce problems familiar from detection systems. Due to the typically high intensity requirements for producing an optical lattice, using a laser is highly

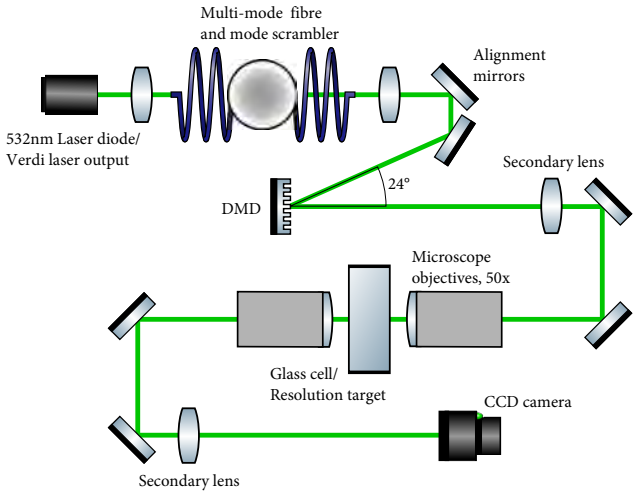

Figure 5.1: showing the optical system used for testing the projection of SLM patterns into the image plane of the microscope objectives. Light at 532nm is provided by a frequency doubled Nd:YAG laser. This is coupled into a multi-mode fibre to produce a speckle pattern output. A technique is applied to reduce the speckle pattern to a near top-hat beam. This is collimated and directed onto the SLM at an angle of 24°. The SLM pattern splits the beam into two components and directs one through the secondary lens and microscope objective. This combination images the SLM surface onto the focal plane of the objective. The second objective and secondary lens pair then images the focal plane distribution onto a camera for measurement. Testing has been undertaken with the glass cell and a resolution target.

desirable over an incoherent light source such as a high power LED. Shining a coherent beam through an optical element produces an étalon effect where the beam interferes with a back reflection creating interference fringes. In detection systems the appearance of these fringes dominates raw images but can be removed by subtracting a background image without the atom distribution. Fringes persist at some level due to vibrations or motion of optical elements causing path length changes across the beam and shifting fringe positions slightly, preventing perfect removal. For the SLM system, the problem is more critical as the atoms experience the light pattern directly meaning no post processing can be performed. This has led to the development of an illumination scheme in which the beam is passed through a multi-mode optical fibre to produce a speckle pattern. This is then manipulated to be homogeneous on time scales faster than those relevant to atoms in the experiment.

5.2 Overview

The imaging system will be built around the vacuum system. Specifically, the microscope objectives will be placed on either side of the science cell described in Section 4.3.3, with one providing detection and the other manipulation. Each side then serves a separate purpose, the detection side to produce an image of the 2D

atom cloud onto a camera and the manipulation side to produce an image of the output of an SLM in the plane of the 2D atom cloud. The optical system is shown schematically in Figure 5.1.

Beginning with the SLM side of the system, light is provided by a commercial frequency doubled Nd:YAG (a Verdi from Coherent) laser system, giving light of wavelength 532nm with a power output of up to 12W. This choice of wavelength is motivated by the linear scaling with resolution, a 532nm source allowing both a good resolution and a commercially available laser. This is coupled into a multimode fibre with numerical aperture 0.48. This serves two purposes, to produce an incoherent speckle pattern and to pass the beam over the laboratory to the main experiment system. A low power frequency doubled Nd:YAG laser was used for initial testing, providing approximately 4mW of 532nm light.

The microscopes objectives are telecentric and infinity corrected, requiring a collimated beam as input or use of a secondary tube lens for imaging. The output from the fibre is collimated and directed using two mirrors onto the active surface of the SLM. The SLM divides the beam into two components determined by the SLM on and off states. The off state is directed to a beam dump while the on state passes through the first objective and a secondary lens, also known as a tube lens in microscopy. The secondary lens is used to take the collimated beam and focus it such that the objective can form an image of the SLM in the work plane. The detection side of the imaging system images the light from the atom plane onto a high resolution digital 12 bit CCD camera, a Pixelfly from PCO imaging. This is a high quantum efficiency device with a double shuttering mode to allow fast exposure times. The image is magnified to cover the CCD chip. This is achieved by placing the CCD surface in the back plane of the objective and secondary lens. For alignment purposes and to keep the system design compact, two mirrors are placed between each secondary lens and objective pair.

5.3 Imaging considerations

As discussed in Section 3.9, the optical potential experienced by an atomic ensemble is proportional to intensity. To understand how an SLM pattern will influence the potential it is necessary to understand the effect that the imaging system will have upon the pattern. The SLM will produce a pattern which, when imaged onto the condensate plane, is pixelated on a length scale below the resolution limit of the imaging system. For any two dimensional linear system, the input and output electric fields are related by the superposition integral [106]

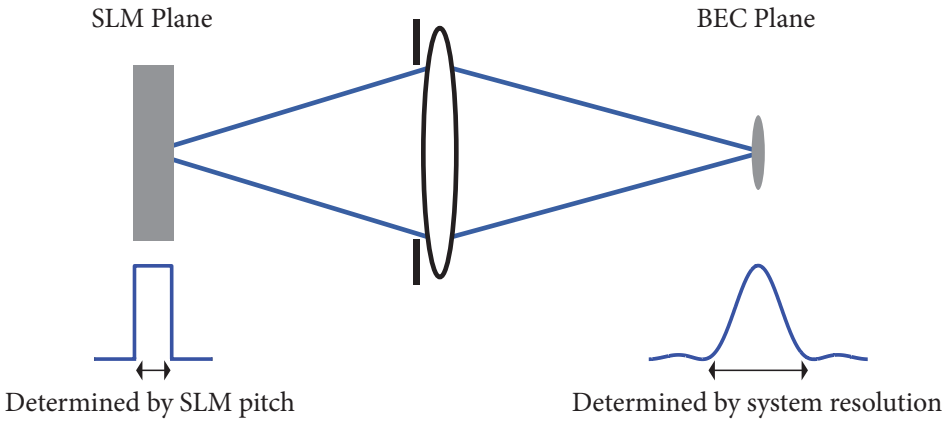

Figure 5.2: showing the effect of the optical system upon the SLM distribution. Micro-mirrors on the SLM reflect an approximately top-hat function. This is then filtered by the optical system according to (5.1). As when magnified each micro-mirror is below the resolution limit of the optical system, the resulting distribution in the image plane is then an Airy disc.

$$g_2(x_2, y_2) = \iint_{-\infty}^{\infty} g_1(\xi, \eta)\, h(x_2, y_2; \xi, \eta)\, d\xi\, d\eta \tag{5.1}$$

where the function h is the response of the system to a δ function at coordinates (ξ, η) in the input plane, known as the point-spread function (PSF). In essence, the output field is built up from a series of PSFs distributed according to the input field. For a diffraction limited system the PSF is given by the diffraction pattern from a circular aperture, the Airy disc

$$h(x_2, y_2; \xi, \eta) = \frac{2J_1(f(x_2, y_2, z; \xi, \eta))}{f(x_2, y_2, z; \xi, \eta)} \tag{5.2}$$

where J_1 is the first order Bessel function of the first kind and z is the plane separation. The result is that an SLM pixel demagnified onto the atomic plane using a microscope objective such that it is below the resolution limit of the system will be blurred over the length scale of the PSF. Effectively each SLM pixel acts as an impulse input to the system as shown in Figure 5.2.

As for measurement the image plane distribution has to pass through a second objective, (5.1) is reapplied to find the resulting distribution in the camera plane. The influence of both objectives upon an input point source is then a convolution of two Airy discs. This will effectively decrease the apparent resolution. Figure 5.3 shows the intensity of an Airy disc compared to that of a convolution of two Airy discs. To reproduce the 26.3% central dip the convoluted function must be separated by a distance a factor 1.33 further apart. As such an observed resolution limit of 0.707μm can be expected.

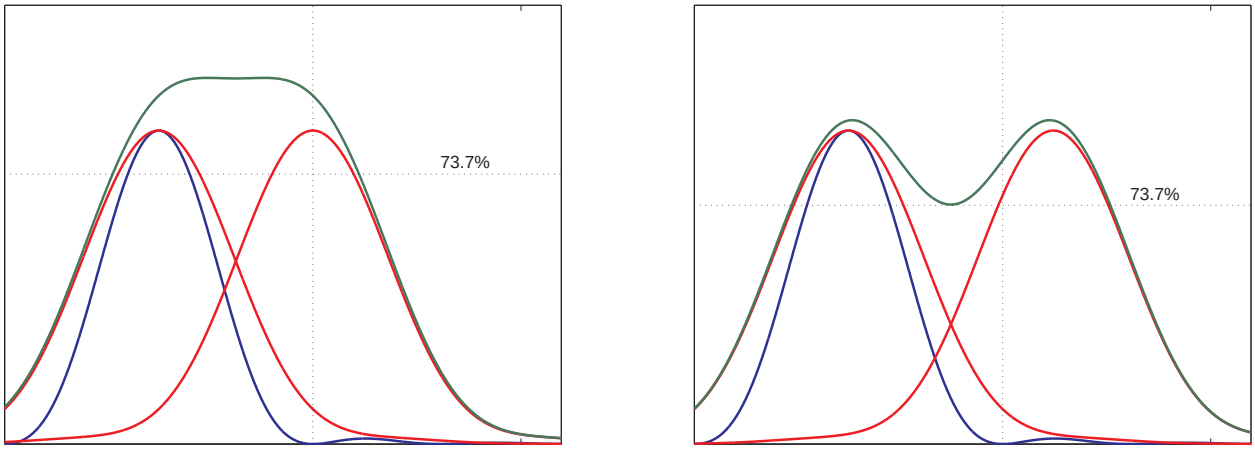

Figure 5.3: *Left:* showing a representation of the intensity in the camera plane when separating two SLM pixels according to the Rayleigh limit. An impulse input to the optical system is converted to an Airy disc (blue) by the first microscope objective. After travelling through the second microscope objective the distribution becomes the convolution of two Airy discs (red). As such, a Rayleigh criterion resolvable feature in the image plane is not resolvable on the camera (green). *Right:* showing the situation when resolvable using the Rayleigh criterion (using the same dip % as that for two Airy functions). This occurs when features are 1.33 times further apart.

5.4 Spatial light modulator system

Imprinting a pixelated pattern onto a beam requires an array of active elements capable of locally modulating either the amplitude or phase, or both, of the beam. The majority of commercially available SLMs achieve this using liquid crystal (LC) or liquid crystal on silicone (LCoS) technology. These modulate the phase of the beam by changing the refractive index of a pixel, usually to give a phase shift of π. Amplitude modulation can then be achieved by adjusting the polarisation shift of the beam such that it is attenuated by a filter when a pixel is active. Another approach is to use a digital micro-mirror device (DMD - not to be confused with a deformable mirror device). DMD arrays use micro-mirrors with two tilt positions to divide a beam into two components. By directing the light from one tilt state out of the optical system the DMD acts as an amplitude modulator.

Using an SLM to pixelate a beam can be achieved in either a transmissive or reflective geometry. Reflective systems tend to have higher light efficiency [107] and much lower dispersion when compared to chromatically compensated transmissive optics. This makes a reflective system more suited to applications which require high throughput or broadband sources. However, transmissive systems are generally much easier to align and also allow for a far more compact system, while reflective optics generally require folded optics solutions to allow a reasonable system size.

5.4.1 Spatial light modulator specifications

The experiment SLM is a high speed, high resolution DMD device supplied by Texas Instruments as part of their D4100 developer kit. It is an array of 1920x1080p aluminium micro-mirrors with a pitch of 10.8μm and fill factor of 92.5%. Each mirror represents one pixel in an image produced by the SLM. A mirror is attached to a yoke which is in turn connected to a torsional hinge. The mirror is either tilted such that the yoke rests on a landing point in one of two active positions, at $\pm 12°$, or allowed to float freely when not in use. The tilting is controlled by the electro-static force generated by two electrodes, each placed under one of the unconstrained mirror corners. These are in turn controlled by a dual CMOS memory cell which is located below the mechanical portion of the mirror. The state of the memory cell does not directly determine the state of the mirror as once the mirror has landed it is locked in place until it receives a reset signal, unlocking the mirror and allowing it to move to the position determined by the electrodes. This allows the electro-static portion of the system to be preloaded, meaning that on a reset signal the state of all mirrors can be altered simultaneously. A single micro-mirror is a MEMS object and as such they are created in sheets with manufacture leaving a region, approximately ten mirrors wide, of permanently floating pixels around the active region.

The DMD is used to imprint an amplitude modulation onto a beam by selectively removing portions of the beam. This is achieved by illuminating the mirror array such that the light from only one of the mirror states, the on state, is captured by the rest of the optical system while the rest, the off state, is directed into either a beam dump or camera to capture the inverse of the on state. Given the $\pm 12°$ range of the micro-mirrors, when using the $+12°$ as on, an ideal illuminating angle is -24°, as shown in Figure 5.2. Using this scheme the on state then reflects normal to the DMD surface, allowing the whole DMD plane to be in focus and also providing much simpler alignment of the rest of the optical system.

The specified light efficiency of the DMD is 68%. Significant losses arise from an 88% reflectance for the aluminium mirrors and the 92.5% filling factor. There is also a window with broadband coating, with an efficiency of approximately 97% for four passes. However, using the illumination angle above, any light loss due to reflections from surfaces other than the on state mirrors will be deflected out of the optical system, as with light from the floated state. This allows the DMD to retain a high contrast ratio despite large losses.

The DMD is specified as capable of achieving 21,348 frames per second but this is practically limited to 10,700Hz by the memory on the control board. The maximum optical intensity is rated at $25 W cm^{-2}$, with the device having a total active area of 20.736mm by 11.664mm. In practice additional cooling would be necessary to keep the device within the working temperature range when using high optical powers.

The current tube lens, focal length 200mm and diameter 24mm, prevents the whole SLM distribution from passing through the system. Treating each mirror as a source for a diverging beam gives a divergence of order $\theta = \frac{\lambda}{\pi w_0} \approx 0.03$ using w_0 equal to half the mirror pitch. The maximum dimension of the SLM surface that can currently be used is then $d_{lens} - 2f \tan\frac{\theta}{2} \approx 17.5$mm. Demagnified into the image plane the SLM surface then has dimensions 350μm by 230μm.

5.4.2 Control system

The DMD device is operated through the Texas Instruments control board. The primary components of the chipset are two Xilinx Virtex 5 FPGAs. The first of these is the DDC4100 chip, an FPGA with no user programmability, which controls the DMD device both directly and through the two DAD2000 drivers. The DAD2000 drivers are used to power the DMD and issue the reset command to allow the mirror to change state. Communication between the control FPGA and user is provided by the ALP-4.1 high-speed Application Programming Interface (API) from ViALUX. This is a Xilinx Virtex 5 FPGA which is user programmable and controlled using a set of ALP commands. It serves the purpose of handling user input and converting this into a language suitable for the control FPGA. It also places data, such as images or sequences, into the on-board memory before running the DMD to avoid bottle necking caused by data-transfer.

To control the SLM an object orientated C++ program was developed [14]. This passes settings and images to the API through use of a series of ALP commands. For use in testing the system the control code is also capable of producing a series of testing images. This includes grids, square and sine waves of variable modulation frequency, mathematical functions such as harmonics, and randomised images or speckle patterns. The program also has built in greyscale interpretation for reading in colour images and can be used to generate sequences.

5.4.3 Mounting

The DMD device must be mounted at a rotation of 45° from horizontal to keep the mirror tilting direction vertical. This allows for all of the mirror states to reflect light in the horizontal plane, making alignment of the system far simpler. To achieve this, and bring the DMD centre to an appropriate beam height, a custom mount was designed. This also allows some rotation of the DMD to account for the device to device error in the tilting angle (specified as ±1°) and the possibility of improving contrast. The base of the mount acts as a large flat, allowing good access for ensuring parallelism between this and the base plate of the microscope objective mounting. This makes translating the DMD surface such that it is aligned with the rest of the

optical system trivial, and also allows easy removal and replacement of the DMD for testing with a simple mirror. The mount is open at the rear to allow addition of a more substantial heat sink as this will be necessary with high power beams. The mount is built into a cover to act as a dust shield.

5.4.4 Numerical comparison of binary and grey scale pixels

To produce grey scale patterns, SLMs use a time varying binary signal to give an intermediate intensity. As discussed in Section 2.3, having a time independent potential is necessary for producing an Anderson localised sample. However, having a grey scale potential is more versatile, allowing the creation of smoother patterns. Due to the blurring of each mirror pixel on passing through the optical system, multiple mirror pixels will overlap in the image plane. This gives rise to the possibility of creating a grey scale pattern using a binary SLM. To determine to what extent this is possible the two situations have been compared numerically. The objectives will demagnify a single micro-mirror to a size of 0.21μm. This places each pixel below the resolution limit of the optical system. The SLM plane can then be represented as an array of point sources, having magnitude 1 or 0 for the binary case or a value between 1 and 0 for grey scale. The field in the image plane is then given by the sum of the contributions from each pixel, with each pixel having an Airy disc envelope. Each pixel is separated from neighbouring pixels by 0.21μm.

For an incoherent light source the side lobes of the Airy disc are less significant, and add in intensity rather than in the field. As the illumination of the SLM is intended to be incoherent a Gaussian envelope has been used. This approximates an incoherent source. The intensity in the image plane is then:

$$I_{image}(r) = \sum_{pixels} I_0 v(r - r_p) \approx \sum_{pixels} I_0 \exp\left(\frac{-\left[(x - x_p)^2 + (y - y_p)^2\right]}{2\rho^2}\right) \tag{5.3}$$

with ρ controlling the width of each pixel envelope. In the following the width of SLM pixels in the image plane will be quoted as the distance over which a pixel envelope decays to e^{-2} of the initial value.

The width of a pixel in the experiment system is expected to be of order 0.532μm. By defocusing the microscope objective it would be possible to increase the pixel width. Due to the telecentricity of the objectives this should be possible without changing the separation of the pixels. This may be useful in realising smoother potentials, by providing additional blurring to allow more overlapping. In reality the width of the Gaussian will be limited by the imaging system used while the pixel density will be limited by both the imaging system and the SLM. In the following, two cases are considered numerically, first trying to produce a smooth harmonic potential. This would be valuable for production of controllable harmonic traps,

or to remove the additional harmonic confinement imposed onto an optical lattice by the gaussian shape of the beams. The latter application has recently been studied experimentally in [108], where a Gaussian beam is corrected to have an RMS flatness of 1.5% using a binary SLM. Initial experiments using such a technique have already been performed [104]. The second case is a disordering potential, having obvious benefits towards realisation disordered transport experiments.

Harmonic potentials

Producing a smooth potential would obviously be simpler with grey pixels as the intensity could be increased by small amounts from pixel to pixel. For binary pixels producing such a potential shape would require alternate pixels being on or off such that the total intensity decreases as smoothly as possible. The density of pixels which are on would need to change according to the function required. To achieve this for an arbitrary potential would require telling each pixel whether it should be on or off based on the status of all other pixels which overlap within a certain distance. Improvement could then be made readdressing each pixel to test the possibility of improving the smoothness. An approximate approach has been used where a random number is compared to the required function, normalised such that the maximum value of the function coincides with the maximum obtainable random number. The result is that the pixel density varies as required on average. An example of an SLM distribution for a parabolic function is shown in Figure 5.4. The downside of this approach is that the overall picture retains features resulting from the randomness.

Examining the resulting images for various widths, shown as a central slice in Figure 5.5, reveals that pixels extending over larger widths result in smoother variations. This is to be expected as for narrow widths pixels overlap with fewer neighbours. To produce a smooth potential several nearby pixels must overlap sufficiently. It is also clear that pixel widths larger than the objective resolution are required for a smooth potential. This may be possible through defocusing of the microscope objective.

Disorder potentials

Producing a disordered SLM distribution simply requires randomly assigning the value of each pixel as 0 or 1 for binary pixels or a random number between 0 and 1 for grey pixels. Flat probability distributions have been used with each value being equally likely. Figure 5.6 compares the two cases for a FWHM of 0.532μm. As would be expected, the binary SLM produces a higher contrast pattern, having an 11% offset compared to 30% for grey scale. This would have the consequence of requiring a higher laser power to reach the same disorder strength with a grey scale SLM. The average size of a modulation, measured using the peak of

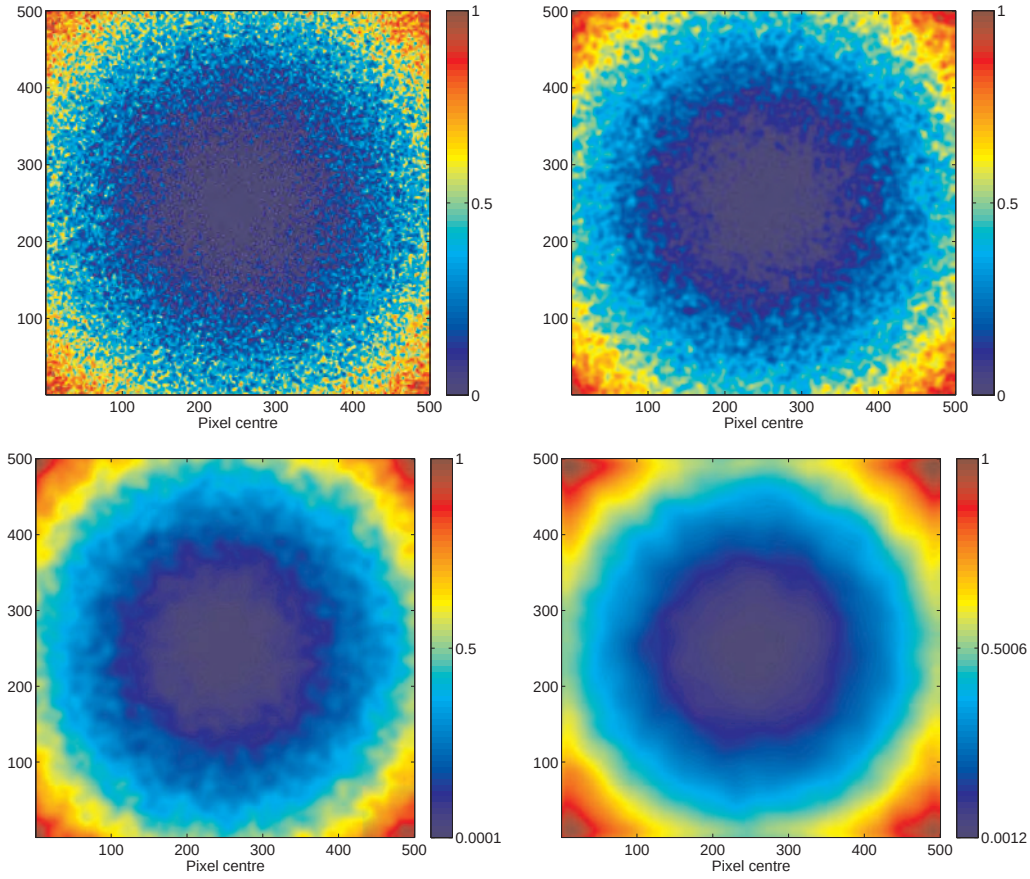

Figure 5.4: showing the numerical simulation of the image plane intensity for the representation of a parabolic potential using only binary SLM pixels. The image width is 114μm with SLM pixels having 0.21μm separation. Image plane pixel e^{-2} widths are, top left 1.05μm, top right 2.52μm, bottom left 5.25μm and bottom right 10.5μm. This shows pixel widths larger than the resolution of the microscopes are required to produce a smooth potential with a binary SLM.

the auto-correlation function, is approximately equal. Long distance correlations appear due to pixels being distributed in a grid. Binary pixels outperform grey scale, although a grey scale SLM could also be used to produce binary.

Summary

The blurring of the SLM pixels as they pass through the optical system allows a binary SLM to perform similar tasks to one having grey scale. However, producing smooth harmonic potentials would require a larger pixel width than the resolution of optical system in order to provide additional blurring. This could be achieved by swapping the objective when wanting harmonic potentials, and perhaps by defocusing the telecentric microscope objective. For producing disorder potentials a binary SLM achieves a factor of 3 lower

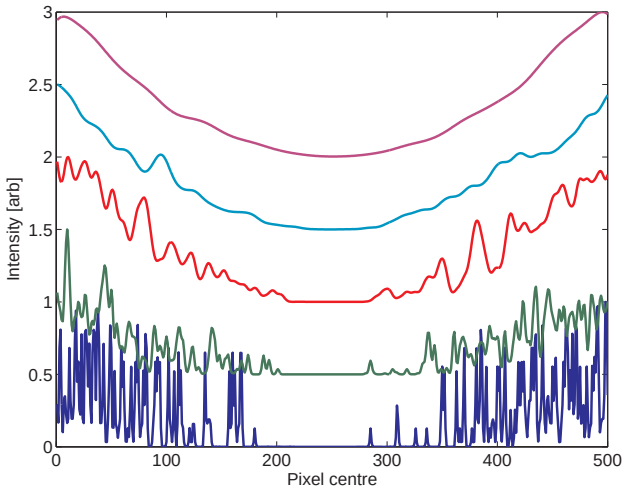

Figure 5.5: showing central slices of the image plane intensity for the images of Figure 5.4. Image plane pixel e^{-2} widths are: dark blue 0.53μm, green 1.05μm, red 2.52μm, light blue 5.25μm and magenta 10.5μm. The traces have been offset for clarity.

intensity offset due to having larger modulations from pixel to pixel. As a binary SLM is more suitable for pursuing Anderson localisation it is certainly preferable for producing disorder. One situation in which a grey scale SLM will certainly outperform binary is when trying to produce a smooth potential with requiring more than one length scale of pixel, i.e. a pattern with both large and fine structure scales. This could be useful in creating a lattice and a harmonic envelope both on the SLM, to remove the effect of having a Gaussian beam profile.

5.5 Development of a multi-mode illumination source

Using coherent light for imaging leads to the appearance of fringes, arising from interference caused by back-reflections in the beam. As imaging the SLM onto the atoms directly allows no fringe reduction through post-processing, it is necessary to suppress this effect from the beginning. An obvious option is to investigate what is available using incoherent sources such as LEDs. While it is possible to reach high light powers using an LED, the piece usually contains multiple sources, making collimation and collection of the light difficult, requiring the design of a condenser system. A more desirable option is to attempt coherence reduction of a laser beam.

One technique for suppressing coherence involves coupling coherent light into a multi-mode optical fibre. The output of this is then a speckle pattern, arising from interference between the occupied modes of the fibre. As both detection and imaging of a SLM require a well-defined beam profile this is obviously not very

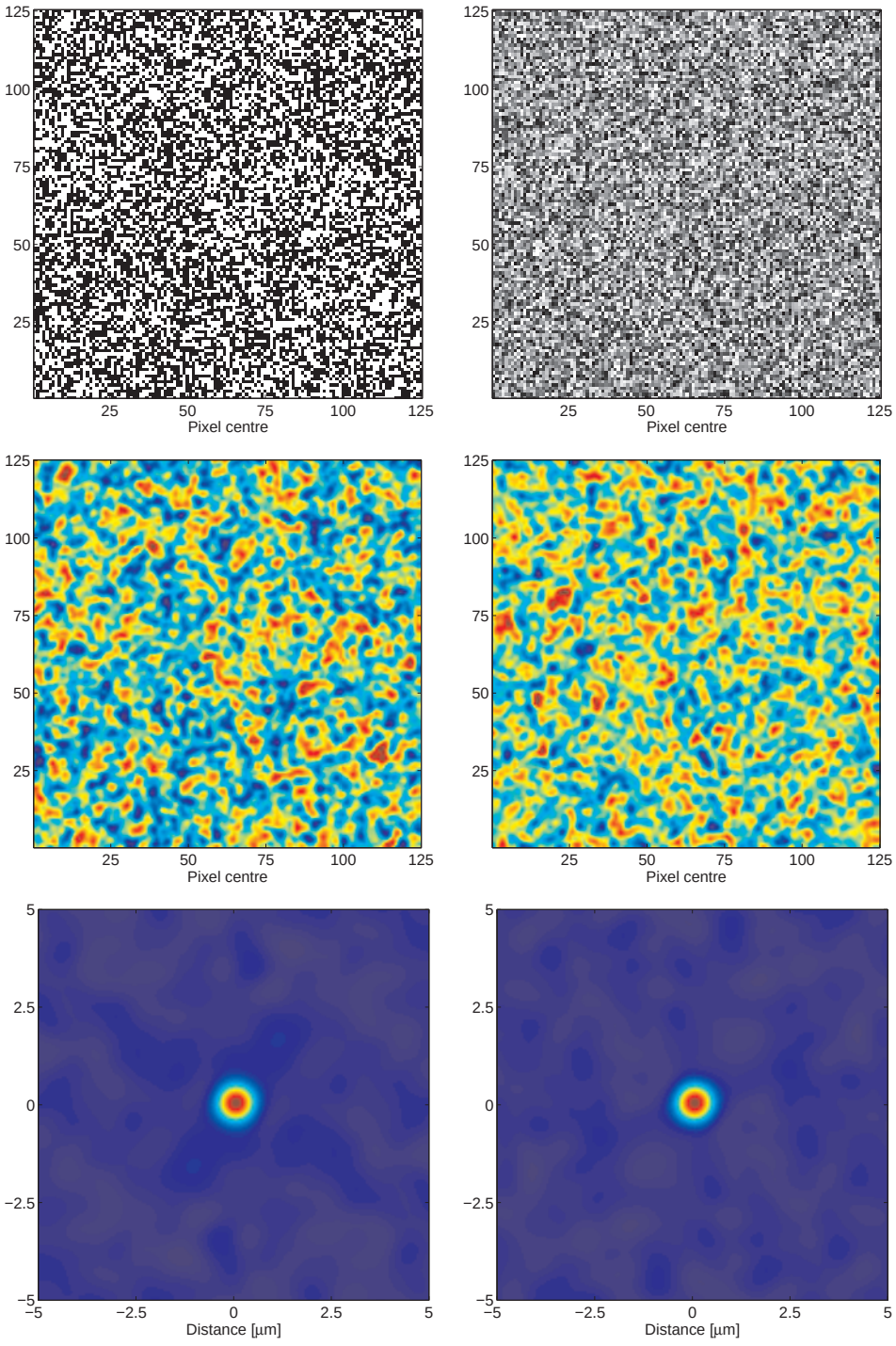

Figure 5.6: showing numerical simulation comparing the production of a disorder potential for binary (left) and grey scale (right) SLM pixels. The image width is 27μm, with pixels separated by 0.216μm. The pixel e^{-2} width is 0.9μm corresponding to a FWHM of 0.532μm. The top images show the distribution in the image plane, represented as an array of point sources. The centre images represent the image plane for incoherent illumination. The bottom images show the auto-correlation peak of the centre images (note the change in scale).

useful. However, by dynamically changing the occupied modes, or the phases between individual modes, the speckle pattern can be made to change in time such that on integrating a homogeneous field is produced. Achieving a washing out of the speckle pattern on a fast enough time scale then provides a more useful illumination source. Relevant time scales for use with this apparatus are related to atomic motion, requiring time scales of order 1μs given by the trapping frequencies of the lattice sites.

To provide illumination for the SLM such an approach has been taken, using a two-step process. First, the size of the speckle grain is reduced to allow more efficient averaging. This is achieved by increasing the occupancy of the fibre mode spectrum. To homogenise this speckle pattern on integrating a special technique has been developed. To protect intellectual property, only an analysis of the effectiveness of the technique will be presented with the working principles omitted.

5.5.1 Point load mode scrambler

The averaging process will occur more readily with a finer grained speckle pattern. This can be produced by occupying a larger portion of the mode spectrum of the fibre, thus increasing the number of **k**-vectors contributing to the output field. This can be accomplished through use of a mode scrambler, which ideally serves to re-distribute the light in the fibre from the initially launched modes equally throughout the entire mode spectrum, such that they are all equally excited [109]. The modes in a multi-mode fibre are orthogonal meaning that coupling between the modes is very weak. To produce non-zero matrix elements and allow coupling between modes some form of perturbation is required. A perturbation can be introduced through a local variation in the refractive index. There are many methods by which this can be achieved as mechanical action will give rise to local alteration in the density, thickness or stress distribution over the fibre. Commercially available mode scramblers often compress the fibre between several ridges to create variations in the density along the fibre. Another example is thinning the fibre at one point, which can be achieved by heating the fibre at a point and stretching it. However, these methods have been shown [109] to preferentially excite very high order and leaky modes at the expense of lower order modes, leading to a less homogeneous profile with high light loss.

Another method is to create a micro-bend in the fibre [110], creating an almost point perturbation which gives rise to a wide range of spatial frequencies. This can be produced by running the fibre over itself and applying load on the crossing point, as shown in Figure 5.7. The load applied can be accurately controlled, allowing careful tuning and reproducibility of the extent of the mode coupling. This is important as too large a load can lead to preferential excitement of higher order modes causing a concave beam profile. By

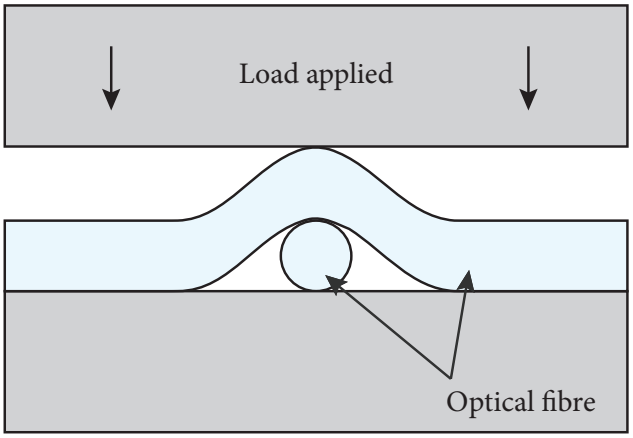

Figure 5.7: showing the point load mode scrambler. A multi-mode fibre is looped over itself and placed between two PTFE plates. A load is then applied to the top plate to compress the overlapping point.

having the fibre cross itself two paired and reasonably identical perturbations are produced. This causes the launched modes to be coupled into a new, wider distribution and then to again be redistributed, occupying modes more evenly over the spectrum.

A point load mode scrambler was created by placing a loop of optical fibre between two plates and applying a defined load onto the top plate. To prevent tilting and maintain a reproducible load distribution the loop was supported at two points by another length of fibre, through which light does not pass. This provides four micro-bends, two at the crossing point and one at each point where the fibre crosses the support.

Figure 5.8 shows the speckle size versus load for a multi-mode fibre with numerical aperture 0.48. This shows a roughly linear decrease in speckle size with load before a limit at which the speckle size no longer decreases. This is appropriate as the mode distribution will become increasingly filled. From the various fibres tested, higher numerical aperture fibres allowed finer grained speckle patterns under load. This can be understood as a higher numerical aperture fibre has a larger mode spectrum, meaning more **k**-vectors are available to contribute to the speckle pattern [111]. For excess load light is increasingly lost from the fibre as leaky modes become occupied.

5.5.2 Effectiveness of the averaging technique

An averaging technique was developed to homogenise the speckle pattern output of the multi-mode fibre. As stated previously, the details of the technique have been omitted for intellectual property protection, with only an assessment of effectiveness presented. For the averaging technique to be viable for use in experiment speckle must be suppressed to a sufficient degree and on sufficiently fast time scales. To determine whether

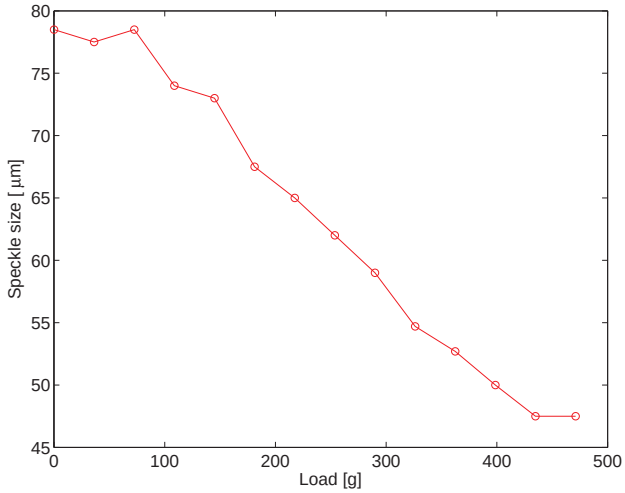

Figure 5.8: showing the FWHM of the speckle grain versus load for a multi-mode fibre having numerical aperture 0.48. Increasing the load beyond this range causes losses and damage to the fibre.

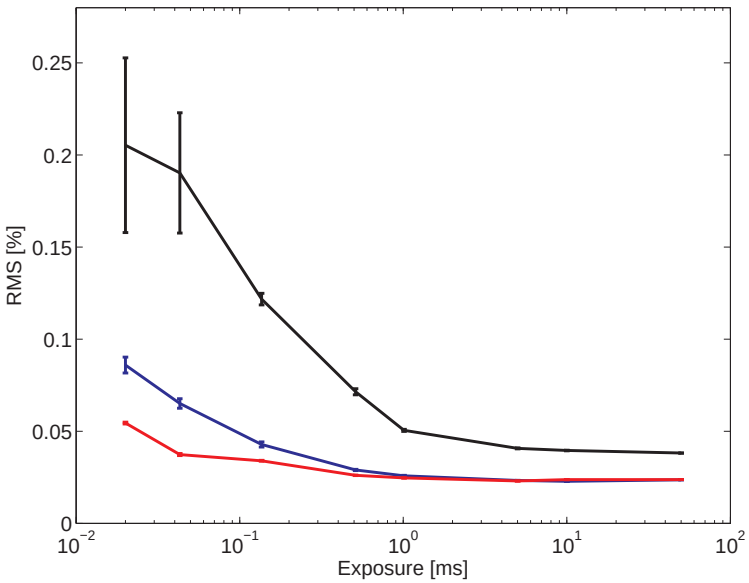

Figure 5.9: showing the RMS fluctuation on top of the multi-mode fibre output versus exposure time for three incarnations of the averaging technique. For shorter exposures the speckle suppression is less effective. With improvement of the technique the RMS is kept to 5% at the shortest exposure time of the camera. The influence of large scale structure and shot noise have been reduced through spatial band-pass filtering

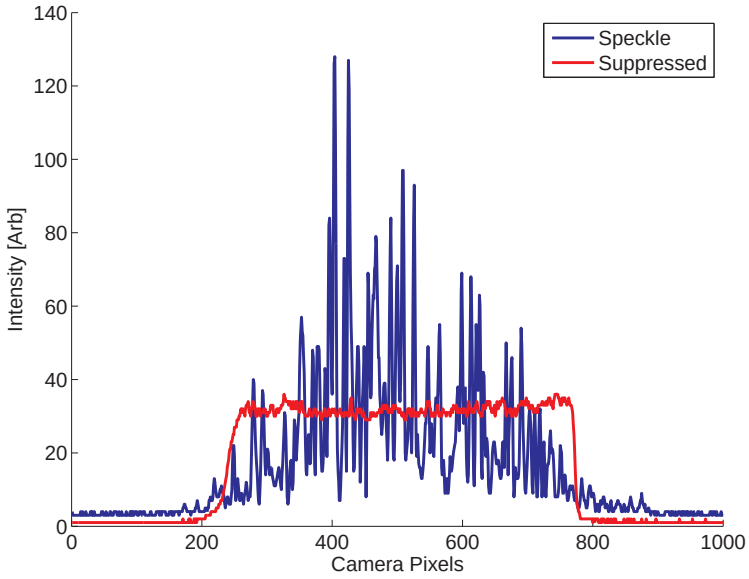

Figure 5.10: showing a cut through of the intensity across output from the multi-mode fibre with and without averaging. The exposure time is 5ms. Large scale structure and shot noise have not been filtered.

this was the case, the technique was applied after being launched with the mode scrambled multi-mode fibre. The output intensity pattern was then captured on a high resolution digital 12 bit CCD camera, BC106VIS from Thorlabs, at various exposure times. Figure 5.9 shows the root mean square (RMS) of the intensity fluctuation over the beam when applying three incarnations of the technique. The offset RMS is believed to be due to a combination of residual large scale structure on the beam and shot noise. The effect of these has been reduced through spatial band-pass filtering around the speckle size. The current optimum configuration achieves an RMS of below 5% down to exposure times of 20μs, the limit of the camera. Figure 5.10 shows a cut through of the beam with and without the technique in action. Speckle is drastically reduced, with fluctuations being suppressed by 12.1dB. Furthermore, the intensity pattern is top-hat like rather than Gaussian. On imaging the SLM onto a 2D atom cloud this would reduce curvature over the plane.

To determine the broadening of the linewidth of the beam induced by the technique the beam was split into two components and passed through two acousto-optical modulators running at different frequencies. One beam is coupled into the multi-mode fibre and mode scrambled before the technique is applied, while the other is passed through free space. The two are recombined on a non-polarising beam splitter and shone onto a high frequency photodiode to provide a beat signal. The speckle suppressed beam is expanded such that one speckle grain covers the photodiode. Figure 5.11 shows the photodiode signal when recorded with a spectrum analyser and filtered. The width of the narrow peak in the inactive case is due either to noise or

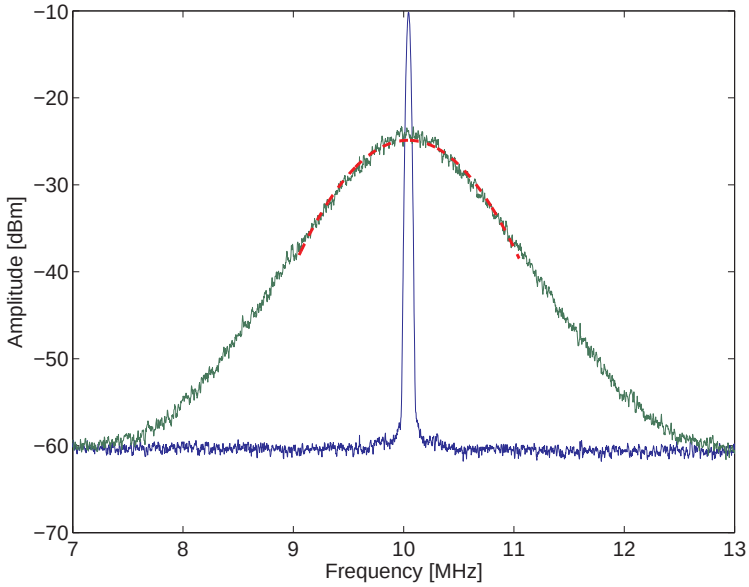

Figure 5.11: showing the beat signal between the output of the multi-mode fibre and a reference beam with (green) and without (blue) the averaging technique applied. The blue peak is limited by noise while the red peak is broadened to 0.95MHz.

the resolution limit of the spectrum analyser. In the active case the width is broadened to 0.94MHz. This is still a narrow width, roughly a factor of two lower than the diode lasers used for MOT cooling.

5.6 High resolution optical system

The primary constituents of the optical system are the microscope objectives themselves, Mitutoyo G-Plan APO 50x objectives. The objectives are infinity corrected and have a numerical aperture of 0.5 allowing resolution of one wavelength. This means a nominal resolution of 532nm for SLM patterns or 780nm for imaging. This would allow sub-lattice spacing resolution with the intended 1μm spacing. Although objectives are available with similar or better resolution, these have the particular qualities of being corrected for use with a glass sheet of 3.5mm thickness and made to have a large working distance of 13.89mm. Using this specification to design a glass cell for the vacuum system then allows mounting of the objectives external to the system without loss resolution. The objectives have a magnification factor of 50x, meaning that an SLM pixel of size 10.8μm is demagnified to 0.216μm. The objectives form a telecentric system, meaning that even when out of focus the demagnification remains the same, making it possible to deliberately defocus the objective to cause additional blurring in the image. The relevance of this is discussed in Section 5.4.4

The objective creates an image at infinity, with a real image being produced at the focal point of a

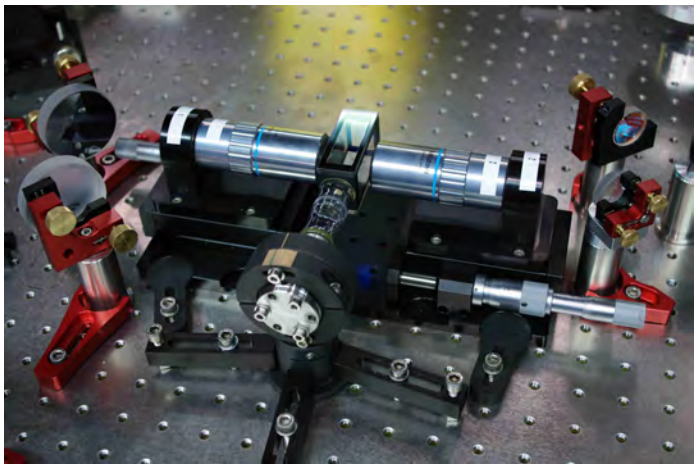

Figure 5.12: showing the mounting of the objectives and glass cell for testing the optical system. The objectives are mounted onto one dimensional measurement stages with differential micrometres. These mount onto a precision base plate which is fixed to the table. The glass cell is held using a rotatable clamp to allow study of how tilting influences resolution.

secondary lens. Thus for the optical system, a secondary lens must be used with each objective, one with the SLM in the back plane and the other the Pixelfly camera.

Building a test system requires design of a mounting system for the two objectives, as shown in Figure 5.12. This consisted of a precision base plate onto which two one dimensional measurement stages with differential micrometres were mounted. This allows fine adjustment of the separation between the objectives but no alignment of their concentricity. This was relied upon by designing the base plate such that the two stages were both mounted at precisely the same height and rotation, by using the high precision dowel points of the stages. To add practicality, the base plate was designed to be used with eight clamps which fit into slots on the base plate. This allows for removal and replacement of the whole mounting system, for example to allow removal of a measurement stage, without losing the position with respect to the rest of the optical system.

The microscopes themselves are then held in a custom mount which fixes onto the moving platform of the measurement stages, again using high precision dowels. They are held using their mounting screw threads turned into a brass cylinder. The objectives are mounted horizontally, rather than the vertical mounting that will be used in the experiment. This introduces one particular inaccuracy, which is that the weight of the objective will cause it to tend to tilt with gravity.

To introduce the glass cell, a separate mount was designed which allowed mounting at various angles in order to test the impact of this on the optical system. This clamps onto the CF16 flange of the glass cell and allows inclusion of a blind flange on the cell both to prevent contaminants entering and to add the option of

pumping down the cell for performing vacuum tests. A flat is included on the base to fix the glass cell in a defined manner with respect to the objectives. In order to prevent user error causing an objective to impact upon the glass cell, the free space on the base plate between the two measurement stages has access points for centrally mounting a spacer which prevents moving the objectives closer than 1mm to the glass cell.

5.7 Testing of optical system

This section will cover the measurement of the resolution of the optical system and that of SLM patterns imaged through it. To determine the best illumination for the system this is performed with three illumination sources: a high power LED formed of two diodes, the beam resulting from a 532nm laser diode after passing the multi-mode source and the output of a commercial Verdi laser system running at powers of order mW. The resolution of patterns put through the system is measured by obtaining the contrast between two peaks. A standard resolution limit is the Rayleigh criterion. This is defined as the point at which one Airy disc falls on top of the first minimum of another [112]. This corresponds to a dip of 26.3% below the peak height.

5.7.1 Measurement of resolution using a target

To measure the resolution of the optical system a 1951 USAF resolution target, a series of line pairs with different pitches, was placed between the two microscope objectives. The optical set up is as in Figure 5.1 with the resolution target in place of the glass cell. The first objective is used to illuminate the target, while the second images the target onto the camera chip. The SLM elements are all set to the active state. To aid in positioning, the target was mounted onto a coarse three axis translation stage. As the objectives specify a numerical aperture of 0.5, a nominal resolution of 0.532μm can be expected with the test light. As measurement on the camera is doubly diffraction limited the measured resolution will be limited to 0.707μm. The highest resolution line pair on the target has 645 pairs per mm, corresponding to a resolution of 1.55μm. However, due to the target having no anti-reflection coating and the lack of 3.5mm glass, the achievable resolution is expected to be limited.

Figure 5.13 shows a comparison of the resolution target when illuminated by a high power LED, the collimated mode scrambled multi-mode fibre output and a collimated beam from the Verdi laser all at 0.1ms exposure time. This highlights the desire for the multi-mode source. The LED clearly displays poor contrast, most likely due to excessive scattering inside the objective, while the Verdi laser gives rise to prohibitive fringes. The resolution of the system measured using the target is shown in Figure 5.14. This shows that the

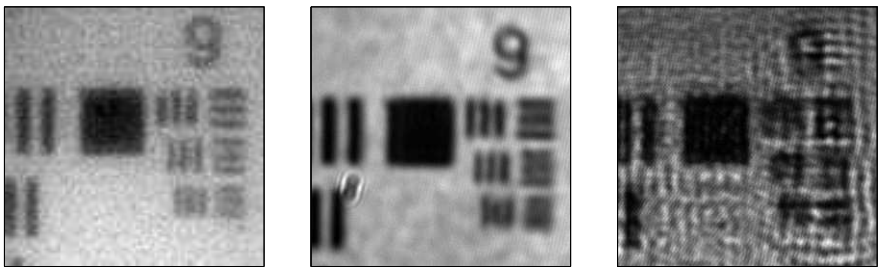

Figure 5.13: showing the camera image (exposure 1ms) of the resolution target when imaged using the optical system. Three illumination types are used; LED (left), multi-mode fibre output (centre) and the Verdi laser (right). The three line pairs used to measure contrast in Figure 5.14 are to the right of the image. The image size is approximately 35μm in the image plane.

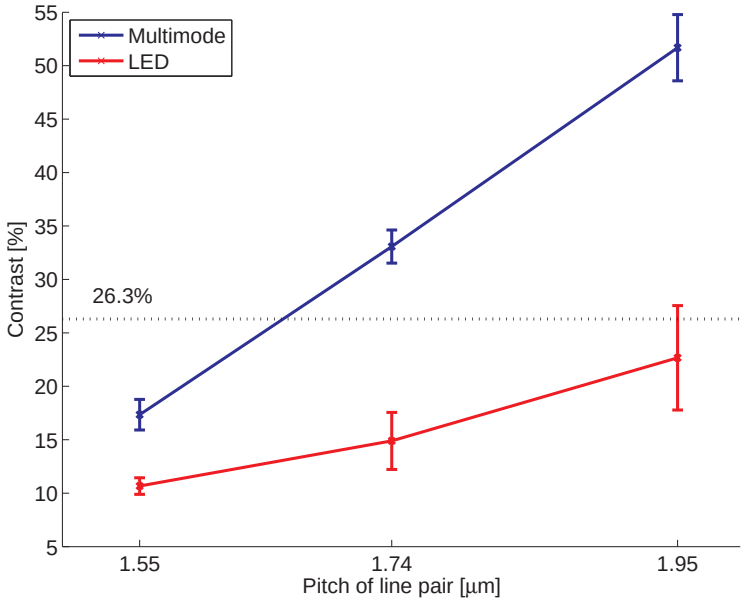

Figure 5.14: showing the contrast between lines using the three finest line spacings on the resolution target. The target has been illuminated with the LED and multi-mode output. The Verdi laser has been omitted due to excessive fringing. The background contrast level has been removed (≈10% for multi-mode and ≈30% for LED). The Rayleigh resolution criterion is shown.

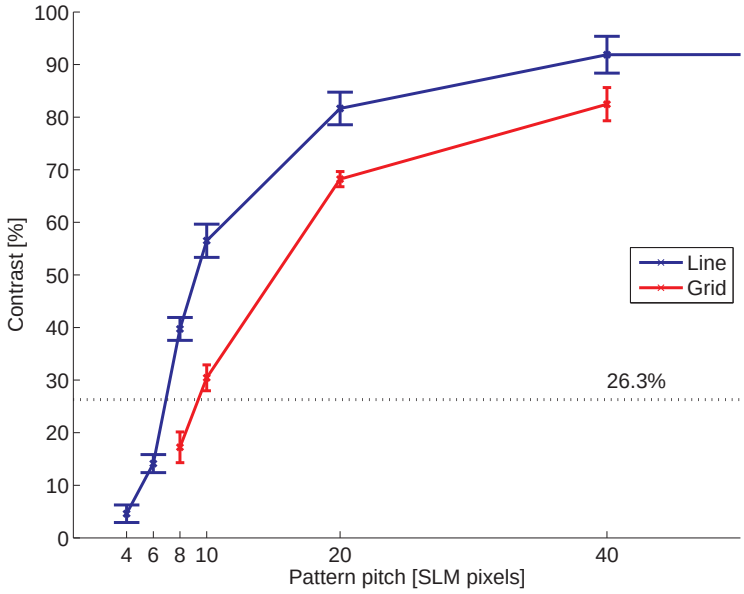

Figure 5.15: showing the contrast versus line pair pitch for patterns generated on the SLM. The illumination light is provided by the multi-mode source. Each SLM pixel corresponds to a distance of 0.216μm in the image plane. Background contrast has been removed.

resolution is best when illuminated with the multi-mode source. However, this is still roughly a factor of two worse than the nominal resolution.

5.7.2 Resolution of spatial light modulator patterns

The SLM pattern was imaged through the optical system and onto the camera. This was achieved by focusing the camera side objective onto the resolution target, then adjusting the focus of the SLM side objective until the SLM pattern was imaged onto the camera chip. To determine how well the image could be resolved, patterns of various line pair pitches were loaded onto the SLM. This was performed across a range, from a pitch of 50 to 2 pixels. Each pixel corresponds to 10.8μm on the SLM or 0.216μm in the image plane. Figure 5.15 shows the contrast level versus pixel spacing, showing that only pitches above eight pixels were resolvable. Extrapolation shows that the Rayleigh criterion falls at a pitch of seven pixels corresponding to 1.512μm. This corresponds to a resolution of approximately 1.1μm when allowing for passing through both objectives.

5.7.3 Testing the influence of the glass cell

The resolution target was replaced with the glass cell of the UHV system, which has high quality coatings on all optical faces, to allow measurement of resolvable structures on the SLM in more realistic conditions. Importantly, the objectives are corrected for 3.5mm glass plates which match the dimensions of the glass cell. The glass cell also has high quality optical coatings which reduce the background offset.

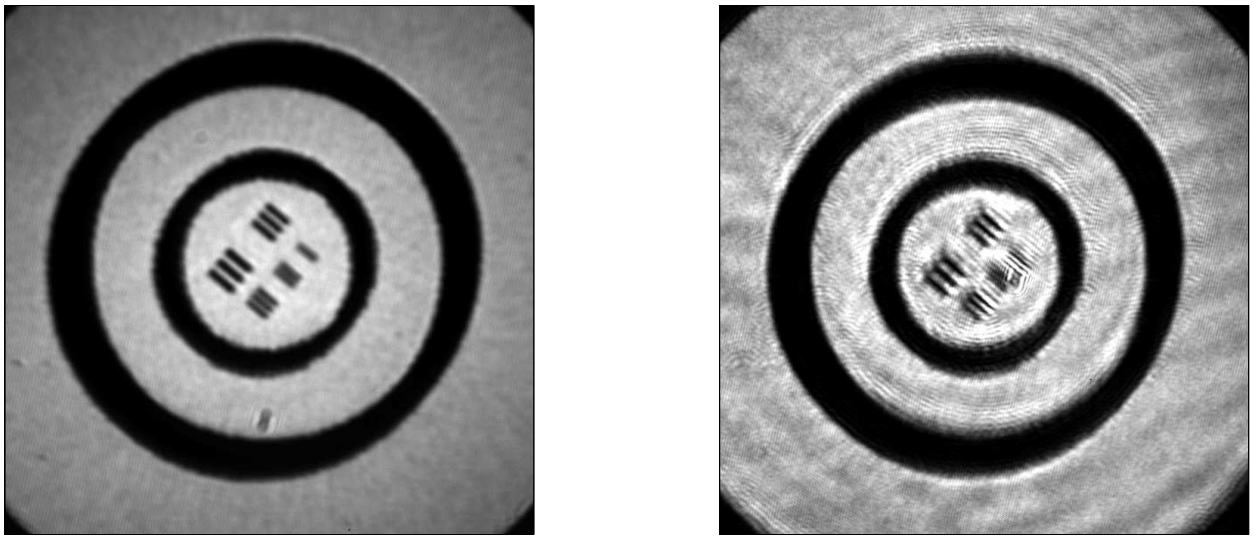

Figure 5.16: showing the SLM pattern after passing through the system with the glass cell placed between the microscope objectives. The multi-mode source (left) has improved resolution compared to testing using the resolution target or SLM without glass cell. Fringes persist using the Verdi source (right) despite the high quality coatings of the glass cell. Both images are 74.4μm across in the image plane.

Figure 5.16 shows a comparison between the resulting camera image for the multi-mode and Verdi sources when the glass cell is placed between the two microscope objectives. The pattern arising when using the multi-mode source now has better contrast and the lower spaced line pairs are visible. When using the Verdi laser fringes are again prevalent.

A particular concern in setting up the system is the optical path difference experienced across the beam surface in travelling through the glass cell if it were slightly tilted with respect to the beam. Figure 5.17 shows the influence of tilting the glass cell over a range of ± 1.5 degrees and Figure 5.18 shows the impact on the contrast of SLM patterns. Tilting the glass cell away from the normal decreases the resolution of the SLM pattern drastically with tilting preventing resolution of any of the line pairs used on the SLM. Tilting decreases the resolution to of order 2.16μm.

The finest line spacing that could be resolved on the camera was 8 SLM pixels. Extrapolating the point at which the Rayleigh criterion is met gives a spacing of 6.2 SLM pixels, corresponding to a distance of

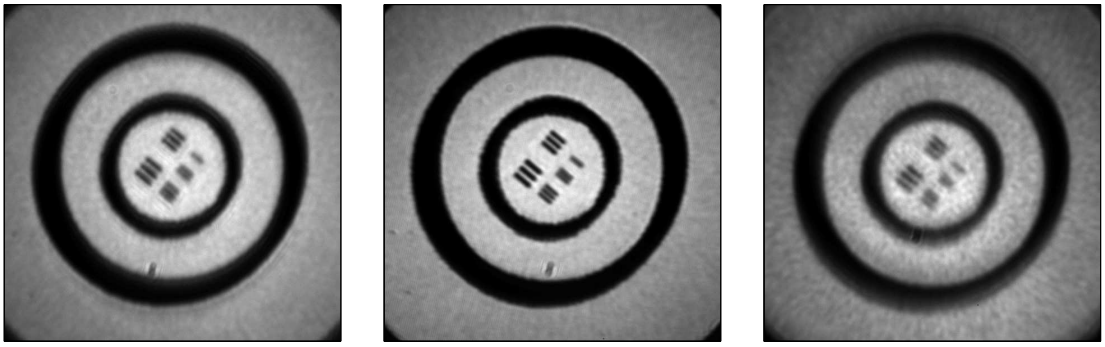

Figure 5.17: showing the change in SLM pattern when the glass cell is tilted $-1.5°$ (left), $0°$ (centre) and $1.5°$ (right) from normal to the beam. The illumination is provided by the multi-mode source with a camera exposure time of 1ms. Each image is 74.4μm across in the image plane.

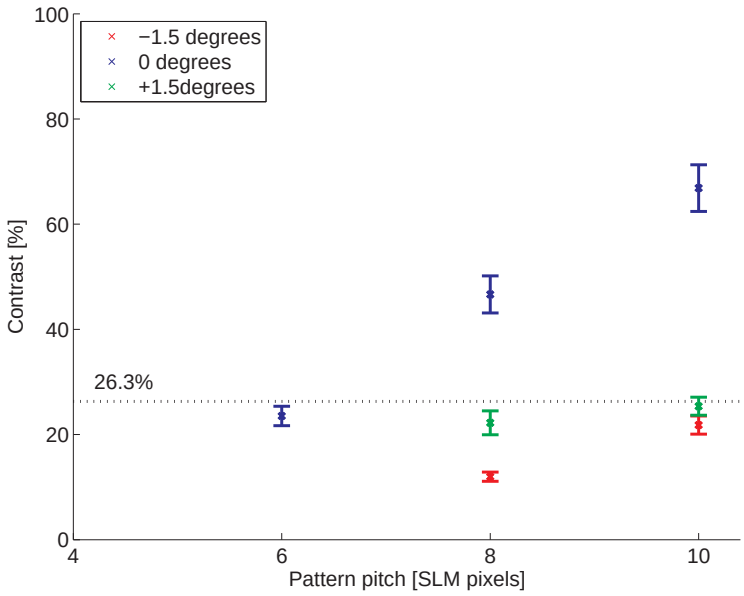

Figure 5.18: showing contrast versus line pair pitch for patterns generated on the SLM when the glass cell is placed between the microscope objectives. Results are shown for the glass cell at three tilt angles. Each SLM pixel corresponds to a distance of 0.216μm in the image plane.

1.3μm in the image plane. This suggests a resolution of 0.98μm when compensating for passing through both objectives, roughly a factor of two worse than the nominal resolution of the objective.

5.8 Prediction of power requirements for experiment phases

With the resolution of the system measured it is possible to obtain an estimate of the parameters one could expect when trying to produce an Anderson localised sample. This requires calculating the mean free path according to (2.16). Using a square area of 11mm side corresponds to a system size of 220μm in the image plane. This sets the upper limit for the localisation length.

The mean free path also depends on the k value of the atom. Taking the same approach as discussed in Section 2.7, converting the interaction energy of a tightly trapped cloud into kinetic energy, would mean calculating for a k value of $k_0^2 = \frac{2m\mu}{\hbar^2}$. As such, the mean free path has been calculated at five different values of μ, centred around $\mu = h \cdot 200$Hz to be comparable to previous experiments [7]. The results are compared for two values of r_c, the nominal resolution limit of 0.532μm and the resolution of 0.98μm.

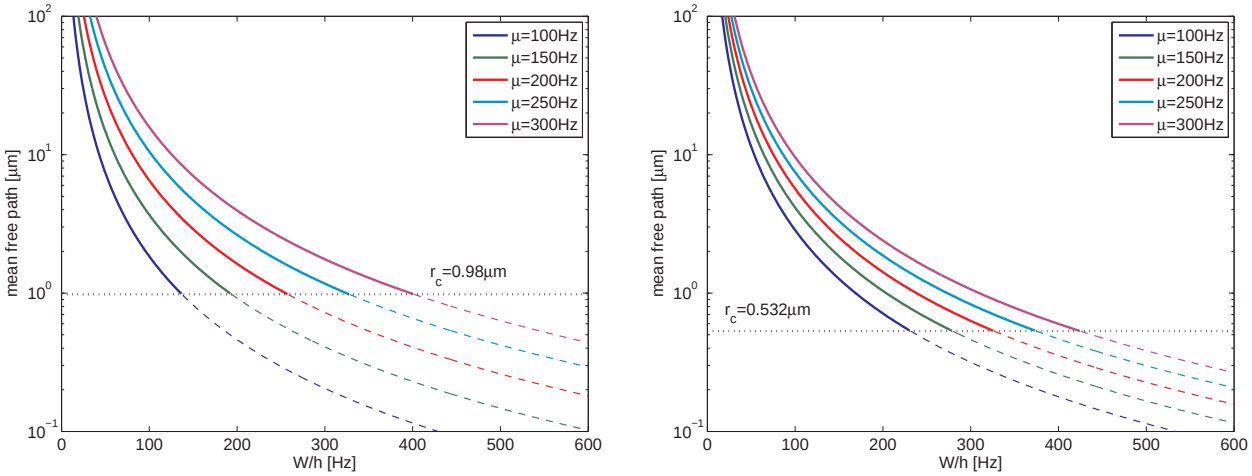

Figure 5.19: showing calculation of the mean free path versus disorder strength W according to (2.16). This is calculated for r_c =0.98μm (left) and 0.532μm (right). Achieving values below r_c is not realistic. The k values are taken from five values of μ. W and μ are in units of the Planck constant.

Figure 5.19 shows the calculation of the mean free path versus disorder strength. The minimum mean free path is reached at a value of between $W \approx 100-400$Hz depending on μ. Using (3.7), this corresponds to laser powers of order 40mW. Figure 5.20 shows the scattering parameter $k \cdot l$ versus disorder strength. This shows that an intermediate $k \cdot l$ value of $\approx 3-5$ can be achieved over the range $W \approx 100-400$Hz (depending on the value of μ taken) for both values of r_c. To determine what would be visible in the system the localisation

length is calculated in Figure 5.21. All of the curves having different μ value can be localised over length scales shorter than the system size. However, to assure that the localisation is not reducing to classical trapping it is necessary to ensure that $\mu > W$ [43]. Inspection of Figure 5.21 reveals that for $r_c = 0.98\mu$m keeping the localisation length below the system size and $\mu > W$ is only possible for $\mu = 100 - 200$Hz. Furthermore, W is always of order μ, with $W/\mu = 0.92$ for $\mu = 100$Hz. While the condition for non-classical trapping is less stringent for 2D than 1D (for example [49] suggests $W/\mu = 0.98$ as a suitable value for experiment), this could lead to classical trapping. The percolation threshold is $0.5W$ for a Gaussian 2D disorder, meaning this is less of a concern. However, it is still desirable to have atoms with energy higher than the potential to demonstrate a clear example of atoms being localised by coherent effects. The situation is better for $r_c = 0.532$ with $W/\mu = 0.85$ for $\mu = 300$Hz. Smaller values of W/μ are possible through use of a larger system size to allow longer localisation lengths and therefore weaker scattering. This could be possible in the current optical system using the long direction of the SLM.

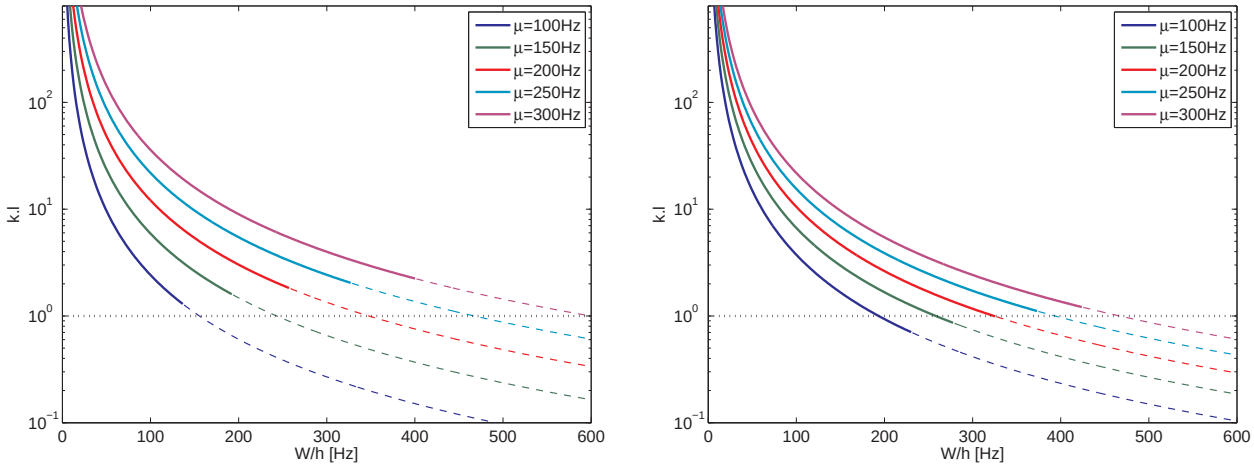

Figure 5.20: showing $k \cdot l$ versus disorder strength W calculated using the mean free paths of Figure 5.19 for r_c =0.98μm (left) and 0.532μm (right). The bold lines illustrate the portion of the curve for which the mean free path is above r_c. As such the dashed lines are not experimentally achievable. The dotted line shows $k \cdot l = 1$. W and μ are in units of the Planck constant.

5.9 Summary

The optical system has been tested, achieving resolutions of 1.74μm when imaging through a 1mm thick resolution target or 1.3μm when imaging the SLM surface through the experiment glass cell. The increased resolution is primarily due to the microscopes being glass corrected for 3.5mm, the thickness of the glass cell walls. If allowing for passing through both objectives these resolutions drop to 1.3μm and 0.98μm

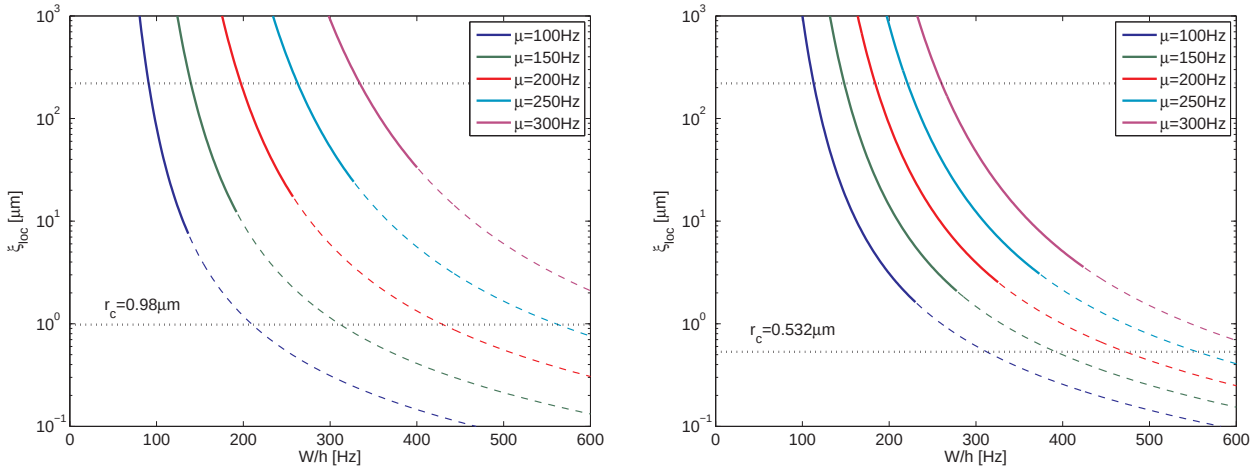

Figure 5.21: showing the localisation length ξ versus disorder strength W for r_c =0.98μm (left) and 0.532μm (right). The bold lines illustrate the portion of the curve for which the mean free path is above r_c. As such the dashed lines are not experimentally achievable. The lower dotted line indicates r_c and the upper shows the system size 220μm. W and μ are in units of the Planck constant.

respectively. These values are higher than the nominal resolution of 0.532μm or 0.707μm when allowing for convolution. The main cause for discrepancy is believed to be due to the horizontal mounting of the objectives during testing. The weight of the objectives then causes them to slightly bend in their mount. As for the experiment system the objectives must naturally be mounted vertically the resolution should be improved. To take account of such problems the objectives will be mounted onto precision xyz stages when used in the experiment. The impact of tilting the glass cell has also been tested, finding that a 1.5° tilt decreased the resolution to of order 2.16μm. This is also a potential cause for the sub-optimal resolution and as such must be accounted for in mounting onto the experiment system.

For providing the illumination for the optical system a multi-mode fibre source has been used to produce a speckle pattern. Through application of a novel technique this has been reduced to a homogeneous profile on timescales down to 20μs, the exposure limit of the camera used for testing. Details of the technique have been omitted to protect intellectual property rights. The source was shown to be broadened to a linewidth of 0.94MHz. The source has applications outside the scope of the project, potentially providing useful illumination for fields such as microscopy.

Using the measured and nominal value of resolution it has been shown that the system should be capable of producing Anderson localised samples. However, especially using the measured resolution, it may not be possible to observe localisation of atoms without going below the $\mu < W$ threshold. To improve upon this the system size must be increased and the resolution improved towards the nominal value.

CHAPTER 6

EXPERIMENTAL PROCEDURE & RESULTS

6.1 Introduction

This chapter will cover the progress achieved by the combination of the apparatus from Chapters 3, 4 and 5. Figure 6.1 shows the current progress of the experiment compared to the experiment cycle for producing a condensate. The system has been built with the aim of first preparing cold rubidium samples and then continuing into potassium and mixtures. The experiment has been brought to the point of consistently producing ^{87}Rb 3D MOTs of approximately 5mm across which are easily visible to the eye without darkening the laboratory. Magnetic transport has also been implemented, with atom clouds being moved into the science chamber. Progress has also been achieved using ^{40}K with 3D MOTs and successful magnetic transport.

6.2 2D MOT of rubidium

A 2D MOT was first produced using the simple 1" beam optical system of Figure 6.2L with four 220 turn coils paired into two anti-Helmholtz configurations, separation 11cm, providing the magnetic field gradient. The optical system was mounted onto a breadboard supported by the aluminium frame which holds the vacuum system. The coils were mounted onto the 2D MOT chamber. The optical system collimates the output of polarisation maintaining fibre from the laser system and sets oppositely sensed circular polarisation for the outgoing and retro-reflected beam. After first observing the 2D MOT the optical system was upgraded to that of 6.2R. This achieves a larger beam size of a 5cm by 2cm ellipse using a cylindrical lens beam expander. To retro-reflect and provide a polarisation shift a 90° prism is used instead of a wave plate and mirror combination. This is preferable financially as large wave plates are expensive. The alternative option

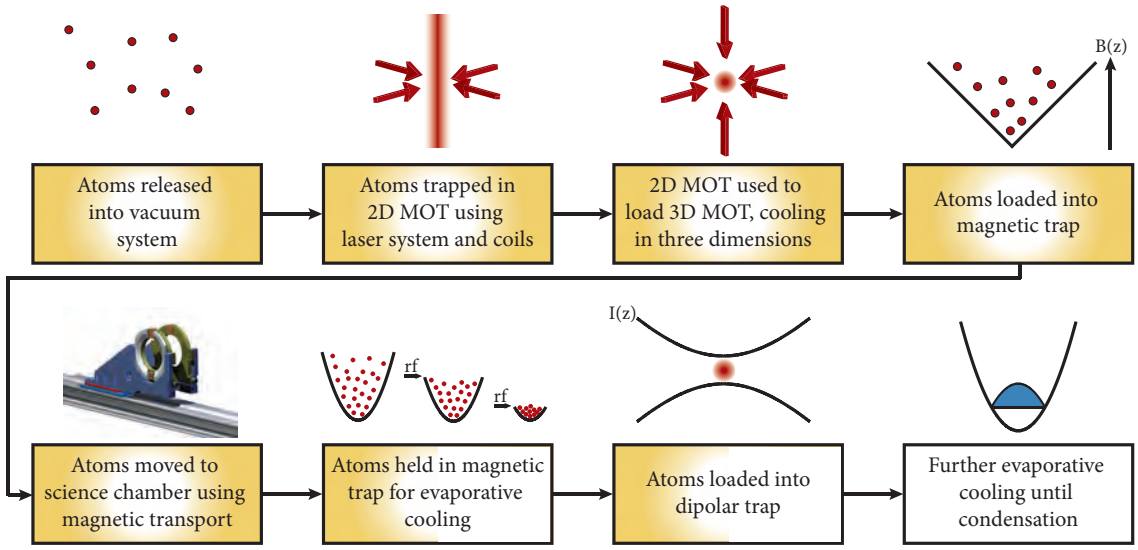

Figure 6.1: showing the experiment cycle. Steps which have been successfully accomplished are highlighted in gold. The apparatus for evaporative cooling has been proved functioning correctly but low magnetic trap lifetimes and leaks in the transport coils have inhibited effective evaporation and prevented further progress. The evaporation apparatus has been tested and used to remove atoms and the dipole trap optical system has been set up and characterised but not used on atom clouds.

of using lenses to contract the beam is not suitable due to space constraints. As expected, upgrading the system produced an elongated 2D MOT. Using the prism the incoming beam is flipped, with each half picking the equivalent of a half wave shift in polarisation. A concern when using the prisms is the presence of a non-reflecting edge where the two 90° reflecting surfaces meet. This places a dark line approximately 1mm thick across the reflected beam, meaning that across the centre of the 2D MOT there is only light travelling in one direction. This sheet of light is not balanced by another in the opposite direction, in principle meaning that atoms will be pushed out of the trap, causing the top half of the 2D MOT to be lost on travelling through the sheet in moving toward 3D MOT. This would reduce the loading rate of the 3D MOT by a factor of two. In an attempt to observe and reduce this effect, during optimisation of loading from the 2D MOT to the 3D MOT chamber, the centre of the incoming beam was obstructed using a mask. This results in two stacked 2D MOTs with a dark region in between. However, the loading rate could only be reduced or made equal using this approach. This is believed to be due to criticality of alignment, as the mask must be exceptionally well centred otherwise it will also induce a light sheet due to the beam inverting nature of the prism. As such, if higher loading rates are required while using the prism system a precision mask could be developed. A 2D MOT produced using this system is shown from above as a dot in Figure 6.3, taken using an infra-red CCTV camera.

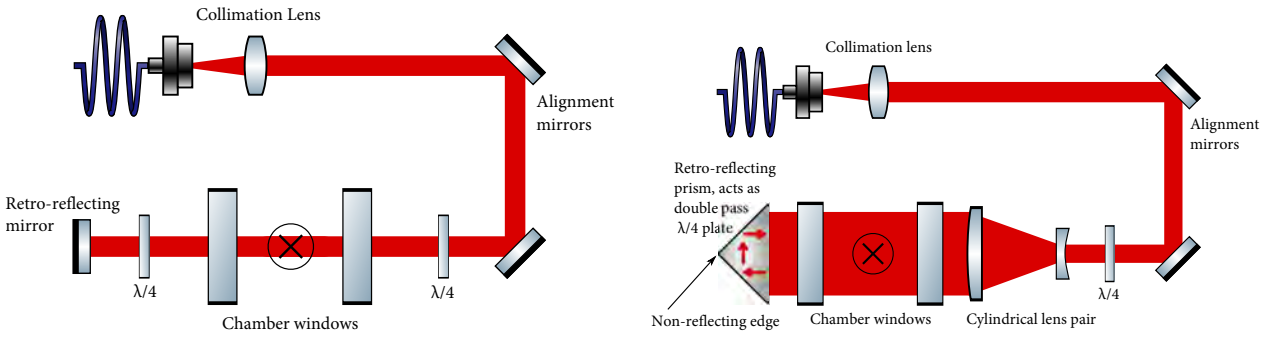

Figure 6.2: *Left:* showing the optical system used to achieve 2D magneto-optical trapping. The output of a polarisation maintaining fibre is collimated and the polarisation set to circular before passing through the vacuum chamber windows. The beam is then retro-reflected and the polarisation rotated in sense. The direction of the second beam pair is denoted by a black cross. *Right:* showing the upgraded optical system. The beam is asymmetrically expanded into an elliptical beam of dimensions 5cm by 1cm. The retro-reflecting mirror and wave plate combination are replaced with a 90° prism. This inverts the beam vertically and changes the sense of the circular polarisation. The indicated non-reflecting edge places a 1mm shadow through the centre of the beam.

Initially the coils used to provide the gradient field for the 2D MOT functioned well, allowing a highly adjustable gradient. However, when the temperature of the coils was approaching equilibrium with the vacuum system, the polarisation of the 2D MOT beams was noticed to have changed on passing through the chamber. This effect was reproducible, with the cause being stress induced birefringence of the vacuum system windows. While this effect could be compensated using wave plates, this would result in a long time scale (approximately three hours) variation in polarisation on start-up of the experiment. To account for this problem more directly a gradient magnetic field was instead produced using permanent magnets. This is based upon the design of [113], modified to provide larger gradients. Four stacks of three neodymium bar magnets are held in four pillars located at each corner of the 2D MOT chamber as shown in Figure 6.4. The pillars attach onto a chassis which mounts directly onto the top of the 2D MOT chamber. Each pillar can be moved in and out over a range of 3cm, allowing minor modification of the field gradient.

A critical step in alignment of the 2D MOT is ensuring that the atom beam has good line of sight to the 3D MOT chamber, allowing atoms to flow directly through the differential pumping stage tube. This is achieved by translating and tilting the permanent magnet mount and viewing the 2D MOT fluorescence from below the differential pumping stage using a camera. The mount was then locked in place by fixing with epoxy at several contact points on the top of the 2D MOT chamber.

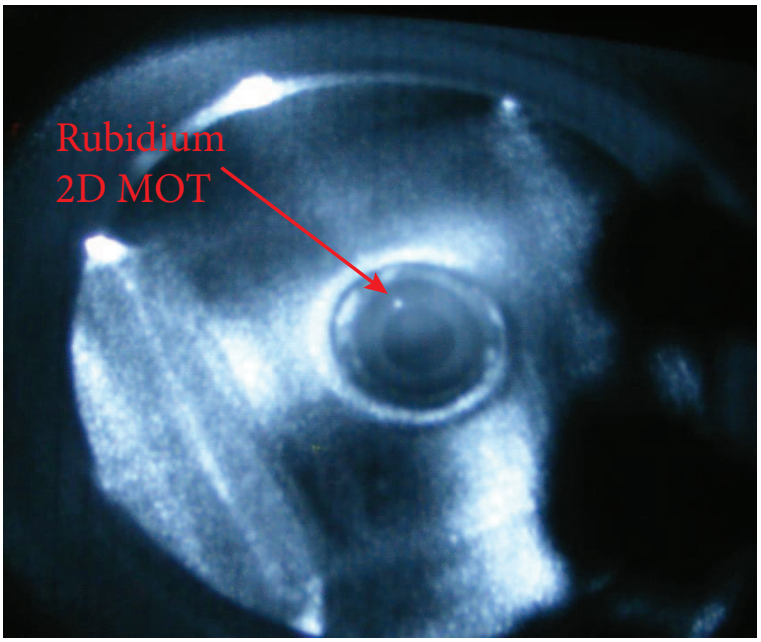

Figure 6.3: showing an infra-red photograph of the 2D MOT taken from above before aligning the 2D and 3D MOT centres. The MOT is a line extending into the page. To the right a shadow of the dispensers can be seen and in the centre of the picture the entrance of the differential pumping stage. For scale, the inner diamter of the graphite rod is 6mm.

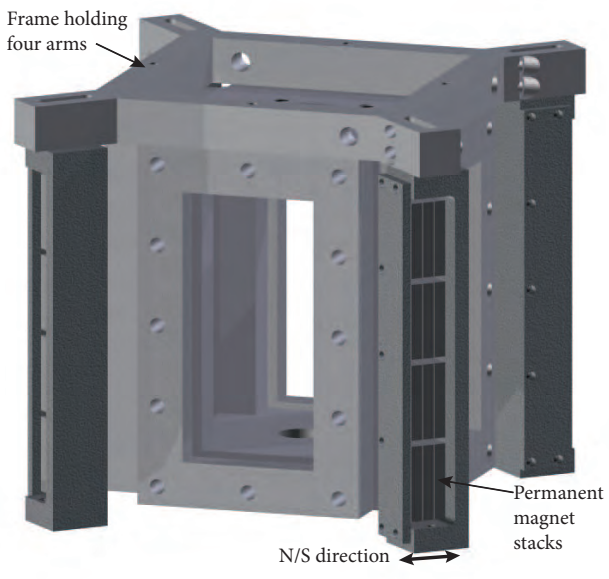

Figure 6.4: showing the permanent magnet housing used to replace the 2D MOT magnetic field coils. Neodymium bar magnets are held in four pillars attached to a mount resting on top of the 2D MOT chamber. Alignment is possible by translating and tilting the mount. For scale, the 2D MOT chamber has an overall height of 120mm.

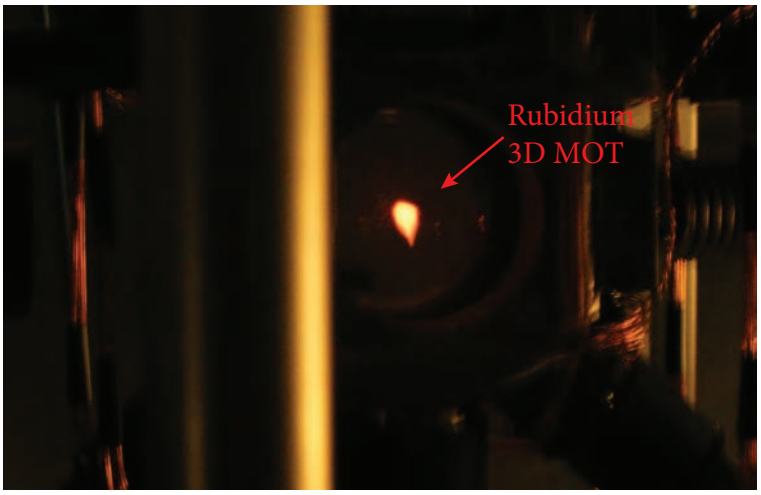

Figure 6.5: showing a photograph of a fully loaded 3D MOT of rubidium 87. The tapered bulge at the bottom of the cloud is due to the pushing beam passing through the MOT. The cloud has a e^{-2} radius of approximately 2.5mm. The direction of gravity is toward the bottom of the page.

6.3 3D MOT of rubidium

The optical system used for the 3D MOT consists of six lens tubes each collimating a fibre output to give a 20mm beam diameter. Each pair is supplied by the outputs of one 50:50 fibre splitter. Two outputs are used for each beam pair, rather than one output and a retro-reflector, to provide better matched beam powers. The light is detuned by $2\pi 18$MHz and the beams have a combined power of 46.6mWcm^{-2}. The four radial tubes mount directly onto the 3D MOT vacuum chamber using a custom mount design which allows fine alignment of the beams. The axial pair are mounted onto height adjustable platforms stood directly on the optical table. Each lens tube contains a wave plate to set the correct polarisation of the beams, with the radial beams all being aligned to have the same sense and the axial pair the opposite. The wave plates used are zero order to permit use of light for both ^{87}Rb and ^{40}K through the same lens tube. The 3D MOT coils of Section 3.6 mount directly onto the 3D MOT vacuum chamber to provide the field gradient. Using this system it was possible to achieve 3D magneto-optical trapping of ^{87}Rb. A photograph of the trapped cloud is shown in Figure 6.5.

A fluorescence imaging system was set up to image the MOT onto a photodiode to provide a signal for optimisation. Optimisation of the 3D MOT is comprised of two broad categories. First it is necessary to optimise the loading rate from the 2D MOT and second to optimise the 3D MOT to achieve high atom numbers and large densities while having low temperatures. These are coupled to some degree as, for example, a high loading rate permits a higher atom number. To provide a useful signal for optimising the loading rate

a short experiment cycle was used to load the MOT for 0.5s before releasing. This allows near real time observation of the effect of adjustments in alignment or parameters. The loading rate is then optimised by achieving the fastest growth in the initial 0.5s. The initial signal change was 20mV between empty and a fully loaded MOT. Adjusting the alignment of the 2D MOT optics provided a 40mV signal when optimised. The pushing beam was then aligned such that it blew away both the 2D MOT and 3D MOT to provide a good alignment criterion. The beam power was then reduced to provide optimum signal. At this point the beam was slightly misaligned to avoid directly hitting the 3D MOT. Using this approach a signal of 131mVs^{-1} was achieved, corresponding to an initial loading rate of $7.6 \cdot 10^7$ atoms/s. For conversion between the fluorescence signal and atom number see Appendix B.1.

With the loading rate optimised, the alignment of the 3D MOT beams was adjusted to avoid shearing or bulging of the cloud. Due to the design of the radial telescope mount the beams are naturally well centred and parallel once adjusted. These were aligned such that the light from one telescope was coupled into the coating of the opposing fibre. The axial telescopes are then aligned to be perpendicular to the radial beams and also cross coupled. Once aligned a fully loaded MOT produced a fluorescence signal of 450mV, as shown previously in Figure 4.20, corresponding to $2.8 \cdot 10^8$ atoms and densities in the low 10^9atoms cm^{-3} range. This is a relatively small MOT, which is to be expected due to the short loading time before reaching a balance in loading and loss rates.

During the growth of the 3D MOT, the atom number initially grows with a linear slope as atoms populate the trap. However, as the trap fills loss mechanisms become relevant, altering the growth curve such that it takes on the form $N(t) = Rt\left(1 - e^{-\frac{t}{\tau}}\right)$. Assuming that losses due to background gas are negligible, a high loading rate can be maintained as the MOT fills by reducing the light power or altering the detuning of the 3D MOT beams to reduce loss terms. This was attempted in two steps, but proved ineffective. This was due to the loss rate being dominated by the background gas rather than light induced losses. For such an approach to be effective a longer lifetime is required. The improvements to the vacuum system now allow a lifetime of over 60s, meaning that in future optimisation using this technique should be possible.

To reduce the temperature of the atom cloud further a 10ms period of optical molasses is applied. This requires cancelling of stray magnetic field gradients through use of the compensation coils. Once set up and configured to cancel stray gradients these were enabled throughout all stages of the experiment cycle. To apply the molasses all light is first blocked, then the 3D MOT magnetic field removed. The detuning of the cooling light is then shifted to 2π60MHz and shone onto the atom cloud.

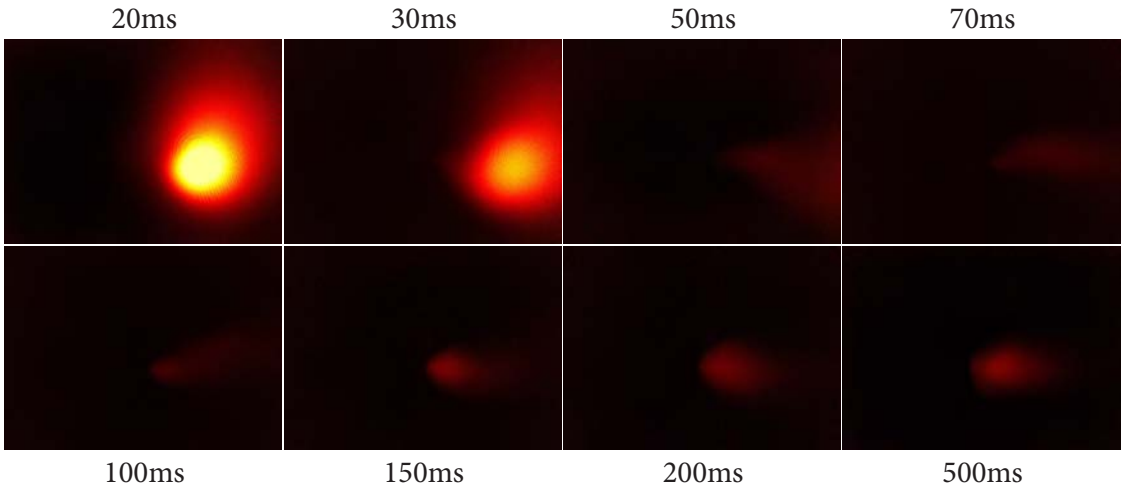

Figure 6.6: showing absorption images of the rubidium cloud when levitated by the magnetic trap field after increasing holding times. This is taken without optical pumping having been performed. In the early stages non-trapped atoms can be seen falling from the trap, with the majority of atoms having been lost by 50ms. The direction of gravity is to the right. The partial revival of the cloud after the 100ms time slot is unclear, but could be due to repopulation from the $|F = 2, m_F = 1\rangle$ state.

6.4 Magnetic trapping and transport of rubidium

After producing a fully loaded 3D MOT the atoms are loaded into a magnetic trap produced using the transport coils. As prior to magnetic trapping the atom cloud still occupies all of the five available magnetic sub-states, at least three fifths of the total atom number is lost during loading the magnetic trap. To improve the efficiency of loading the atoms are first pumped into the desired magnetic sub-state, $|F = 2, m_F = 2\rangle$. This is achieved by applying a bias field and using circularly polarised light from the detection module to induce transitions to the correct state.

With optical pumping complete, all light sources are disabled using the laser system AOMs and shuttered to prevent any resonant light from entering the experiment system. The magnetic field is then set to a weak gradient of 18.4G/cm. This gradient is used as it provides just enough trapping to levitate the atoms, as shown in Figure 6.6, taken without optical pumping. These images, along with others from this section, were obtained using absorption imaging, see Appendix B.2. This stops the atoms from falling under gravity while the gradient is ramped up at a slower rate to prevent heating the cloud. After levitating the atoms for 2ms the gradient is ramped up over 10ms to reach a final strong gradient of 112±5%G/cm, the maximum permitted by the coil cooling system. An image of atoms in the magnetic trap after 0.3s holding time can be seen in Figure 6.7. This demonstrated an average atom number of order $3 \cdot 10^8 \pm 21\%$ atoms. The error term is due

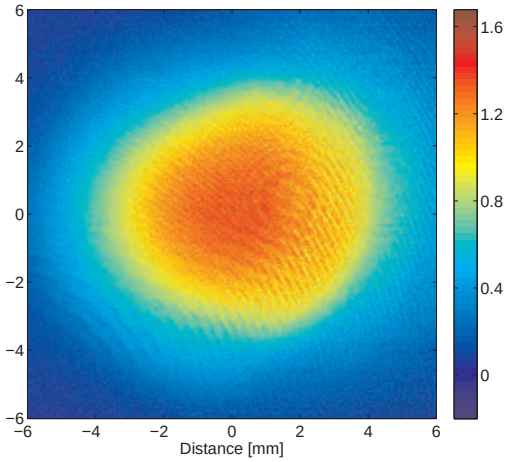

Figure 6.7: showing an absorption image of the rubidium cloud when held in a magnetic trap having strong gradient 112±5%G/cm. The image shows the optical density of the cloud. The cloud has been held in the 3D MOT chamber for 0.3s before imaging. The resonant probe beam has an intensity of $200\mu\text{Wcm}^{-2}$ and is applied for a 8μs pulse. The atom number is $3 \cdot 10^8 \pm 21\%$ atoms, calculated as average of ten realisations using identical parameters to those used to generate the figure. The error represents the statistical spread. The direction of gravity is to the right and the strong trapping axis is into the page.

to fluctuations in the atom number from shot to shot. This is also visible in fluorescence measurements and is due to fluctuation in the intensity of light from the detection module. Although this is accounted for in the imaging measurements, the detection module also provides light for the pushing beam, meaning a fluctuating loading rate (this is also the source of the error margins seen in Figures 4.21L-R and 4.26). In calculating the atom number and error, images with highly anomalous results are neglected (in some images it appears there is little or hardly any atom cloud). Comparison of this and the measurement from fluorescence imaging is not reasonable beyond order of magnitude due to the difference between the measurement techniques.

The magnetic trap lifetime was measured by monitoring the atom number using absorption imaging after increasing holding times. The results of this have already been presented in Figure 4.21, finding a lifetime of 1.76s. As this measurement is exceptionally susceptible to resonant light, great care was taken to prevent any from entering the system. As such, the laser system modules were placed behind a light-proof wall and thoroughly curtained off.

With the atoms held in the trap magnetic transport is performed by holding the atom cloud in the transport coil trap and moving them on the linear actuator. Figure 6.8 shows an absorption image of the cloud taken with the cloud in the glass cell after a total of 1s transport and hold times. The atom number in the glass cell trap is $1.6 \cdot 10^8 \pm 27\%$. The lifetime in the glass cell was measured, with the results having already been presented in Figure 4.21. These gave a lifetime of 12.2s, a factor of seven higher than the lifetime

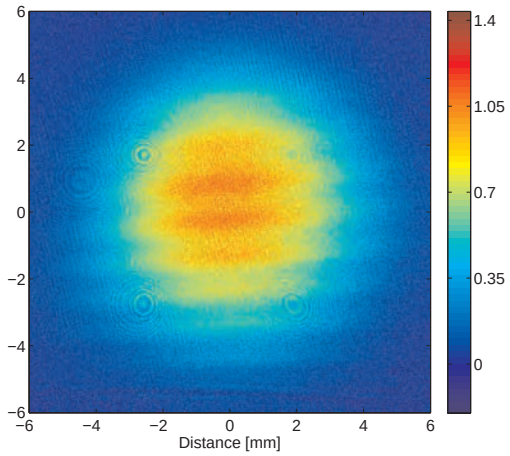

Figure 6.8: showing an absorption image of the rubidium cloud after magnetic transport to the glass cell. The image shows the optical density of the cloud. The strong trapping gradient is 112±5%G/cm. The cloud has been transported from the 3D MOT chamber and held in the glass cell for a total holding time of 1s. The resonant probe beam has an intensity of $200\mu\mathrm{Wcm}^{-2}$ and is applied for a 8μs pulse. Averaging over ten realisations using parameters identical to those in the figure gives an atom number of $1.6 \cdot 10^8 \pm 27\%$. The direction of gravity is down with the strong trapping axis being into the page.

in the 3D MOT chamber. It is not straight forward to convert this into a transport efficiency determined purely by the transport procedure. Due to the small gradient acting against gravity the atoms are colliding with the narrow aperture of the glass cell during transport. This, coupled with likely evaporation due to atoms hitting the glass cell walls during storage, will alter transport efficiency. Another issue is the loss rate due to background collisions which is not constant during travel. The low lifetime of the 3D MOT chamber reduces the current optimisation procedure to moving the atoms to the glass cell as quickly as possible.

Unfortunately, despite the longer lifetime in the science cell, it was not possible to evaporatively cool the cloud in order to load a dipole trap. This is due to both the short lifetime and too weak a magnetic field gradient. The RF antenna was used to empty the trap but the time available for rethermalisation was too short for efficient evaporation. In addition, a series of leaks developed in the magnet cooling bodies. This inhibited further study of the properties of the clouds, for example temperature. The pressure concerns of the vacuum system have since been resolved, with lifetimes of larger than 60s, as shown in Figure 4.26. This is easily sufficient for evaporation, with experiments typically evaporating over of order 20s. However, improvements to the coil system are still pending meaning further evaporation attempts have not yet been undertaken.

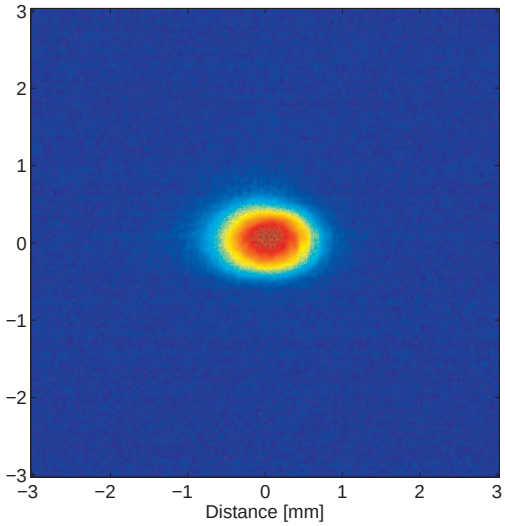

Figure 6.9: showing a fluorescence image of a potassium 3D MOT after fully loading. The atom number is of order 10^6. Calibration of the detunings of the potassium laser system is on-going meaning a precise value for scattering rate, and therefore the atom number, is not yet possible. The direction of gravity is to the right.

6.5 Progress with potassium

With further progress for rubidium hindered by low lifetimes and low gradients in the magnetic trap, the potassium system became a priority. A 2D-3D MOT was achieved without the need for realignment. Figure 6.9 shows a fluorescence image of a potassium 3D MOT having of order 10^6 atoms. Magnetic trapping and transport have also been achieved. In order to test the need for a second chamber for preparing the second species, measurements of the influence of a growing rubidium 3D MOT on a fully loaded potassium 3D MOT were taken. These show a factor of 1.7 suppression in the number of trapped potassium atoms. As this is not a particularly large loss, and is most likely irrelevant for sympathetic cooling [54], a separate chamber appears unnecessary for potassium. As such, the design work put into having a separate chamber will instead benefit by the future addition of further atomic species. This would require a separate chamber due to optical access constraints.

6.6 Current status

Unfortunately two issues were hindering further progress. First, as discussed in Section 4.7.1, inaccuracy of the instruments measuring the pressure of the vacuum system masked an unacceptable pressure of the background gas. As the only reliable way to obtain measurements of this was using atom clouds the experiment had to progress considerably before this problem could be revealed. This prevented using long loading times for the

3D MOT and limited the amount of time in which evaporative cooling could take place. The second problem was having too low a gradient in the magnetic transport coils. The size of the trap was large enough that the outer region of the trap was lost in passing through the narrow aperture on entering the glass cell. The maximum gradient that the coils could provide was measured, using a Hall probe, as 112±5%G/cm in the strong direction at 80A current (the maximum allowed by the coil power supply and cooling system), with the strong direction being aligned perpendicular to the direction of gravity. The low gradient also prevented fast rethermalisation times during evaporative cooling which, coupled with the low lifetime, prevented efficient evaporation. The coil cooling body was also not sturdy enough to prevent intermittent leaks.

To address the high pressure, the 3D MOT chamber has been replaced with a near identical chamber which instead uses indium sealing. The UHV system has been baked and is displaying pressures of below $1 \cdot 10^{-11}$mbar. Atom cloud measurements have been performed, finding lifetimes of longer than 60s in both the 3D MOT and glass cell positions. This is entirely suitable for the loading stages and evaporative cooling. However, further progress is still hindered by an upgrade to the coil system. The transport coils have been redesigned to have approximately a factor of two smaller radius, meaning roughly a factor of two higher gradient. They also should allow a higher current. The gradient will still be lower than optimum for evaporative cooling, and as such the coils intended for manipulating Feshbach resonances, also pending construction, will also be used to create a strong gradient field.

CHAPTER 7

CONCLUSIONS

This thesis concerned the construction of an experiment for producing mixtures of ^{87}Rb and ^{40}K in a two dimensional potential. One of the key aims of the experiment is achieving single site resolution of a 2D optical lattice using a high resolution microscope objective. A second objective will be used to image patterned potentials, generated using a spatial light modulator, onto the atom cloud. The aim is to allow creation of an extremely versatile potential, permitting study of a wide range of two dimensional physics. The thesis has focused on the progress toward reaching these goals, in particular on the development of the ultra-high vacuum system and the imaging and manipulation system.

A modular vacuum system has been constructed which allows preparing of atomic species in a separate chamber before moving them to a glass cell for further experiment. The system has an exceptionally narrow profile along the transport direction, with the 3D MOT chamber having a total thickness of just 36mm. This was achieved through development of a novel epoxy sealing technique. After baking the system a pressure of order $1 \cdot 10^{-11}$mbar was reached. However, this was followed by a slow pressure rise in the 3D MOT chamber. The system pressure rose to of order $1 \cdot 10^{-10}$mbar in the 3D MOT chamber, taking one month to reach equilibrium. Subsequently, atom clouds were used to measure the pressure, finding pressures of order $5 \cdot 10^{-10}$mbar in the 3D chamber and $8 \cdot 10^{-11}$mbar in the glass cell. These are approximately a factor of 4 higher than indicated by the system.

The cause of the rising pressure was found to be water permeating through the epoxy bonds of the 3D MOT chamber. This was determined through observing the pressure of a test system while surrounding the 3D MOT chamber in a low humidity environment. This caused a decrease in system pressure after five days, with the pressure rising after a similar time scale when returning to ambient humidity. A permeation rate of $K = 8.8 \cdot 10^{-14}\mathrm{m}^2/(\mathrm{Pa\ s})$ was measured for water travelling through the epoxy. Measurement of the

permeation rate of helium through the epoxy gave a larger value than literature, perhaps suggesting that the ingress is faster than permeation.

A potential improvement to the epoxy sealing technique is to use a buffer seal to prevent water from reaching the bond. This is being attempted using Viton poured into the volume surrounding the bond. The time scales involved in testing are of order months. To prevent delay the experiment 3D MOT chamber has been replaced with a near identical chamber which uses indium sealing. The system has been baked and is currently displaying pressures of below $1 \cdot 10^{-11}$mbar. Atom cloud measurements have shown the system to provide optimum conditions for reaching BEC, with a lifetime of over 60s in both the 3D MOT and glass cell chambers. Time scales of this order are suitable for both the loading and evaporation stages.

The imaging system for the experiment aims to achieve resolution of single sites in an optical lattice, allowing detection and, through use of a SLM, manipulation on length scales of order the lattice spacing.

An illumination source has been developed which reduces the speckle pattern output of a multi-mode fibre to a near homogeneous profile. The specifics of the source have been omitted due to the intention of securing intellectual property rights. The source produces a flat top beam with RMS fluctuations of below 5% down to the exposure limit of the camera used for testing. The output was beat against a reference laser showing that the source is broadened to 0.94MHz. This is still a narrow width, roughly a factor of two lower than the diode lasers used for MOT cooling. The multi-mode source, an LED and the output of a laser were compared in the imaging system. The multi-mode source allowed roughly a factor of two better resolution than the LED and produced no fringes on the camera when compared to the laser. The source also has potential applications outside the scope of the current project, for example in microscopy.

The resolution of the optical system has been measured at 1.3μm when using 532nm light. This was achieved when imaging patterns the SLM through the glass cell. If allowing for the loss in resolution caused by passing through a second microscope the resolution is increased to 0.98μm. The measured resolution is roughly a factor of two worse than the specified resolution of 0.532μm. This is believed to be due to the horizontal mounting of the objectives. The impact of tilting the glass cell has also been tested, finding that a 1.5° tilt decreased the resolution to of order 2.16μm. This is another possible cause for the sub-optimal resolution. To take account of such problems the objectives will be vertically mounted onto precision stages when integrated into the experiment. It is predicted that using the optical system will allow production of a strongly scattering disorder potential. However, with the currently achieved resolution and spot size, it may be necessary to use potential depths larger than the atomic energy in order to demonstrate localisation over a practical distance.

The experiment has achieved cooling, trapping and magnetic transport of both ^{87}Rb and ^{40}K. A 2D and 3D MOT system with a maximum ^{87}Rb loading rate of $7.6 \cdot 10^7$ atoms/s has been configured. This allowed trapping of order $2.8 \cdot 10^8$ atoms for ^{87}Rb, measured using fluorescence imaging, and densities in the low 10^9atoms cm^{-3} range. The ^{40}K atom number is of order 10^6. The size of the MOTs for both species are limited by the low 1.7s lifetime in the 3D MOT chamber. This inhibited further optimisation. Atoms have been captured in the magnetic trap finding atom numbers of $3 \cdot 10^8 \pm 21\%$ using the more accurate technique of absorption imaging. The ^{87}Rb and ^{40}K clouds have been successfully transported to the science chamber, with ^{87}Rb atom numbers of $1.6 \cdot 10^8 \pm 27\%$ being achieved. The transport efficiency is dominated by collisions with the background gas and the UHV chamber walls, with the later arising due to the low gradient of the transport coils. Due to the lower lifetime in the 3D MOT chamber, the transport was optimised by moving the atoms as quickly as possible to the glass cell. The next phase attempted was evaporation in the magnetic trap through use of an RF-knife. It was not possible to evaporate efficiently due to a low lifetime of 12.2s in the science chamber and low magnetic trap gradient of $2B'$ =112±5%G/cm in the strong direction. The latter is exacerbated considerably by experiment having the weak gradient direction compensating gravity. As discussed above, the vacuum issues have since been rectified. Since re-baking the system, the experiment has progressed back to the point of optimising a 3D MOT of rubidium and performing magnetic trapping and transport. The experiment is still awaiting an upgrade to the transport coil system. The coils are being replaced with a smaller radius coil which should provide roughly a factor of two larger gradient. This, coupled with the extended lifetime, should allow for efficient evaporation and reaching of Bose-Einstein condensation.

APPENDIX A

A.1 Vacuum performance history

The system was initially built using only metal parts. The filaments of each TSP were degassed and the system prebaked to 250°C for twelve days. Once completed, the system was constructed with all components and baked to 150°C for 18 days. The temperature was kept at this level to reduce thermal stress on the epoxy bonds of the 3D MOT chamber. System pressures are measured on the IGPs shown in Figure 4.14, denoted using their respective chamber 2D, 3D and GC.

Following the initial bake the 3D and GC IGPs showed pressures of $5 \cdot 10^{-12}$ and $7 \cdot 10^{-12}$mbar respectively while the 2D pump only reached $5 \cdot 10^{-10}$mbar. This was limited due to leaks in two of the 2D MOT chamber windows. These were sealed using VacSeal, causing the pressure to drop $8 \cdot 10^{-11}$mbar by the next morning. The TSPs of both the 3D MOT chamber and the science chamber were then fired by passing a current of 48.5A through them for two minutes. This resulted in a decrease in pressure, with pressures of $7.6 \cdot 10^{-11}$mbar, $5.8 \cdot 10^{-12}$mbar and $9.7 \cdot 10^{-12}$mbar being measured on the 2D, 3D and GC pumps respectively. Over the following five days the 3D pressure rose linearly to $2.9 \cdot 10^{-11}$mbar. At this point, both valves were sealed and the TMP switched off. Due to one of the valves being defective and not sealing appropriately the system was vented. As a precaution, the TMP had been set to vent through an argon reservoir. Argon was used to prevent resettling of water over internal surfaces, and chosen over other dry gases such as N_2 due to inertness as during baking the dispensers were taken over their activation temperature.

After replacement of the defective valve the system was pumped down reaching pressures of 2D, 3D, GC: $2 \cdot 10^{-11}$mbar, $1.5 \cdot 10^{-10}$mbar, $2 \cdot 10^{-11}$mbar. The system was then helium leak tested using a mass spectrometer. An increase in helium concentration could only be detected when flooding a bag of helium over the 3D MOT windows.

To maintain a pressure level of $1.5 \cdot 10^{-10}$mbar in the 3D chamber, the TSP had to be fired cyclicly on a period of time scale a week. After firing the pressure dropped to around $1 \cdot 10^{-10}$mbar rising to between $2 - 4 \cdot 10^{-10}$mbar after 7 days. The time to form a monolayer upon a surface is given by:

$$t_{ml} = \frac{4}{nvd_0^2} \tag{A.1}$$

with n the density, d_0 the monolayer thickness, 0.372nm for air, and v the average velocity. For a TSP operating at 10^{-10}mbar, this would give an saturation time of order 7 hours. This corresponds reasonably well with time observed before the pressure begins to rise after firing. The manufacturer suggests a refiring rate of 5-10 hours in this pressure range [91]. Attempts using daily firing over several weeks did not produce a significantly lower initial pressure.

In an attempt to recover the previously obtained lower pressures the system was re-baked to 150°C for two weeks. In particular, this was performed to remove residue argon from the IGPs to prevent instabilities. The system then reached a low pressure point of $3 \cdot 10^{-11}$mbar. Figure 4.19 shows a rise in the 3D pressure over twelve days directly after the bake. Upon reaching pressures of order 10^{-10}mbar it again became necessary to fire the TSP weekly to maintain this level. Although the gradual pressure rise was not desirable, having pressures of this order in the 3D MOT chamber would grant lifetimes of order 100s, sufficient for experiment processes. For this reason, the vacuum system was kept operational until the pressure could be tested with atoms directly.

A.2 Mass spectrometer calibration for helium measurement

The mass spectrometer, QMS200 from Pfeiffer vacuum, provides an ion current proportional to the number of molecules at each mass. To convert this to a measurement of pressure it is preferable to measure a source with defined gas load, such as a calibrated leak. As no such apparatus was available the ion current was instead compared to the signal of a cold cathode gauge, IKR270 from Pfeiffer vacuum rated accurate to a pressure of $5 \cdot 10^{-11}$mbar. The mass spectrometer is used to measure the partial pressure at each mass while the gauge provides total pressure. The mass spectrometer is primarily used for measuring leak rates during helium leak testing. To calibrate this for helium the system was flooded with an atmosphere of helium. The pumpdown curve was recorded for the gauge and the mass spectrometer measuring at the helium mass. The mass spectrometer ion current was then multiplied by a calibration factor to overlap the two curves during the period where helium desorption dominates the pressure, see Figure A.1. After this time the gauge

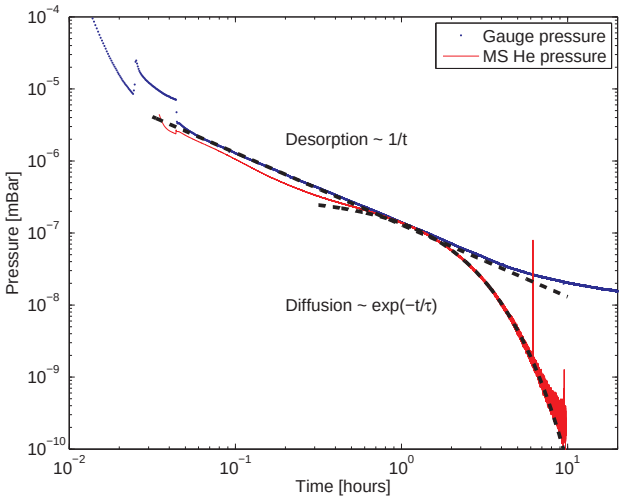

Figure A.1: showing the mass spectrometer and cold cathode gauge pressure during pumping down from an atmosphere of helium. The mass spectrometer trace has been overlapped with the gauge pressure to convert ion current to pressure.

pressure is dominated by the partial pressures arising from desorption of different gases, presumably water, and the helium pressure instead decreases through diffusion. This calibration relies on the gauge current varying linearly with pressure. In reality this is not necessarily the case and the gauge will most likely have a current to pressure function of the form $i = CP^n$ with n being of 1.1-1.4 [87]. As such, measurements of lower pressures are more likely subject to inaccuracy.

APPENDIX B

B.1 Obtaining atom numbers from fluorescence

To measure the fluorescence signal from the magneto-optical trap the cloud was imaged onto a 5kHz photodiode. This was achieved using a 1.5" radius lens placed with a focal length of 300mm. The solid angle through which photons from the cloud hit the detector is then $\Omega = 4.032 \cdot 10^{-3}$. The voltage drop over the photodiode, V, is given by

$$V = iR \tag{B.1}$$

with R the gain resistor, 500kΩ, and i the current. The current is given by the rate at which photons are detected multiplied by the electron charge

$$i = eR_s\Omega NQ \tag{B.2}$$

with R_s the photon scattering rate given by the product of the excited state population with the line width Γ, N the atom number and Q the quantum efficiency of the photodiode, specified as 80% at 780nm. Representing the atom as a two level system, the saturation parameter is [60]

$$s = \frac{I}{I_{sat}} \tag{B.3}$$

with

$$I_{sat} = \frac{\pi hc\Gamma}{3\lambda^3} \tag{B.4}$$

where $\Gamma = 2\pi \cdot 6.066\text{MHz}$ for ^{87}Rb. The saturation intensity is 1.67mWcm^{-2} for ^{87}Rb and 1.75mWcm^{-2} for ^{40}K. For rubidium, the 3D MOT telescopes have a combined power of 46.6mW, with each beam having a 13.5% diameter of 19.8mm. Taking an average of the intensity over the centre 2.5mm radius of the beam (which contains the majority of the atoms, the cloud having a e^{-2} radius of approximately 2.5mm), gives $I_{av} = 0.616\text{mWcm}^{-2}$ per mW of the total beam power. For all six beams active this gives a saturation parameter of $s = 17.2$. The excited state population is given by

$$\rho_{ee} = \frac{\frac{1}{2}s}{1 + s + \left(\frac{2\delta}{\Gamma}\right)^2} \tag{B.5}$$

with δ the detuning. A detuning of $2\pi \cdot 18\text{MHz}$ as used in the MOT gives an excited state population of 0.16 and thus $R_s = 6.1 \cdot 10^6$ scatters per second. Substiting (B.1) into (B.2) and rearranging for N gives

$$N = \frac{V}{eR_s\Omega NQR} \tag{B.6}$$

giving a conversion of $N = 6.3 \cdot 10^5\text{atoms/mV}$. As shown in Figure 4.20, signals of order 450mV are reached for a fully loaded ^{87}Rb MOT, giving atom numbers of $2.8 \cdot 10^8$ atoms.

B.2 Absorption imaging

When irradiating an atom cloud with a near resonant light atoms will remove energy from the beam through absorption. This causes a shadow of the atom cloud to be imprinted upon the beam. A beam, having intensity I, travelling along the z-axis is attenuated according to [112]:

$$I_{out}(x, y) = I_{in}(x, y) \exp\left(-\sigma \int n(x, y, z)\, dz\right) \tag{B.7}$$

where n is the density distribution of the cloud and σ is the absorption cross section specific to the atomic species, given by [55, 60, 114]:

$$\sigma = \frac{6\pi c^2}{\omega_0^2}\left(1 + s + \left(\frac{2\delta}{\Gamma}\right)^2\right)^{-1} \tag{B.8}$$

Rearranging (B.7) gives:

$$n_{proj}(x, y) = \int n(x, y, z)\, dz = \sigma^{-1}\text{OD} \tag{B.9}$$

where n_{proj} is the density with the z-component projected onto the x, y plane and OD is the optical depth of the cloud, given by:

$$\mathrm{OD} = \ln\left(\frac{I_{in}\left(x,y\right)}{I_{out}\left(x,y\right)}\right) \tag{B.10}$$

This allows determination of cloud density distributions and cloud sizes. Through allowing the cloud to expand over increasing times the spreading of the cloud can then be measured, allowing determination of the cloud temperature and many associated properties. This has not been performed due to a lack of stability in the detection beam. The number of atoms can simply be obtained by integration of n_{proj} over the x, y plane (to take into account the detection area per pixel, A, (B.9) must be multiplied by extra factor of A^{-1}). To obtain the information experimentally a $200\mu\mathrm{Wcm}^{-2}$ beam of resonant probe light is used to irradiate the atoms for a short 8μs pulse. Resonant light is used to avoid lensing effects [55]. The light from the beam is then captured on a high performance digital 12 bit CCD camera, a Pixelfly from PCO Imaging. The I_{in} image is simply obtained by taking a second picture without the cloud present.

ACKNOWLEDGEMENTS

My work throughout my time on the project has been guided by Prof. Kai Bongs and Dr. Jochen Kronjaeger. Thanks first to Kai for taking me onto the project and teaching me so much about the field. Thanks for all your help with everything regarding my work on the project and otherwise. I'll miss our morning state of things conversation. It is impossible really to thank you enough Jochen for all that you've done over the past few years. The project wouldn't have got half as far without you. You don't know how glad I am to hear you'll have someone new to bother you.

To the PhD students on the project, Mathis, Nadine, Marisa and more recently Charlotte, thanks for all the hard work in the lab. Mathis and Nadine, we've been working together for ages now, thanks for all the stuff you've taught me. Having had no background in the field I picked up loads from working with both of you, in and out of the lab. Of course you've both caused your fair share of trouble. Nadine's weapon of choice is extremely varied ranging from millimetres, peppers, purposes and oranges to toothpaste. And Mathis plays the long game, delaying a very particular allotment of trouble by a year. Marisa, although you came a bit more recently you've done some great work for the project. As Mat once put it - you are"business", and I think that fits. I won't forget our MATLAB escapades in a hurry. Simon is coming with me. Thanks to Charlotte in particular for being the only one on the project not to spray my face with cooling oil or water. Thanks to the rest of the office; Ole, Mat, and Steve. Ole (the epitome of a kick ass physicist) you helped me out loads when I was starting off with our vacuum system and have given me excellent advice since (and one crazy drive). Mat (it's a house) for being a general source of merry adventures. Steve, it's been a pleasure.

Andy and Caroline, thanks for all the great work on the SLM control code and optical system. Without you the lab has been cleaner (Andy) and also less green. Thanks to Adam for his work on mode scrambling and Nadine and Marisa confundling. Noone loves coils like you.

To the guys from the workshop, Steve, Tony, Jag, John and Dave, thanks for teaching me all sorts about machining and part design as well as creating some great stuff. You made my life easier even if I couldn't return the favour.

Mum, Dad and Chris thanks for all the support over the last few years and recently in particular. The morning lifts and surprise bolognese spring to mind. My wife Zoe, sorry for all the long hours away from home, I know it hasn't been great. Thanks for all the stuff you've done over the last few months so that I've not had to and all the support over the last few years. And all the gingerbread of course. The tapes will be on hold no longer.

LIST OF REFERENCES

[1] Anderson, M. H. et al. *Science*, **269**, 198–201, (1995).

[2] Davis, K. B. et al. *Phys. Rev. Lett.*, **75**, 5202–5205, (1995).

[3] Jaksch, D. et al. *Phys. Rev. Lett.*, **81**, 3108–3111, (1998).

[4] Greiner, M. et al. *Nature*, **415**, 39–44, (2002).

[5] Anderson, P. W. *Phys. Rev.*, **109**, 1492–1505, (1958).

[6] Abrahams, E. et al. *Phys. Rev. Lett.*, **42**, 673–676, (1979).

[7] Billy, J. et al. *Nature*, **453**, 891–894, (2008).

[8] Roati, G. et al. *Nature*, **453**, 895–898, (2008).

[9] Kondov, S. S. et al. *Science*, **334**, 66–68, (2011).

[10] Fisher, M. P. A. et al. *Phys. Rev. B*, **40**(1), 546–570, (1989).

[11] Deissler, B. et al. *Nature Physics*, **6**, 354–358, (2010).

[12] Bakr, W. et al. *Nature*, **462**, 74–77, (2009).

[13] Shearson, J. F. et al. *Nature*, **467**, 68–72, (2010).

[14] Blackmore, A. Master's thesis, University of Birmingham, (2012).

[15] Willis, C. E. Master's thesis, University of Birmingham, (2012).

[16] Mott, N. F. *Proc. Phys. Soc.*, **A62**, 416–422, (1949).

[17] Scalettar, R. T. et al. *Phys. Rev. Lett.*, **66**, 3144–3147, (1991).

[18] Damski, B. et al. *Phys. Rev. Lett.*, **91**, 080403, (2003).

[19] Fallani, L. et al. *Phys. Rev. Lett.*, **98**, 130404, (2007).

[20] Bergmann, G. *Phys. Rep.*, **107**(1), 1–58, (1984).

[21] Ioffe, A. F. and Regel, A. R. *Proc. Semicond.*, **4**, 237, (1960).

[22] Mott, N. F. *Metal-Insulator Transitions*. Taylor and Francis, (1974).

[23] Akkermans, E. and Montambaux, G. *Mesoscopic Physics of Electrons and Photons*. Cambridge University Press, (2007).

[24] Akkermans, E. and Maynard, R. *J. Physique Lett.*, **46**, 1045–1053, (1985).

[25] Sheng, P. *Introduction to Wave Scattering, Localization and Mesoscopic Phenomena*. Springer, 2nd edition, (2005).

[26] Edwards, J. T. and Thouless, D. J. *J. Phys. C Solid St. Phys.*, **5**, 807–820, (1972).

[27] Thouless, D. J. *Phys. Rep.*, **13**, 93–142, (1974).

[28] Edwards, J. T. PhD thesis, University of Birmingham, (1978).

[29] Gor'kov, L. P. et al. *JETP Lett.*, **30**, 228–231, (1979).

[30] Fermi, E. *Nuclear Physics*. University of Chicago Press, (1950).

[31] Shapiro, B. *Phys. Rev. Lett.*, **99**, 060602, (2007).

[32] Apalkov, V. M. et al. *J. Opt. Soc. Am. B*, **21**, 132–140, (2004).

[33] Castellani, C., Di Castro, C. and Peliti, L. (Eds.). *Disordered systems and localization: proceedings of the conference held in Rome*. (1981).

[34] Lee, P. A. and Ramakrishnan, T. V. *Reviews of Modern Physics*, **57**, 287–337, (1985).

[35] Dalichaouch, R. et al. *Nature*, **354**, 53–55, (1991).

[36] Van Albada, M. P. and Lagendijk, A. *Phys. Rev. Lett.*, **55**, 26922695, (1985).

[37] Wolf, P. E. and Maret, G. *Phys. Rev. Lett.*, **55**, 2696–2699, (1985).

[38] Wiersma, D. S. et al. *Nature*, **390**, 671–673, (1997).

[39] Schwartz, T. et al. *Nature*, **446**, 52–55, (2007).

[40] Weaver, R. L. *Wave Motion*, **12**, 129, (1990).

[41] Hu, H. et al. *Nature Physics*, **4**, 945–948, (2008).

[42] Wiersma, D. S., Kaiser, R. and Fallani, L. (Eds.). *Proceedings of the International School of Physics, Enrico Fermi: Nano Optics and Atomics: Transport of Light and Matter Waves*. Societá Italiana Di Fisica and IOS Press, (2011).

[43] Clément, D. et al. *Phys. Rev. Lett.*, **95**, 170409, (2005).

[44] Fort, C. et al. *Phys. Rev. Lett.*, **95**, 170410, (2005).

[45] Aubry, S. and André, G. *Ann. Israel Phys. Soc.*, **3**, 133, (1980).

[46] Robert-de-Saint-Vincent, M. et al. *Phys. Rev. Lett.*, **104**, 220602, (2010).

[47] Kuhn, R. C. et al. *New Journal of Physics*, **9**, 161, (2007).

[48] Sanchez-Palencia, L. et al. *New J. Phys.*, **10**, 045019, (2008).

[49] Kuhn, R. C. et al. *Phys. Rev. Lett.*, **95**, 250403, (2005).

[50] Lett, P. D. et al. *Phys. Rev. Lett.*, **61**, 169–172, (1988).

[51] Dalibard, J. and Cohen-Tannoudji, C. *J. Opt. Soc. Am. B*, **6**, 2023, (1989).

[52] Goldwin, J. et al. *Phys. Rev. A*, **65**, 021402, (2002).

[53] Ospelkaus-Schwarzer, S. PhD thesis, Universität Hamburg, (2006).

[54] Campbell, L. D. et al. *Phys. Rev. A.*, **82**, 063611, (2010).

[55] Ketterle, W., Durfee, D. S. and Stamper-Kurn, D. M. *aking, probing and understanding Bose-Einstein condensates. Proceedings of the International School of Physics - Enrico Fermi, 67.* Societá Italiana Di Fisica and IOS Press, (1999).

[56] Ferrari, G. et al. *Phys. Rev. Lett.*, **89**, 053202, (2002).

[57] Steck, D. A. *Rubidium 87 Line Data*, rev. 2.0.1.
URL: http://steck.us/alkalidata/rubidium87numbers.pdf, (2008).

[58] Tiecke, T. G. *Properties of Potassium*, rev. 1.
URL: http://staff.science.uva.nl/ tgtiecke/PotassiumProperties.pdf, (2010).

[59] Baumert, M. PhD thesis, University of Birmingham, (2012). Not available at time of print.

[60] Metcalf, H. J. and van der Straten, P. *Laser Cooling and Trapping.* Springer, (1999).

[61] Meyer, N. PhD thesis, Universität Hamburg, (TBC). Not available at time of print.

[62] Vogel, A. PhD thesis, Universität Hamburg, (2009).

[63] Pethick, C. J. and Smith, H. *Bose-Einstein Condensation in Dilute Gases.* Cambridge, (2004 reprint).

[64] Bergeman, T. et al. *Phys. Rev. A*, **35**, 1535–1546, (1987).

[65] Metcalf, H. J. *Nat. Bur. Stand. (U.S.) Spec. Publ.*, **653**, 59, (1983).

[66] Lin, Y.-J. et al. *Phys. Rev. A*, **79**, 063631, (2009).

[67] Petrich, W. et al. *Phys. Rev. Lett.*, **74**, 3352–3355, (1995).

[68] Kozuma, M. et al. *Phys. Rev. Lett.*, **82**, 871–875, (1999).

[69] Gott, Y. V. et al. *Nuclear Fusion 1962 Suppl., Pt. 3 (International Atomic Energy Agency, Vienna)*, page 1045, (1962).

[70] Pritchard, D. E. *Phys. Rev. Lett.*, **51**, 1336–1339, (1983).

[71] Esslinger, T. et al. *Phys. Rev. A*, **58**, 2664–2667, (1998).

[72] Greiner, M. et al. *Phys. Rev. A*, **63**, 031401, (2001).

[73] Lewandowski, H. J. et al. *Phys. Rev. Lett.*, **88**, 070403, (2002).

[74] Davis, K. B. et al. *Phys. Rev. Lett.*, **74**, 5202–5205, (1995).

[75] Ketterle, W. and Van Druten, N. J. *Adv. Atom. Mol. Opt. Phys.*, **37**, 181–236, (1996).

[76] Grimm, R. et al. Optical dipole traps for neutral atoms. arXiv:9902072.

[77] Cox, S. G. et al. *Rev. Sci. Inst.*, **74**, 3185–3187, (2003).

[78] Kaltenhuser, B. et al. *Rev. Sci. Inst.*, **78**, 046107, (2007).

[79] Lide, D. R. (Ed.). *Handbook of Chemistry and Physics*. Number 12-211. Wiley, 89th edition, (1988).

[80] MatWeb. *Online materials information resource*.
URL: http://www.matweb.com/ as of 05/09/2012.

[81] NASA. *Outgassing Data for Selecting Spacecraft Materials*.
URL: http://outgassing.nasa.gov/ as of 05/09/2012.

[82] Weatherill, K.J. et al. *Rev. Sci. Inst.*, **80**, 026105, (2009).

[83] Anderson, D. Z. et al. *United States patent, no. US 7,126,112 B2*, (2006).

[84] Tamulevich, T. W. et al. *Epo-Tek technical note*, **11**, (1980).

[85] Chen, W. T. and Nelson, C. W. *J. Res. Develop.*, **23**, 179–188, (1979).

[86] Lees, W. A. *Adhesives in engineering design*. London : Design Council, (1984).

[87] Weissler, G. L. and Carlson, R. W. (Eds.). *Methods of Experimental Physics, Volume 14 - Vacuum Physics and Technology*. Academic press, (1979).

[88] O'Hanlon, J. F. *A User's Guide to Vacuum Technology*. Wiley, 2nd edition, (1988).

[89] Carpenter, L. G. *Vacuum Technology*. Hilger, 2nd edition, (1970).

[90] Avdiaj, S. and Erjavec, B. *Materials and technology*, **46**, 161–167, (2012).

[91] VG Scienta. Manufacturer handbook - titanium sublimation pumps. (2009).

[92] Gupta, A. K. et al. *Vacuum*, **25**, 362–372, (1975).

[93] Gerlach, A. et al. *Microsystem Technologies*, **7**, 17–22, (2001).

[94] Weitenberg, C. et al. *Nature*, **471**, 319–324, (2011).

[95] Grier, D. G. *Nature*, **424**, 810–816, (2003).

[96] Curtis, J. E. et al. *Optics Communications*, **207**, 169 – 175, (2002).

[97] Bergamini, S. et al. *J. Opt. Soc. Am. B*, **21**, 1889–1894, (2004).

[98] Boyer, V. et al. *Phys. Rev. A*, **73**, 031402, (2006).

[99] Graham, B. D. et al. *Phys. Rev. A*, **84**, 053410, (2011).

[100] Graham, B. D. et al. *Phys. Scr.*, **T143**, 014008, (2011).

[101] Moulder, S. et al. *Phys. Rev. A*, **86**, 013629, (2012).

[102] Franke-Arnold, S. et al. *Optics Express*, **15**, 8619–8625, (2007).

[103] Becker, C. et al. *Nature Physics*, **4**, 496–501, (2008).

[104] Bakr, W. et al. *Science*, **329**, 547–550, (2010).

[105] Muldoon, C. et al. *New Journal of Physics*, **14**, 073051, (2012).

[106] Goodman, J. W. *Introduction to Fourier Optics*. Roberts & Company, third edition, (2005).

[107] Solgaard, O. *Photonic Microsystems*. Springer, (2009).

[108] Liang, J. et al. *Appl. Opt.*, **48**, 1955–1962, (2009).

[109] Hallam, A. G. PhD thesis, Aston University, (2007).

[110] Hallam, A. G. Gb patent, no. gb2405488, (2005).

[111] Goodman, J. W. *Speckle Phenomena in Optics*. Roberts & Company, (2007).

[112] Hecht, E. *Optics*. Addison Wesley, 3rd edition, (1998).

[113] Tiecke, T. G. et al. *Phys. Rev. A*, **80**, 013409, (2009).

[114] Arnold, A. S. PhD thesis, University of Sussex, (1999).